2018

Evaluating Hypoxia-Targeting Vectors for MRI Applications

Dj Wijesekera
Western Sydney University
Ingham Institute for Applied Medical Research

Evaluating Hypoxia-Targeting Vectors for MRI Applications

Dj Wijesekera

BSc (Advanced Science, Honours, Class I)

A thesis submitted for the degree of Doctor of Philosophy

December, 2018

Nanoscale Organisation and Dynamics Group, Western Sydney University, Campbelltown

Medical Physics, Ingham Institute for Applied Medical Research, Liverpool

“Success is to be measured not so much by the position that one has reached in life as by the obstacles which have been overcome.”

Booker T. Washington

Statement of Authentication

I, Dj Wijesekera, declare that this thesis contains no material that has been accepted for the award of any other degree or diploma and that, to the best of my knowledge and belief, this thesis contains no material previously published or written by another person, except when due reference has been made in the text of this thesis.

Dj Wijesekera

December 2018

Acknowledgements

First and foremost, I'd like to acknowledge the extensive guidance and support given by my principal supervisor, Prof. William S. Price. Secondly, to my co-supervisors, Drs. Allan Torres, Gang Zheng and Timothy Stait-Gardner, and A/Prof. Gary Liney, you guys have been phenomenal. To Allan, I met you on my first day as an undergraduate, and you have been a valuable source of advice ever since. To Gang, our countless discussions which have led to some pretty interesting research are very much appreciated. To Tim, your assistance with the theoretical work in this thesis is also very much appreciated. To Gary, I will always be grateful for your effort and support, especially during the early stages of my candidature, as I was trying to figure out which directions to take my research.

A very special mention goes out to Dr Abhishek Gupta. It has been an absolute pleasure to work with you during this project. You are a much respected scientist, and you've been a valuable source for nearly every question I could think of during this candidature. Knowing what you can do, I truly wish you all the best with your future endeavours.

A special mention goes out to Dr Scott Willis, whose assistance throughout my candidature, especially during the binding studies, is very much appreciated. A special mention also to Ms Robyn Grey, who has made the administrative aspects of this candidature very easy to manage. A further mention goes out to the other members of the Nanoscale Organisation and Dynamics Group and the School of Science and Health Higher Degree Research cohort, both past and present, for all their support and assistance at various stages during my candidature, with a special mention to Johnny Chen, Mark Donohoe, Mohammad Zaman and Aleksandra Bjelosevic.

I wish to also acknowledge the funding assistance I received from the Australian Postgraduate Award (APA) and the South Western Sydney Local Health District Radiation Oncology Medical Physics Research Top-Up Scholarship.

Finally, and most importantly, I would like to thank my family for all their continued support. To my parents and my brother, I would not be where I am today without all that you have done and continue to do. To Erin, you have been nothing short of amazing over the last few months, and for that, I am utterly grateful.

Publication List

Published

Dj Wijesekera, Timothy Stait-Gardner, Abhishek Gupta, Johnny Chen, Gang Zheng, Allan M. Torres, William S. Price, A Complete Derivation of the Kärger Equations for Analysing NMR Diffusion Measurements of Exchanging Systems, *Concepts in Magnetic Resonance Part A*, 2018 *(in press)*.

Dj Wijesekera, Scott A. Willis, Abhishek Gupta, Allan M. Torres, Gang Zheng, William S. Price, NMR diffusion and relaxation studies of 2-nitroimidazole and albumin interactions, *Spectrochimica Acta Part A: Molecular and Biomolecular Spectroscopy*, 193 (2018) 318-323.

Myo Min, Mark T Lee, Pete Lin, Lois Holloway, **Dj Wijesekera**, Dinesh Gooneratne, et al. Assessment of serial multi-parametric functional MRI (diffusion-weighted imaging and R2*) with 18F-FDG-PET in patients with head and neck cancer treated with radiation therapy. *The British Journal of Radiology*, 2016; 89: 20150530.

Submitted

Dj Wijesekera, Abhishek Gupta, Mohammad S. Zaman, Shawan Karan, Scott A. Willis, Gary Dennis, William S. Price, Hypoxia-Specific Paramagnetic Liposomes, *ChemistryOpen*, 2018 *(submitted)*.

Conference Presentations

A. Gupta, **D. Wijesekera**, M.S. Zaman, W.S. Price, *Hypoxia-Specific MRI Contrast Agents*, Australian MR in Radiotherapy Meeting, Wollongong, Australia 6-7 December, 2018.

A. Gupta, **D. Wijesekera**, M.S. Zaman, W.S. Price, *Visualising tumour hypoxia: advanced MRI contrast agents*, 3rd Translational Cancer Research Workshop, Austinmer, Australia, 5 October, 2018.

D. Wijesekera, A. Gupta, M.S. Zaman, S.A. Willis & W.S. Price, *Evaluation of Hypoxia Using MRI*, Australian MRI-LINAC Collaborators Meeting, Newcastle NSW Australia, 8-9 December 2017.

D. Wijesekera, S.A. Willis, A. Gupta, A.M. Torres, G. Zheng & W.S. Price, *Characterising the Binding of 2-Nitroimidazole: A Proton NMR Study*, ANZMAG Conference, Kingscliff NSW Australia, 2-6 December 2017.

D.Wijesekera, A. Torres, S. Willis, G. Zhang & W. Price, *The Binding of Nitroimidazole to BSA: A Proton NMR Study*, WSU Symposium on NMR, MRI and Diffusion, Campbelltown, NSW, 29 November 2016.

D. Wijesekera, S. Tang, J. Otton, E.S. Koh, R. Rai, B. Schmitt, L. Holloway, V. Batumalai, G. Delaney & G. Liney, *Longitudinal Accuracy and Reproducibility of Quantitative Cardiac MRI Mapping*, The Royal Australian and New Zealand College of Radiologists Conference, Gold Coast, QLD, 13-16 October 2016.

D.Wijesekera, G.Liney, A.Torres, T.Stait-Gardner, L.Holloway, W.Price, *Evaluating Hypoxia*, Research & Teaching Showcase, Liverpool, New South Wales, 27 November 2015.

M.Min, G.Liney, P.Lin, **D.Wijesekera**, M.Lee, L.Holloway, D.Gooneratne, R.Rai, A.Fowler, D.Forstner, *Assessment of diffusion-weighted imaging and R2* measurements with ^{18}F-FDG-PET in head and neck cancer patients treated with radiation therapy*, MR in RT Symposium, Lund, Sweden, 16-17 June 2015.

Abstract

Tissue hypoxia, or oxygen deficiency in tissue, is usually the result of a locally restricted oxygen supply or an abnormal increase in oxygen consumption, or both. Hypoxia is related to a variety of pathological conditions including cancer, stroke and ischemic heart disease. In locally advanced solid tumors, hypoxic and anoxic regions are often distributed heterogeneously due to structurally and functionally abnormal vasculature. Tumor hypoxia has been closely associated with poor cancer prognosis after radiation and chemotherapy, and is known to encourage tumor proliferation factors, such as growth, apoptosis, angiogenesis and metastasis.

In radiotherapy, dosage (i.e., the amount of radiation required to kill a tumorous tissue) is determined by the intrinsic radiosensitivity of the cancer cell population and the tumor microenvironment, in particular the oxygen level of the tissue. Therefore, hypoxic tissues are known to be resistant to the lethal effects of radiation. The ability to accurately identify the hypoxic levels of tumors, and regions within a tumor, can allow clinicians to alter radiotherapy treatment planning to improve treatment outcomes. Consequently, considerable efforts have been made to identify hypoxia within tumors.

Of particularly interest at present is to develop chemicals, incorporating hypoxia-targeting vectors, which specifically accumulate in hypoxic tissue when injected and can then be traced/imaged by an imaging modality, thus allowing delineation of hypoxic parts of a tumor. The potential of these compounds as markers for hypoxic tumors has long been realised, and have been extensively exploited in positron-emission tomography imaging, but less so in magnetic resonance imaging. However, developing such compounds for MRI first requires determining which of the several available hypoxia-targeting vectors is most favourable. As these targeting vectors bind to macromolecular structures, a suitable model for such determinations is to probe the binding interactions of these vectors in albumin. Probing such interactions has been studied by nuclear magnetic resonance spectroscopy due to its general applicability and non-invasive nature. NMR diffusion measurements allow binding ligands to be easily differentiated from non-binding molecules by significant differences in the diffusion coefficients. The mathematical framework for analysing such data is provided by the Kärger equations.

To understand limits of these equations, such as the short gradient pulse approximation, and thus the conditions under which these equations are valid, a detailed derivation of these equations for the case of two freely diffusing exchanging species is

presented along with the simplifications that result in the slow and fast exchange limits. This leads to the population weighted diffusion equation, which is then used to quantitatively characterise the binding properties of the hypoxia-targeting vectors in albumin by the number of binding sites, *n* and the association constant, *K*.

The binding properties of three hypoxia-targeting vectors were investigated: 2-nitroimidazole, 4-nitroimidazole and 6-nitroquinoline, using NMR diffusion and relaxation measurements. For the vectors which showed binding in diffusion NMR experiments, the binding was probed at three different protein concentrations (0.23, 0.30 and 0.38 mM) with drug concentrations ranging from 0.005–0.16 M at 298 K. Simultaneously fitting the Kärger model to the data obtained from the NMR measurements (D, R_1 and R_2) yielded significantly more robust results than individually fitting each dataset, from which n and K were determined to be 21 ± 3 and 53 ± 4 M−1, respectively. However, n and K were not determined for 4-nitroimidazole and 6-nitroquinoline as any binding interactions were not detected by the diffusion data. However, it is most likely the binding interactions are considerably weak based on the relaxation data, and thus the associated extremely fast exchange process was outside the time scale of the diffusion measurements.

With 2-nitroimidazole possessing the strongest binding interactions of the three vectors studied, 2-nitroimidazole was conjugated to a saturated lipid chain, thus synthesising 1-(2-nitroimidazoyl)octadecane to be used as an active hypoxia-targeting amphiphilic vector. Hypoxia-specific paramagnetic liposomes were then formulated by incorporating commercially available paramagnetic amphiphilic chelates, and 1-(2-nitroimidazoyl)octadecane lipids within the bilayer membranes of the 1,2-dipalmitoyl-*sn*-glycero-3-phosphocholine lipids. Two sets of hypoxia-specific paramagnetic liposomes were formulated: one containing PEGylated lipids and one without, to improve circulation times and optimise targeting, respectively. However, it is likely the absence of PEGylated lipids resulted in less stable liposomes. The relaxivity of the hypoxia-specific paramagnetic liposomes relative to the commercially available contrast agent, Magnevist, increased by a range of approximately 83 - 162%.

The hypoxia-targeting ability of the liposomes was then assessed by comparing the cellular uptake of targeted and non-targeted paramagnetic liposomes in two cell lines: SH-SY5Y human neuroblastoma and MCF-7 human breast cancer, in normoxic and hypoxic conditions. Inductively coupled plasma mass spectrometry revealed a three and five-fold increase in the gadolinium concentration of the hypoxic cells relative to the normoxic cells in the SH-SY5Y and MCF-7 cell lines, respectively, confirming the hypoxia-targeting ability of

these liposomal formulations. However, indistinct contrast difference was observed between the MR images of the normoxic and hypoxic cells in either cell-line, thus suggesting the need to design liposomal formulations with either higher gadolinium content, or better contrast enhancement efficiency, or both. Nevertheless, the primary aim of confirming the hypoxia-specificity of the synthesised paramagnetic liposomes was achieved. This now presents an opportunity to develop hypoxia-specific theranostic liposomes by incorporating hypoxia-activated prodrugs in addition to the targeting and contrast components incorporated in this thesis, thereby combining diagnostic and therapeutic capabilities in a single agent.

List of Key Abbreviations

^{18}F-FMISO	^{18}F labelled Fluoromisonidazole
BOLD	Blood Oxygen Level Dependent
BSA	Bovine Serum Albumin
CPMG	Carr-Purcell-Meiboom-Gill
D_2O	Deuterium Oxide
deoxy-Hb	Deoxyhaemoglobin
DLS	Dynamic Light Scattering
DMF	Dimethylformamide
DOTA	Tetraazacyclododecane-N,N,N,N-tetraacetic acid
DPPC	1,2-dipalmitoyl-*sn*-glycero-3-phosphocholine
DTPA	Diethylenetriaminepentaacetic acid
FBS	Fetal Bovine Serum
FID	Free Induction Decay
FOV	Field of View
Gd	Gadolinium
GdDO3NI	Gadolinium tetraazacyclododecanetetraacetic acid monoamide conjugate of 2-nitroimidazole
HIF-1α	Hypoxia Inducible Factor-1 alpha
HSA	Human Serum Albumin
ICP-MS	Inductively Coupled Plasma Mass Spectrometry
MRI	Magnetic Resonance Imaging

MSD	Mean Squared Displacement
NMR	Nuclear Magnetic Resonance
NMRD	Nuclear Magnetic Relaxation Dispersion
O2	Oxygen
O_2Hb	Oxyhaemoglobin
PBS	Phosphate Buffered Saline
PEG2000 PE	1,2-distearoyl-*sn*-glycero-3-phosphoethanolamine-N-[methoxy(polyethyleneglycol)-2000]
PET	Positron Emission Tomography
PFG	Pulsed-Field Gradient
PGSE	Pulsed Gradient Spin-Echo
PGSTE	Pulsed Gradient Stimulated Echo
pO2	Partial Pressure of Oxygen
ppb	Parts Per Billion
rf	Radio-Frequency
SPECT	Single Photon Emission Computed Tomography

List of Key Symbols

B_0	external magnetic field
D	self-diffusion coefficient
D_b	self-diffusion coefficient of the bound species
D_f	self-diffusion coefficient of the free species
E	attenuated echo signal
g	gradient pulse magnitude
G_f	frequency encoding gradient
G_φ	phase encoding gradient
G_z	slice-selection gradient
η	solvent viscosity
k	Boltzmann constant
K	association constant
M	net magnetisation
P_b	populations of the bound species
P_f	populations of the free species
ρ	nuclear spin density
R_1	longitudinal relaxation rate constants
R_2	transverse relaxation rate constants
S	acquired signal
T	temperature

T_1	spin-lattice relaxation decay constant
T_2	spin-spin relaxation decay constant
T_2*	effective/observed spin-spin relaxation decay constant
T_{aq}	image acquisition time
T_E	echo time
T_R	repetition time
γ	gyromagnetic ratio
δ	gradient pulse duration
Δ	diffusion timescale
τ_m	mean water residency time
τ_R	reorientational correlation time
ω_0	Larmor frequency

Table of Contents

Chapter 1. Introduction

1.1 Cancer

The existence of cancer has been known since ancient times [1]. Since the 1900s, numerous cancer research programs have contributed to an explosion of knowledge in oncology in such areas as the etiology, pathophysiology, detection and treatment of cancer [2]. However, to this day, cancer continues to have a significant impact on world health. In particular, cancer-related statistics reveal the true prevalence of this disease. In Australia, an estimated 138,000 new cases were diagnosed in 2018, with an estimated 49,000 deaths, whereas in the United States, an estimated 1,735,000 new cases were diagnosed, with 610,000 people dying from the disease [3, 4].

Cancer is a disease caused by abnormal cell function and division. Normal cell function and reproduction is based on a controlled 'supply and demand' system [5], where cells will only be sent a signal to reproduce if there are cells that need to be replaced. Cells may need to be replaced due to old age, trauma or mutations preventing the cells from functioning properly. Once these damaged cells are replaced, the cells leave the 'active' reproductive phases, and remain 'inactive' until another signal is received. Some cells lose this control during cell division and begin to divide erratically. This creates an imbalance in cell numbers, and thereby results in the formation of a tumor mass [6]. However, not all tumors are cancerous. Non-cancerous tumors are referred to as benign, whilst cancerous tumors are referred to as malignant [1]. Benign tumors will not invade nearby tissues or spread to other parts of the body. Such examples include fibroids in the uterus and lipomas [7, 8]. Malignant tumors on the other hand, can invade nearby tissues and spread to other parts of the body via the bloodstream, lymphatic vessels or locally, through a process called metastasis [1].

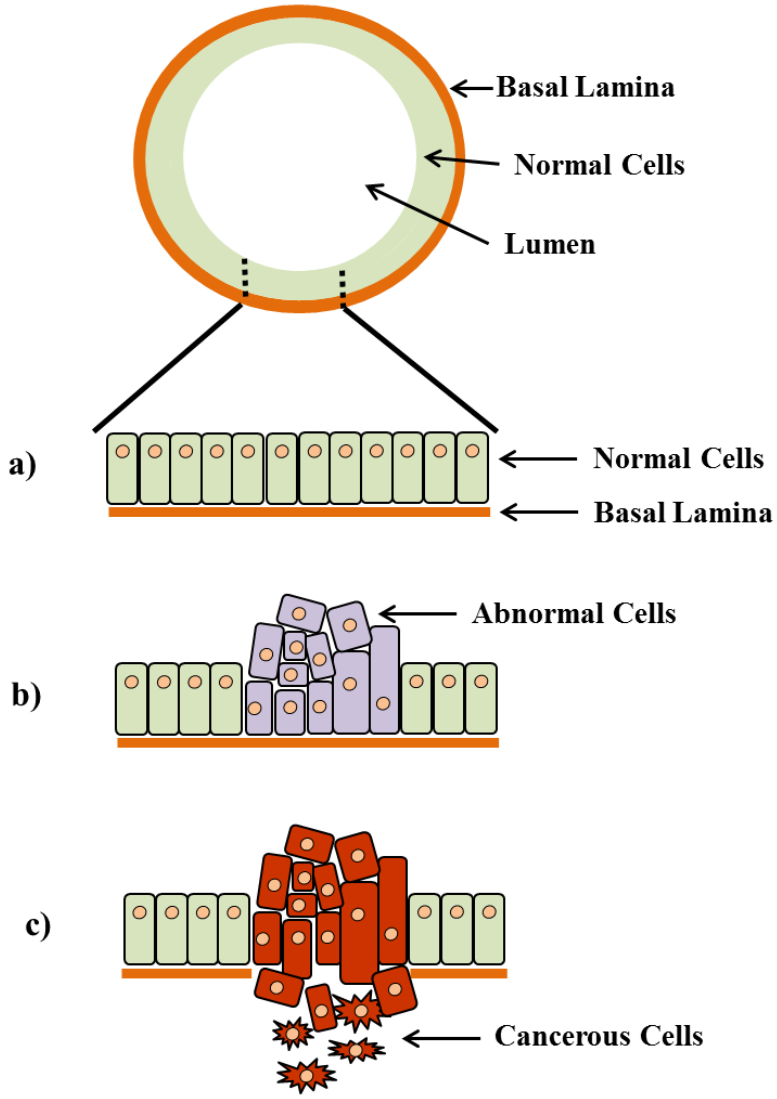

Figure 1: A schematic representation of a) normal cells, b) abnormal cells (i.e., a benign tumor) and c) cancerous cells (i.e., a malignant tumor) within a tubular structure.

At present, many different types of cancer treatments are available (e.g., surgery, chemotherapy, hormonal therapy, radiation therapy and immunotherapy [1]). Depending on the type of cancer and how advanced it is, some patients may only have one type of treatment, while others may have a combination of treatments. Chemotherapy and radiotherapy are two commonly used, highly effective cancer treatment options, and are briefly discussed below.

1.1.1 Chemotherapy

Chemotherapy uses cytotoxic drugs to kill tumor cells by interfering with cell replication through a variety of mechanisms [9]. These mechanisms include breaking the DNA strands (e.g., Cyclophophamide), cross-links in the DNA preventing replication of the cells (e.g., Cisplatin) or inhibition of DNA synthesis and function (e.g., Mitomycin C) [6]. One of the limitations of cytotoxic chemotherapy is that it is not able to distinguish between normal and malignant cells. As a result, normal cells are also killed during treatment, resulting in side effects such as neutropenia, nausea, vomiting, stomatitis and alopecia [6].

1.1.2 Radiotherapy

Radiotherapy uses high energy X-rays, electrons or protons to kill cancer cells [6, 10]. The basic principle of radiotherapy is that such ionizing radiation carries enough energy to cause atoms to gain or lose electrons by forcing electrons to leave their orbitals around the nucleus. This results in DNA damage and other cellular changes, thus causing cell death [11].

Initial forms of radiotherapy treatment involved the use of radioactive sources, but with technological advances such as the development of the linear accelerators (linacs), a variety of radiation types can now be generated in a much more controlled manner. Recent developments have seen linear accelerators combined with other modalities such as magnetic resonance imaging (MRI) scanners, as is the case with the Australian MRI-Linac program [12]. Such developments allow for real time imaging and treatment, which allows for greater radiotherapy treatment accuracy and reduced damage to surrounding healthy tissue.

1.2 Tissue Hypoxia

Whilst new chemotherapeutic drugs with novel action mechanisms may lead to more effective anticancer drugs [13] and advancements in radiotherapy may improve the accuracy of the radiotherapy dose delivered [12], the effect of both treatment modalities on normal and malignant cells are governed by biological factors. One of these factors is tissue oxygenation.

The role of oxygen (O_2) as the terminal electron acceptor in oxidative phosphorylation makes it an essential nutrient for mammalian cells, to such an extent that intricate control mechanisms have evolved to maintain a sufficient supply for the mitochondria. These mechanisms control factors such as blood flow, blood vessel dilation and O_2 extraction fraction to maintain a life-sustaining level of O_2. However, the deprivation of sufficient O_2

required to maintain oxidative phosphorylation in cells results in a phenomenon called tissue hypoxia.

For most solid tumors, hypoxia (i.e., tumor hypoxia) develops due to an inability of the vascular system to supply adequate amounts of O_2 to the growing tumor mass. More specifically, this is due to structural and functional abnormalities of tumor microvessels [14], increased diffusion distances between blood vessels of the expanding tumor cell mass, and a reduction in O_2 in the blood due to disease or treatment related anaemia [15]. Hence, there are three distinct types of tumor hypoxia [16]: perfusion related hypoxia (inadequate blood flow due to structural and functional abnormalities), diffusion related hypoxia (increased O_2 diffusion distances), and anaemic hypoxia (reduced O_2 carrying capabilities of the blood).

Hypoxia can be quantified using partial pressure of O_2 measurements (pO_2). Such measurements reflect the amount of dissolved O_2 present in the blood. In normal tissues, the median pO_2 values range between 24 and 66 mm Hg, whereas values less than 20 mm Hg are common for malignancies [17]. A typical example reveals the median pO_2 of normal cervical mucosa to be 36 mm Hg [17], whereas in cancerous tissue, the value drops from 20 mm Hg at stage zero to 5 mm Hg at stage two [18, 19].

Based on a large body of clinical evidence, the hypoxia-mediated aggressive behaviour of cancer cells and their resistance to therapy is suggested to be orchestrated by the hetero-dimeric transcription factor, hypoxia inducible factor-1 alpha (HIF-1α) [20, 21]. HIF-1 controls the expression of a variety of genes, from which any changes to the proteome and genome of neoplastic cells result in the emergence of more aggressive clones able to overcome nutrient deprivation and hostile environments [15]. This ability of hypoxic cells to overcome hostile environments impairs the effectiveness of radiotherapy and other such treatments. The effectiveness of these treatments become progressively limited with decreasing O_2 concentration, to such an extent that approximately 3-4 times more dose is required to be administered under hypoxic conditions compared to well-oxygenated conditions to achieve the same biological effect (i.e., cell death) [15]. Due to the inability to detect hypoxic regions, the increased dose (e.g., radiation) required for the treatment of hypoxic tumors/regions is not accounted for during treatment planning, thus resulting in treatment failures. As a result, several methods have been established to detect tumor hypoxia [22, 23]. These can be classified as invasive or non-invasive detection methods, and are discussed below.

1.3 Measuring Tumor Hypoxia

1.3.1 Invasive Methods

O_2-sensitive electrodes have been used to measure pO_2 *in vivo* [24-27]. O_2 electrodes are necessarily invasive. The direct correlation of the signal of the electrode and the measured pO_2 value causes the O_2 electrode to be inaccurate in hypoxic applications [28]. This limitation has been overcome with the development of fluorescent needle probes, where the signal increases with decreasing O_2 due to quenching of the optical signal [28-30]. Whilst such needle probes have proven to be more successful, fluorescent needle probes are still limited by tumor accessibility due to its invasive nature. As a result, this thesis will look to utilise non-invasive methods, which are not limited by tumor accessibility.

1.3.2 Non-Invasive Methods

Current non-invasive methods for assessing tumor hypoxia include fluorescence optical imaging [23], positron emission tomography (PET) or single photon emission computed tomography (SPECT) detection of radiolabelled tracers [31-33], and MRI techniques (e.g., Blood Oxygen Level Dependent (BOLD)) [34, 35]. Whilst optical imaging offers advantages such as high sensitivity, a large number of hypoxia-sensitive agents and low cost, one major challenge is the limited penetration depth of both excitation and emission light in living organisms [23]. PET, SPECT and MRI methods do not present such limitations *in vivo* and are beneficial in the clinic to obtain serial images which observe growth-dependent changes, three-dimensional radiotherapy treatment plan distributions and evaluations of therapeutic response. As these methods need to be sensitive to pO_2 levels relevant to tumor therapy, the challenge for hypoxia imaging is to measure low levels of tissue pO_2 on a spatial scale [15]. SPECT is advantageous in that isotopes such as Technetium-99 are readily available at low cost with a convenient half-life for hypoxic measurements while ^{18}F PET offers superior spatial resolution and more accurate quantitation [36]. However, both these techniques expose patients to harmful effects of ionizing radiation. Hence, MRI is the non-invasive method of choice as it does not deal with ionizing radiation, and will be the imaging modality used in this thesis.

In MRI, currently of significant interest in tumor hypoxia detection and monitoring is BOLD MRI [35]. It is particularly appropriate for examining oxygenation responses to external interventions, as it facilitates rapid interrogation of vascular oxygenation [37-40]. Due to its sensitivity to changes in blood flow and deoxyhaemoglobin (deoxy-Hb) content

[41], BOLD imaging distinguishes (paramagnetic) deoxy-Hb from (diamagnetic) oxyhaemoglobin (O_2Hb) allowing vascular oxygenation changes to be revealed through appropriately parameterised-weighted imaging. BOLD-MRI is advantageous in that repeated high temporal and high spatial resolution images can be obtained without the administration of an external contrast agent. However, the progression of this method is limited due to the inability of BOLD MRI to measure tissue pO_2 directly [15]. Such limitations have created interest in hypoxia-targeting vectors, which could potentially aid in the development of methods capable of measuring pO_2 directly. These hypoxia-targeting vectors are discussed below.

1.4 Hypoxia-Targeting Vectors

Hypoxia-targeting vectors are molecules, which possess hypoxia sensitive properties. Such vectors include nitroimidazoles, quinones, aromatic and aliphatic *N*-oxides, and metal complexes, which all undergo activation in hypoxic conditions, irreversibly causing change to their intrinsic properties. With the exception of nitroimidazoles, these compounds are yet to be used in tumor imaging, but have been used experimentally as hypoxia activated prodrugs (HAPs) for cancer treatment [42-47]. Nitro ($-NO_2$) groups undergo selective enzyme-mediated reduction in low O_2 conditions, which is a favourable property to be exploited in molecular targeting of hypoxia. Furthermore, as nitro-based compounds, such as nitroimidazoles, have been studied extensively as hypoxia-targeting vectors and used in different imaging modalities [48, 49], these types of compounds will remain the focus of this thesis.

Nitroimidazoles have been studied for the purpose of exploiting hypoxia selective properties since the 1970s [48] after these molecules were found to selectively bind to the macromolecules of hypoxic regions. Intracellular reduction of nitroimidazoles occur in all cells, however, with inadequate O_2 supplies, further reduction leads to reactive products capable of binding to cellular components [50]. These products are formed following an enzyme-mediated single-electron reduction of the nitro group to a free radical. Even though the reduction pathway may proceed in successive steps past the hydroxylamine derivative, it ultimately terminates at the relatively inactive amine derivative [49], as shown in Figure 2.

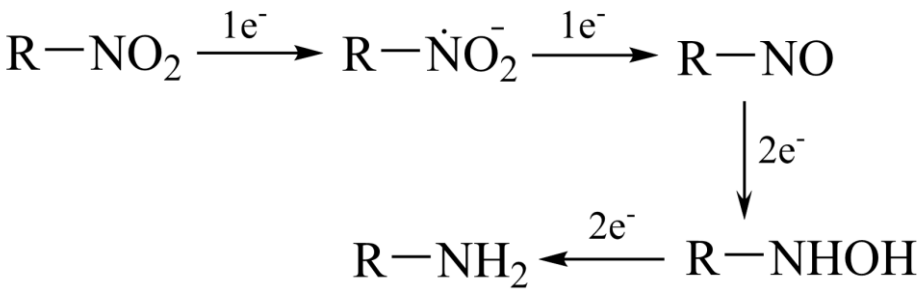

Figure 2: Cellular reduction pathway for nitroimidazoles, which terminates at the amine derivative.

As the compound enters the cell by diffusion through the membrane, its lipophilicity predominately determines the depth of the intracellular interaction. In anaerobic organisms, the pyruvate:ferredoxin oxidoreductase complex is responsible for the initial single-electron reduction. In mammalian cells, a specific enzyme responsible for this reduction has not yet been identified, however numerous enzymes are capable of reducing nitroimidazoles [49, 51].

The higher electron affinity of the intracellular O_2 in comparison to the nitro group causes a reversal of the initial reduction to the free radical anion. The intracellular O_2 concentration determines the rate of oxidation, hence the O_2 sensitivity of the reaction is provided in the initial step of the reaction pathway [49]. Subsequent steps provide the retention required to differentiate between hypoxic and normoxic tissue. Retention occurs in tissues with low O_2 concentrations, as the rate of reoxidation of the original compound is low, allowing further reductive reactions to occur.

The most widely used nitroimidazole-based hypoxia-targeting vectors are 2-, 4- and 5-nitroimidazole (Figure 3). The exact mechanism of nitroimidazoles binding with macromolecules in hypoxic cells is largely unknown [52]. Similar to the macromolecular binding of nitrofurans in bacteria [53] and rat microsomes [54], and nitrothiazoles in schistosomes [55], it is speculated the majority of macromolecular binding of nitroimidazoles also occurs to cellular proteins. Previous studies [53, 56] have shown the biochemical reduction of nitro groups in aromatic nitro compounds to arylamines via nitroso and hydroxylamino derivatives following enzymatic activation by enzymes such as xanthine oxidase, NADPH cytochrome P450 reductase and NADPH cytochrome c reductase [57, 58]. With a variety of hydroxylamines known to bind to cellular macromolecules [59], it is believed these may also be responsible for the macromolecular binding of nitroimidazoles

[60]. Studies involving misonidazole, a nitroimidazole derivative, detected radioactivity in DNA, RNA and protein fractions after administration of [^{14}C]misonidazole, and a molecule with a mass-to-charge ratio corresponding to the hydroxylamine derivative of misonidazole following chemical reduction [60]. This further indicates that the hydroxylamine derivative is likely to be responsible for the binding of nitroimidazoles to cellular macromolecules.

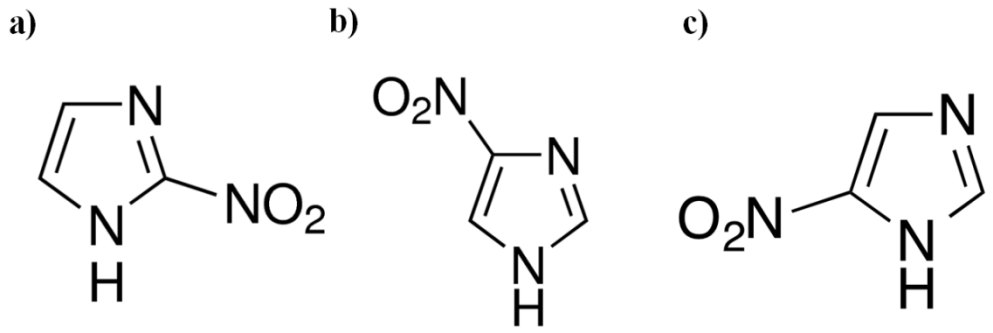

Figure 3: Molecular structures of a) 2-nitroimidazole, b) 4-nitroimidazole and c) 5-nitroimidazole.

With the speculation of the above mentioned hypoxia-targeting vectors binding to cellular proteins, its presents an opportunity to characterise the binding of these molecules with plasma proteins (e.g., serum albumin), which is a common practice in the early stages of drug development. Such interactions can be probed using nuclear magnetic resonance (NMR) methods, and then quantitatively characterised using mathematical models such as the Kärger equations. These ideas will be discussed in greater detail later in this thesis and will be used to characterise the binding interactions of different hypoxia-targeting vectors.

1.4.1 Hypoxia-Targeting Vectors in MRI

The availability of hypoxia-targeting vectors such as those discussed above, has led to the development of several imaging probes targeting tissue hypoxia, of which the most prominent are ^{18}F labelled fluoromisonidazole (^{18}F-FMISO) [61] for PET imaging and ^{99m}Technetium labelled propylene amineoxime [62] for SPECT imaging. Furthermore, several multifluorinated derivatives comprising hypoxia-targeting vectors have been synthesised to assess tumor hypoxia by ^{19}F NMR spectroscopy. However, only one such derivative, gadolinium tetraazacyclododecanetetraacetic acid monoamide conjugate of 2-

nitroimidazole (GdDO3NI) (Figure 4) [63, 64], has been reported for ^{1}H MRI. As a result, this thesis will look to expand on this area of research.

As will be discussed later, the signal intensity in ^{1}H MRI is related to the relaxation rate of *in vivo* water protons, which can be enhanced using a contrast agent administered prior to scanning. These agents utilise paramagnetic metal ions and are evaluated on their ability to increase the relaxation rate of nearby water protons relative to their concentration (i.e., relaxivity). Gadolinium (Gd) (i.e., Gd(III)) is the most widely used metal centre for such proton relaxation agents [65, 66]. While contrast agents such as GdDO3NI provide sufficient contrast with confirmed targeting capabilities, both these properties can be enhanced by encapsulating the 'contrast' and 'targeting' components within supramolecular structures. Such structures present higher relaxivities, and afford relatively easy attainment of favourable pharmacological characteristics, making them excellent candidates as possible carriers for targeted MRI contrast agents, and potentially the next generation of hypoxia-specific theranostic agents.

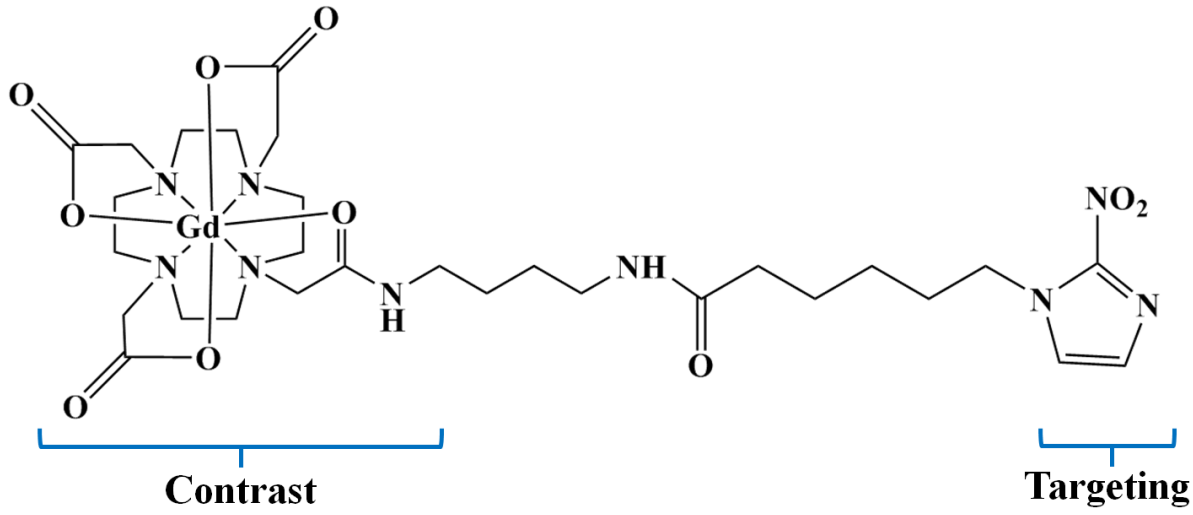

Figure 4: Molecular structure of Gadolinium tetraazacyclododecanetetraacetic acid monoamide conjugate of 2-nitroimidazole (GdDO3NI), with the contrast and targeting components labelled.

1.5 Aims and Objectives

With the ultimate aims of investigating the binding properties of different hypoxia-targeting vectors, and then synthesising a hypoxia-specific paramagnetic agent using one of the studied vectors, the following objectives were set in this project:

(i) understand and derive the two-site binding Kärger model,

(ii) quantitatively characterise the binding of different hypoxia-targeting vectors using NMR methods,

(iii) design, synthesise and characterise hypoxia-specific paramagnetic supramolecular nanoparticles/agents, which incorporate paramagnetic MRI contrast agent and active hypoxia-targeting vectors, and

(iv) investigate the hypoxia-targeting ability of the synthesised structures/agents *in vitro* by assessing the retention of paramagnetic metal ions in cells under hypoxic and normoxic conditions.

In this thesis, Chapters 2 – 4 present the underlying theory and concepts required to understand experimental work of this project. In Chapters 2 and 3, the basic principles of NMR and MRI are detailed, respectively. This becomes relevant in the vector binding and *in vitro* cell studies later in this thesis. With the aim of developing a more effective paramagnetic agent than that currently reported in literature, the different types of contrast agents are reviewed in Chapter 4, ultimately leading to the structure of choice for this project. Experimental/original work is presented from this point forward, starting with a complete derivation of the two-site binding Kärger model, with considerations of both the slow and fast exchange limits, presented in Chapter 5. Using this model for quantitative analysis, the binding studies of different hypoxia specific vectors are presented in Chapter 6. The development of the hypoxia specific paramagnetic agents is detailed in Chapter 7, along with the characterisation of their efficiency as MRI contrast agents. The hypoxia-targeting abilities of the newly synthesised agents *in vitro* cell studies are reported in Chapter 8. To conclude, future research directions are presented with preliminary results in Chapter 9.

Chapter 2. Nuclear Magnetic Resonance, Relaxation & Diffusion

The first step in using NMR methods to determine suitable hypoxia-targeting vectors is to understand the basic concepts of the chosen method. This chapter presents the fundamental aspects of NMR, looking at the basic notions of magnetisation, precession, excitation, acquisition, relaxation and diffusion.

2.1 Overview of NMR

All atomic nuclei possess four important properties: mass, electric charge, magnetism and spin. Whilst mass and electric charge are responsible for the physical and chemical properties of matter, magnetism and spin form the basis of NMR. Magnetism is what enables the atomic nuclei to act as a small bar magnet when placed in an external magnetic field. Spin, an intrinsic quantum mechanical property, is much more difficult to visualise. Simplistically, it can be described as the magnetic moment of an atomic nucleus spinning about its own axis, which is associated with an inherent angular momentum referred to as spin angular momentum (Figure 5). Spin is characterised by a quantum number, I. As spins with $I = ½$, such as the ^{1}H nuclei were studied in this thesis, all discussions in this thesis will relate to spin-half nuclei.

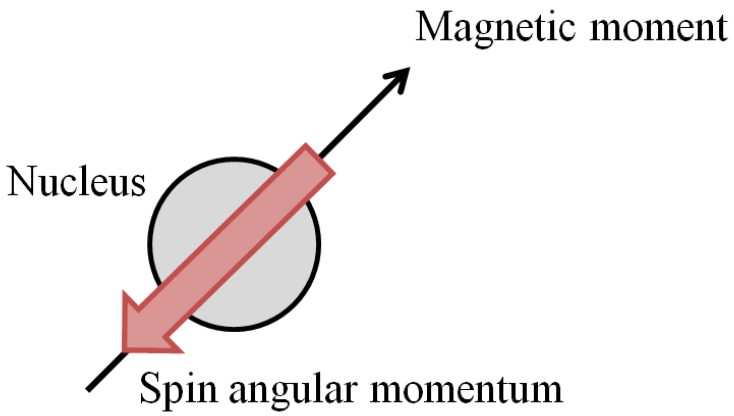

Figure 5: A simplified schematic representation of nuclear spin.

The effect of NMR exists due to nuclear spin, and its interaction with an external magnetic field, $\mathbf{B}_0$ [67]. The interaction of the nuclear spin and $\mathbf{B}_0$ results in a simultaneous

rotating revolving motion of the spins referred to as precession. The angular frequency of precession is referred to as the Larmor frequency, ω_0,

$$\omega_0 = -\gamma B_0, \tag{2.1}$$

where γ is the gyromagnetic ratio of the nucleus and B_0 is the applied magnetic field strength. As a nuclear spin is precessing, it will attempt to align its magnetic moment with $\mathbf{B_0}$ to minimise the energy of the magnetic interaction between the spin and $\mathbf{B}_0$. The difference in energy of the magnetic interaction of a proton when aligned and anti-aligned with $\mathbf{B}_0$ can be calculated to be 4.23×10^{-26} J at a magnetic field strength of 1.5 T. However, in comparison, the thermal energy associated with a proton at 37 ℃ is approximately 10^5 times larger ($\approx 10^{-21}$ J). This implies that the effect on the spins due to the interaction of the spin and the magnetic field is likely to be almost insignificant. Hence, each spin will mostly remain randomly orientated with only a small preference towards the direction of the applied field. However, as even the smallest of samples contain an extraordinary number of nuclei, this small alignment, when summed over the entire sample, can conduce to a net magnetisation, **M** (Figure 6), with a thermal equilibrium magnitude, M_0. The evolution of **M** is described mathematically via the Bloch equations and will be presented in Chapter 5.

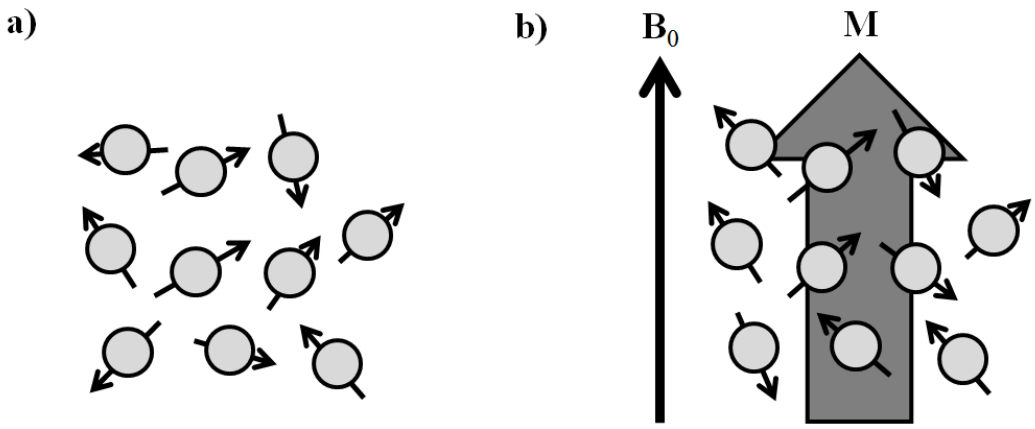

Figure 6: A schematic representation of nuclear spins a) before and b) after the application of an external static magnetic field, B_0. The magnetic moments of the nuclear spins are randomly oriented in the absence of B_0, resulting in a trivial net magnetisation due to the Earth's magnetic field, while in the presence of B_0, the magnetic moments tend to align with B_0 resulting in a net magnetisation, M.

It is necessary to be able to detect the net magnetisation to extract information from the sample. As only the transverse component of the net magnetisation is detectable (i.e., the component orientated perpendicular to $\mathbf{B}_0$), an NMR experiment begins by nutating **M** away from $\mathbf{B}_0$ using a perpendicular magnetic field, $\mathbf{B}_1$, oscillating at the Larmor frequency for a short period of time. This short burst of an oscillating perpendicular magnetic field can be achieved by a radio-frequency (rf) pulse. The resonance between the rf pulse and the Larmor frequency of the nuclei results in a continuous push of the net magnetisation towards the transverse plane, resulting in a transverse magnetisation magnitude, M_{xy}. In NMR, it is common to name the rf pulse based on the angle by which the net magnetisation is rotated (e.g., 90 or 180° pulses, or equivalently π/2 and π pulses, as shown in Figure 7).

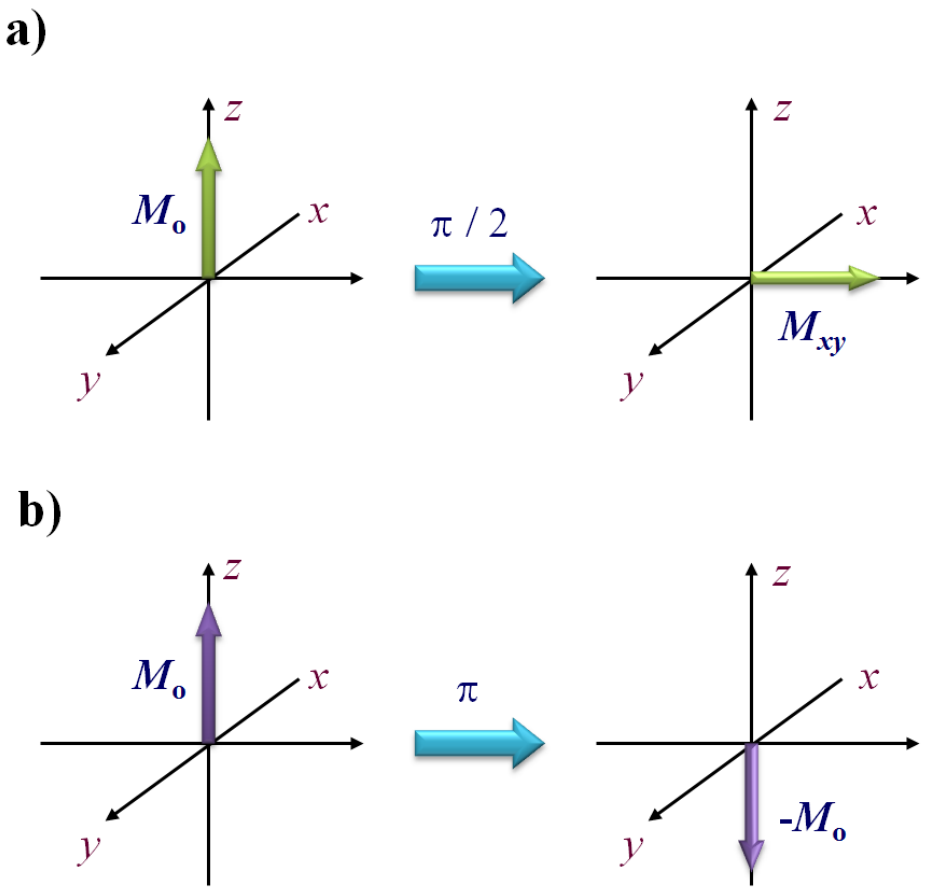

Figure 7: The effect of two common rf pulses on the net spin magnetisation at thermal equilibrium: a) 90° pulse maximising the magnetisation component in the *x*,*y*-plane, where the NMR signal is detected. b) 180° pulse inverting the spin-populations.

During the application of an rf pulse, two precessions are involved: one about $\mathbf{B}_0$ and one about $\mathbf{B}_1$. In the laboratory frame of reference, two simultaneous precessions make the overall motion of the net magnetisation appear as a spiral. In such situations, this can be visualised more simply by considering a frame of reference rotating at the Larmor frequency. In a rotating frame of reference, the spins precessing about $\mathbf{B}_0$ will appear stationary. The rotating frame of reference accounts for the effects of $\mathbf{B}_0$, thus $\mathbf{B}_0$ can be ignored. Furthermore, in the rotating frame, the rf pulse will appear to be static and the net magnetisation will appear to only precess about $\mathbf{B}_1$, thus simplifying the initial two precessions to one.

After the rf pulse is turned off, the net magnetisation, which is now in the transverse plane, continues its usual precession about $\mathbf{B}_0$. A changing magnetic field is generated by this precessing magnetisation, which induces an oscillating electric current via Faraday induction in a nearby receiver coil of the NMR spectrometer. This induced current is then digitised to form the NMR signal commonly referred to as the free induction decay (FID). As it is difficult to deduce the Larmor frequencies of nuclei in different environments from the FID, the FID is Fourier transformed to the frequency domain [68]. The essence of Fourier transform involves multiplying the FID by trial cosine waves to pick out the intensity of the corresponding frequency. This mathematical process results in the conversion of the exponentially decaying signal to a Lorentzian-shaped peak (Figure 8). This forms the NMR spectrum, where the Larmor frequencies can be easily identified by the corresponding peak [68, 69].

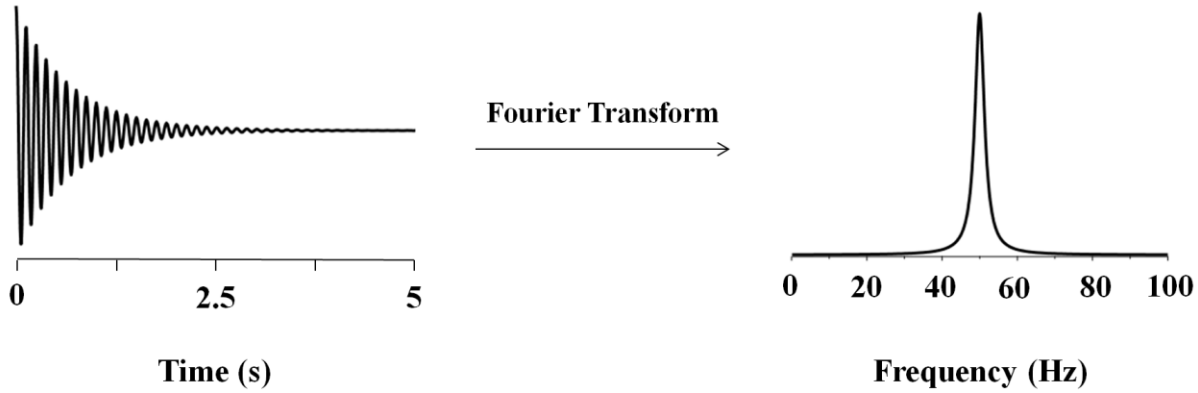

Figure 8: A simulated free induction decay (left) Fourier transformed to obtain the NMR spectra (right). The offset Larmor frequency was set to 50 Hz.

2.2 Relaxation

During the acquisition of an FID, the magnetisation returns to equilibrium by a process known as spin relaxation. There are two primary forms of relaxation; spin-lattice relaxation (returning of the longitudinal magnetisation to its equilibrium value) and spin-spin relaxation (reduction of the transverse magnetisation to zero). The time required for spin-lattice relaxation and spin-spin relaxation to occur is denoted by the decay constants T_1 and T_2, respectively, which observes the rotational motion of molecules and can be used to probe the molecular dynamics of solutions. The two relaxation processes are outlined in Figure 9.

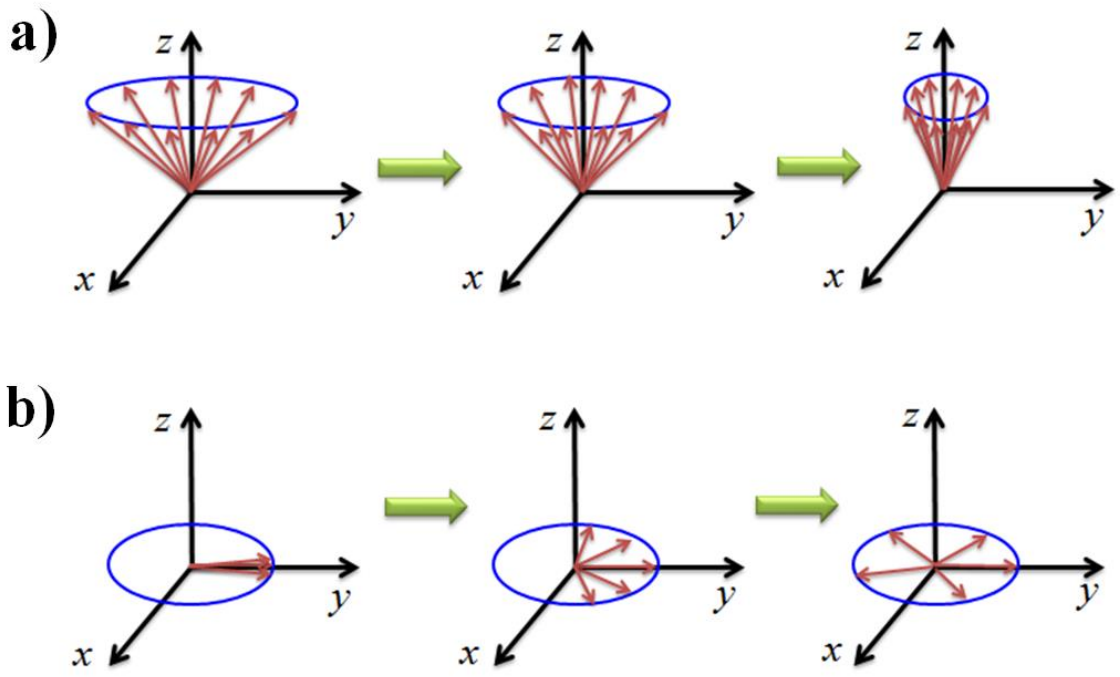

Figure 9: A schematic representation of the relaxation processes: a) spin-lattice relaxation and b) spin-spin relaxation. Spin-lattice relaxation is the return of the longitudinal magnetisation (depicted by the sum of the vertical components of the red arrows in (a)) to its equilibrium value along the *z*-axis, while spin-spin relaxation is the reduction of the transverse magnetisation (depicted by the dephasing of the red arrows in (b)) to zero in the *xy*-plane (from left to right).

2.2.1 Spin-Lattice Relaxation

The spin-lattice relaxation time, T_1, quantifies the rate at which energy is transferred from the nuclear spin system to the neighboring molecules (i.e., the lattice). This is relaxation in the *z*-direction. On the microscopic scale, spin-lattice relaxation refers to the movement of spin populations back to their Boltzmann distribution values [70]. The return of the magnetisation in the *z*-component, M_z, to its equilibrium value, M_0, can be described by the first-order process [70, 71]

$$\frac{dM_z}{dt} = -\frac{(M_z - M_0)}{T_1}. \tag{2.2}$$

After a period of time equivalent to T_1, M_z returns to 63% of its equilibrium value. Experimentally, it is therefore common practice to set a delay of $3-5\times T_1$ to ensure M_Z has almost returned to 100% of its equilibrium value.

2.2.2 Spin-Spin Relaxation

Spin-spin relaxation corresponds to the loss of transverse magnetisation, resulting from the loss of coherences amongst the spins precessing in the *x*-*y* plane. The loss of magnetisation in the *x* and *y* components can be described by the first order processes [70, 71]

$$\frac{dM_x}{dt} = \frac{M_x}{T_2} \text{ and } \frac{dM_y}{dt} = \frac{M_y}{T_2}. \tag{2.3}$$

Similar to spin-lattice relaxation, the signal decay resulting from spin-spin relaxation is described mathematically by an exponential curve. However, T_2 differs from T_1 in that the signal is reduced to 37% of its original value after a time period of T_2 (whereas with T_1, 63% of the signal is recovered after a time period of T_1).

2.2.3 Pulse Sequences for Studying NMR Relaxation

2.2.3.1 Inversion Recovery Pulse Sequence

The inversion recovery method is the most commonly used method to measure T_1 [72]. The inversion recovery pulse sequence consists of a π pulse, followed by a $\pi/2$ pulse after a time delay of τ, as shown in Figure 10.

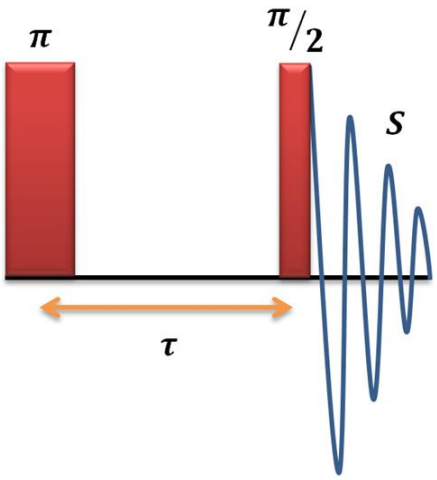

Figure 10: The inversion recovery pulse sequence. The π pulse inverts the magnetisation from the *z* to the –*z* axis. During time τ, the magnetisation relaxes back to equilibrium, after which the π/2 pulse is applied to rotate the magnetisation into the *x*-*y* plane for signal detection. The decaying sinusoid at the end of the sequence represents the acquired signal, *S*.

A profile of the recovery of the longitudinal magnetisation can be obtained by repeating the sequence with different τ delays. The intensity of the observed longitudinal magnetisation, M_z is described by [70]

$$M_z(\tau) = M_0(1-2e^{-\tau/T_1}). \tag{2.4}$$

Eq. (2.4) can then be regressed onto the longitudinal magnetisation recovery profile to determine T_1 (Figure 11).

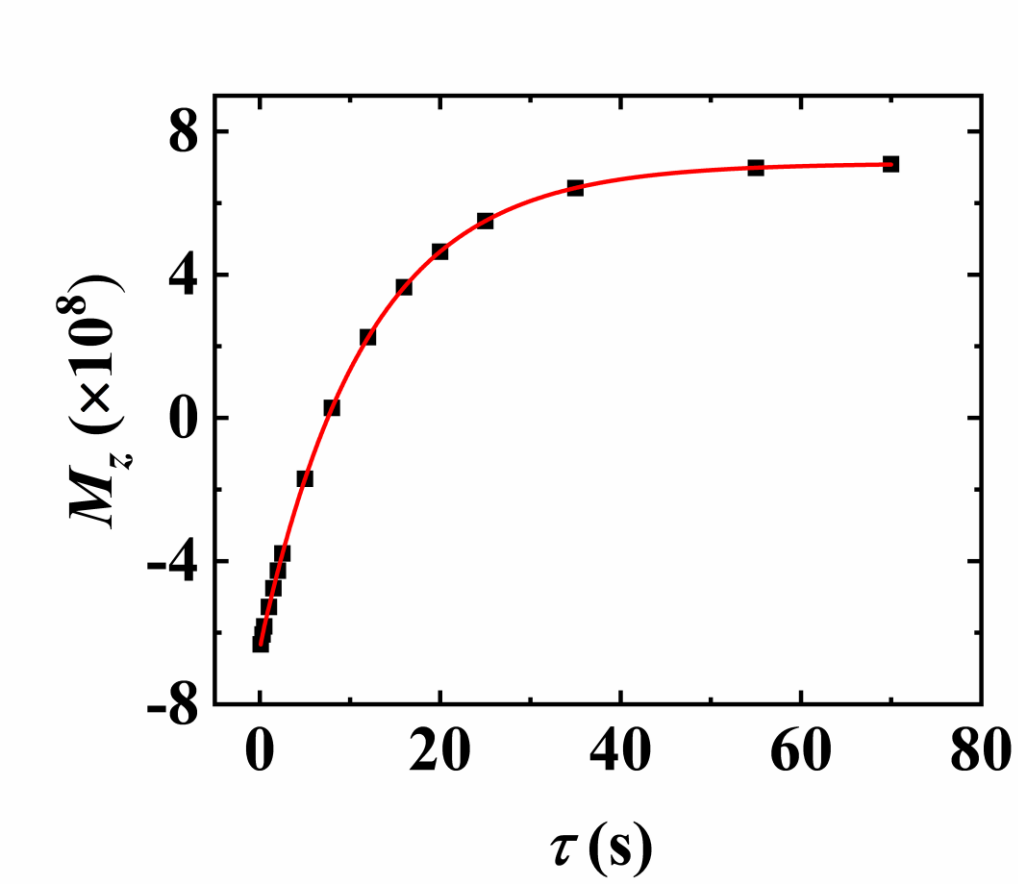

Figure 11: Non-linear regression of Eq. (2.4) to the longitudinal magnetisation recovery profile of 0.03 M 2-nitroimidazole in D_2O (298 K) using 16 values of τ ranging from 0.1 – 70 s to obtain a T_1 of (10.60 ± 0.01) s.

When obtaining a longitudinal magnetisation recovery profile, each repetition of the pulse sequence is separated by a recycle delay of $\geq 5\times T_1$ to ensure that the magnetisation has returned to equilibrium. Prior to determining T_1, $5\times T_1$ can be estimated with the relationship

$$T_1 = \frac{\tau_{null}}{\ln(2)}, \tag{2.5}$$

where τ_{null} is the time delay at which zero (or minimal positive) signal is obtained. Whether a signal is positive or negative is determined by τ relative to τ_{null}.

2.2.3.2 Carr-Purcell-Meiboom-Gill Pulse Sequence

The Carr-Purcell-Meiboom-Gill (CPMG) pulse sequence is the most commonly used method to measure T_2. This pulse sequence consists of a $\pi/2$ pulse, followed by a series of π pulses, as shown in Figure 12.

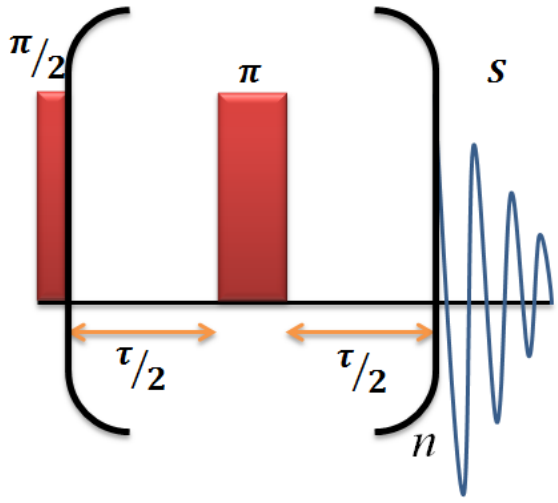

Figure 12: The Carr-Purcell-Meiboom-Gill (CPMG) pulse sequence consisting of a π/2 pulse and *n* repetitions of the Hahn spin-echo unit (τ/2-π-τ/2).

The number of echo cycles is varied in an arrayed fashion. The exponential decay curve is obtained by plotting the intensities of the echo signals against τ. T_2 can be determined by regressing

$$M_{xy}(\tau) = M_0 e^{\left(-\tau/T_2\right)} \tag{2.6}$$

onto the magnetisation decay curve (Figure 13).

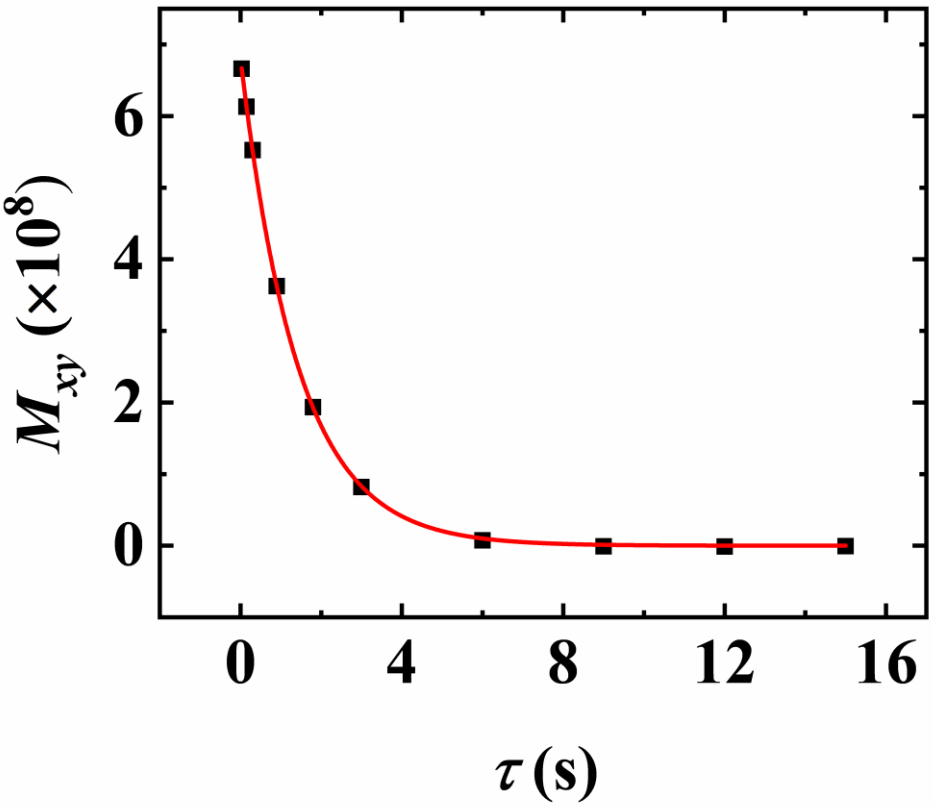

Figure 13: Non-linear regression of Eq. (2.6) to the transverse magnetisation decay profile of 0.03 M 2-nitroimidazole in D_2O (298 K) using 10 values of τ ranging from 0.03 – 15 s to obtain a T_2 of (1.427 ± 0.005) s.

The CPMG sequence is a modification of the spin-echo pulse sequence first proposed in 1950 by Erwin Hahn comprising two π/2 pulses with $\tau/2$ delays in between the pulses and prior to acquisition [73]. The first π/2 pulse excites the net magnetisation to precess in the transverse plane. However, due to magnetic field inhomogeneities and different chemical shifts in the case of multiple resonances, the magnetisation components begin to precess at slightly different rates. Hence, the Hahn spin echo sequence was modified by replacing the second π/2 pulse with a π pulse [74], which inverts the magnetisation and refocusses the components. However, this modified sequence is still prone to diffusion artefacts (i.e., different static fields due to self-diffusion). To accommodate for these artefacts, Carr, Purcell, Meiboom and Gill shifted the phase of the rf of the π/2 pulse by π/2 relative to the phase of the π pulses [75] and repeated the echo cycle multiple times.

2.3 Diffusion

Diffusion, or more specifically self-diffusion, is a type of translational motion, describing the random thermal motion of molecules or small particles at thermal equilibrium (Figure 14) [76, 77]. In diffusion, no bulk displacement occurs, which is different from other types of motion, such as mechanical displacement of solid bodies or advection in liquids [78]. As there is no bulk displacement, diffusion can be assessed by measuring the mean squared displacement (MSD) of single diffusing particles. While the mathematical basis of diffusion is presented in Chapter 5, for now, it will suffice to know that diffusion is characterised by a diffusion coefficient, D (m^2s^{-1}), and can be physically interpreted through the Stokes-Einstein-Sutherland equation [79-81],

$$D = \frac{kT}{6\pi\eta r} \tag{2.7}$$

where k is the Boltzmann constant, T is the temperature, η is the solvent viscosity, and r is the Stokes (or effective hydrodynamic) radius of the diffusing species. Typical diffusion coefficients in aqueous solutions range from 10^{-11} (e.g., large protein molecules: albumin) to 10^{-9} m^2s^{-1} (e.g., water) [82-84]. Diffusion measurements can be used to probe the molecular dynamics of processes ranging from large-scale water management [85] to protein interactions [86, 87].

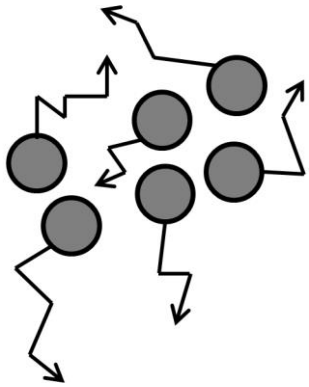

Figure 14: A schematic representation of molecular diffusion, with the arrows depicting the random thermal motion of the molecules.

2.3.1 Diffusion NMR Pulse Sequences

The use of magnetic field gradients to measure diffusion coefficients was initiated by Erwin Hahn with the discovery of the spin-echo [76]. Spin-echoes originate from a refocusing of the spin magnetisation after dephasing due to either spin-spin relaxation or gradient pulses [88]. NMR diffusion measurements are mostly commonly obtained using Pulsed Gradient Spin-Echo (PGSE) or Pulsed Gradient Stimulated Echo (PGSTE) sequences (Figure 15).

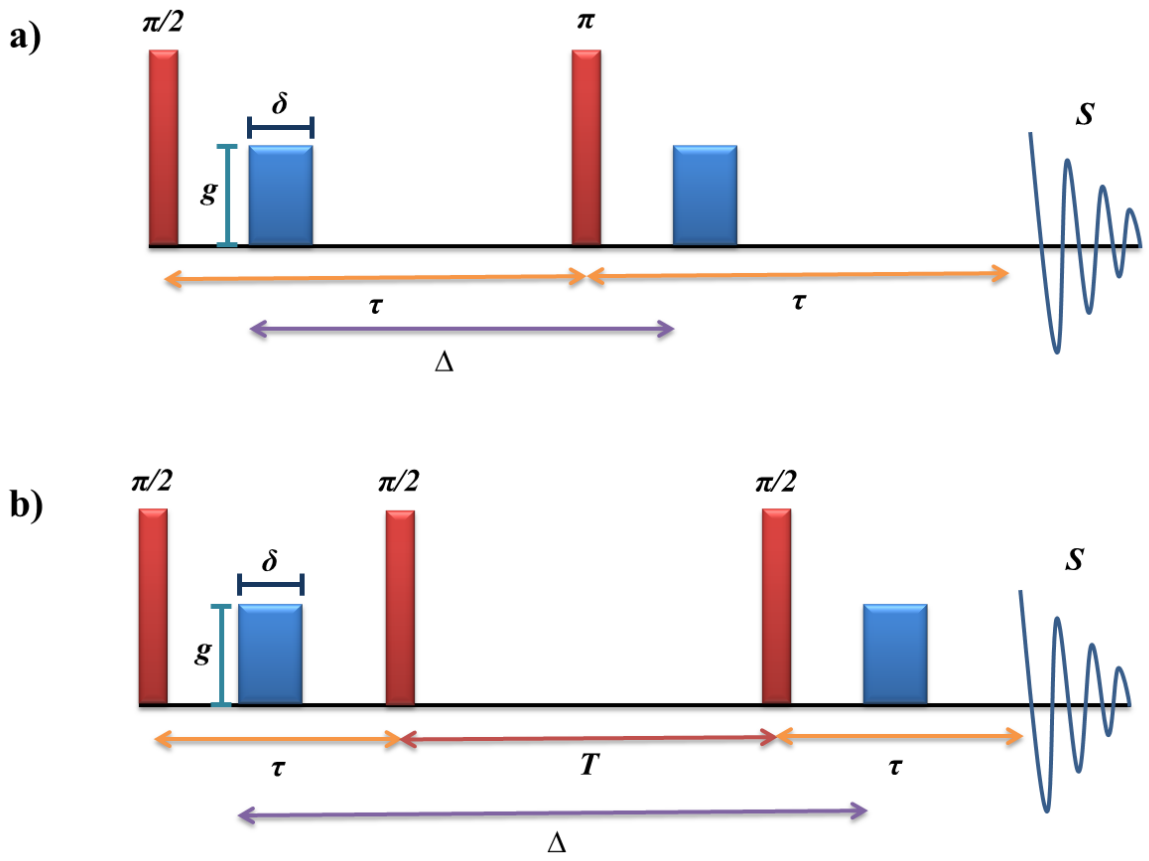

Figure 15: a) A PGSE pulse sequence with π/2 and π rf pulses and magnetic gradient pulses of magnitude, *g* and duration, *δ*. The timescale of the diffusion measurements is represented by Δ. b) A PGSTE pulse sequence, which differs from the PGSE sequence with two π/2 pulses replacing the π pulse, forcing the magnetisation onto the *z*-axis and then onto the *x*-*y* plane. In this sequence, the spin magnetisation is subject to spin-spin relaxation during the *τ* delays and spin-lattice relaxation during the *T* delay. *S* denotes the acquired signal. Typically *δ* is in the range of 0-10 ms, Δ is in the range of ms to s and *g* ranges from 0 to 20 Tm^{-1} [76, 89].

In the PGSE sequence, the *π*/2 rf pulse flips the net spin magnetisation (initially oriented along the static magnetic field) into the transverse plane. The first gradient pulse

then winds the magnetisation into a helix (Figure 16). This will be discussed further in Section 3.1.1. During Δ, translational diffusion will attenuate the radius of the helix. The π rf pulse will then change the chirality of the helix. The application of the second gradient pulse unwinds the magnetisation, at which point the signal is acquired. The PGSTE sequence is similar to the PGSE sequence in the application of the gradient pulses, but differs in the application of the rf pulses. Similar to the PGSE, the first $\pi/2$ rf pulse of the PGSTE flips the spin magnetisation into the transverse plane. The π rf pulse of the PGSE is then replaced by two separated $\pi/2$ rf pulses. The magnetisation is thus stored longitudinally during the bulk of the diffusion time and has a sinusoidal dependence (in contrast to the helical magnetisation arising during the PGSE sequence). The third $\pi/2$ rf pulse flips the magnetisation back into the transverse plane, but in the opposite direction to the first $\pi/2$ rf pulse. The signal is then acquired. It is important to note that the two extra $\pi/2$ pulses in the PGSTE sequence have the same combined effect as the π pulse with regard to gradients winding and unwinding the magnetisation helix. However the PGSTE is advantageous in that it caters for systems with a large T_1 relative to their T_2 (i.e., $T_1 >> T_2$) [89].

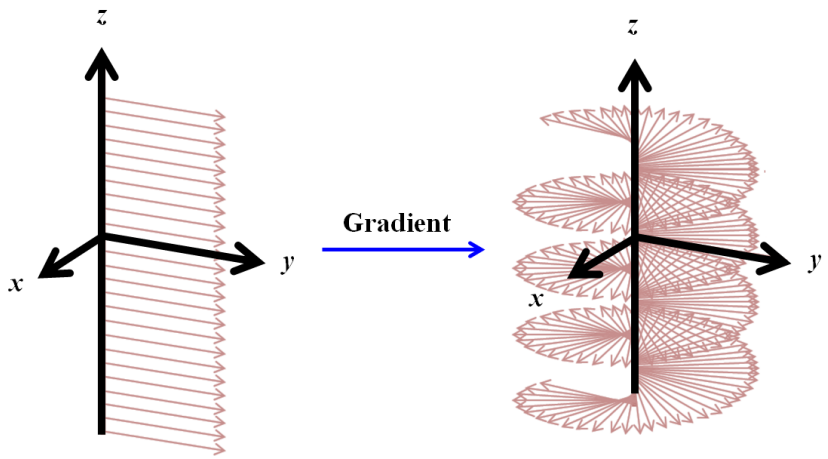

Figure 16: Schematic representation of the formation of a magnetisation helix following the application of a gradient pulse. Prior to the application of any pulses, the net magnetisation is initially oriented in the direction of the static magnetic field (i.e., B_0). The application of the rf pulse flips the net magnetisation into the transverse plane (left), after which the application of a gradient pulse winds the magnetisation vectors into a helix.

Experimentally, a series of measurements can be performed with different magnetic field gradients, g. This results in different amplitudes of the acquired signal, which can be described by the modified Stejskal-Tanner expression [76, 90],

$$S = M_0 \exp\left(-(\gamma\delta g)^2 D\left(\Delta - \frac{\delta}{3}\right)\right), \tag{2.8}$$

where γ is the gyromagnetic ratio. Eq. (2.8) is then normalised (e.g. to the signal acquired without an applied gradient, $S_{g=0}$), giving the attenuation of the echo signal, E,

$$E = \frac{S}{S_{g=0}} = \exp(-bD). \tag{2.9}$$

where $b = (\gamma\delta g)^2 (\Delta - \delta/3)$. D can then be determined using a non-linear regression of Eq. (2.9) to the echo attenuation data obtained at each gradient, as shown in Figure 17.

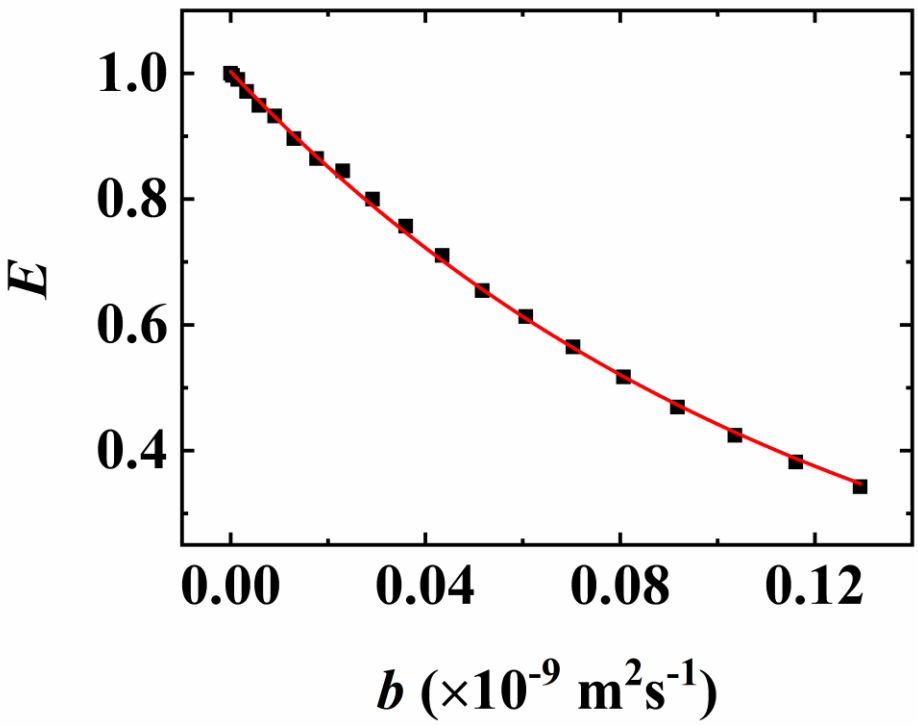

Figure 17: Non-linear regression of the modified Stejskal-Tanner expression to the echo attenuation data of 0.16 M 2-nitroimidazole in D_2O (298 K) obtained at 20 magnetic field gradients ranging from 0.001 – 0.531 Tm^{-1} to obtain the diffusion coefficient of (8.19 ± 0.06) × 10^{-10} m^2s^{-1}.

Chapter 3. Magnetic Resonance Imaging

As NMR underpins the concepts of MRI, this chapter will build on the concepts of Chapter 2, and develop the fundamentals of MRI, which is the chosen method for *in vitro* observation of the synthesised hypoxia-targeting paramagnetic agent in this thesis. The MRI techniques that will be used later in this project will also be introduced.

3.1 Fundamental MRI Theory

Since 1973, the capabilities of NMR to map the spatial distribution of substances within an object has been developed as an imaging method [91-93]. Conceptual and technological advancements have allowed this imaging method, known as MRI to become one of the most important and versatile techniques in diagnostic medicine. Numerous imaging modalities are available for probing the human body. However, MRI is advantageous in that it is non-invasive, does not use ionizing radiation and provides excellent soft tissue contrast.

3.1.1 One-Dimensional Imaging

In the previous chapter, it was explained how an NMR spectrum of a sample can be obtained. In this chapter, this concept is extended to obtain an image of the sample. To explain the concept of imaging, nuclear spin density, ρ, must first be defined. Spin density refers to the number of nuclei in a given voxel, which in simple terms is a 3D equivalent of a pixel. Hence, a higher spin density results in higher signal intensity in an MRI image. The primary objective of imaging is to obtain information relating to ρ at each point, $\mathbf{r}$, in the sample (i.e., $\rho(\mathbf{r})$). To do so, the signals from nuclear spins need to be spatially differentiated. This can be done by applying a magnetic gradient, $\mathbf{G}$, thus varying the external magnetic field in a defined direction [94]. As ω_0 is proportional to the magnetic field experienced by the nuclei, the presence of a gradient allows ω_0 to be expressed as a function of position, $\mathbf{r}$ [93],

$$\omega_0(\mathbf{r}) = \gamma \mathbf{B}_0 + \gamma \mathbf{G} \cdot \mathbf{r}. \tag{3.1}$$

Hence, with an application of a gradient, planes of constant field strength also become planes of constant resonance frequency. This relationship between the spatial domain and the frequency domain in the presence of a gradient forms the fundamental principles of MRI. It can be seen from Eq. (3.1) that a distribution of resonance frequencies will be observed in the NMR spectrum obtained in the presence of a gradient.

This then allows ρ to be determined from the acquired NMR signal. Assuming $\mathbf{G}$ is constant, the acquired signal can be expressed as

$$S(t) \propto \int M_T(0) e^{-i\gamma(\mathbf{G}\cdot\mathbf{r})t} d\mathbf{r}$$
$$\sim \int \rho(\mathbf{r}) e^{-i\gamma(\mathbf{G}\cdot\mathbf{r})t} d\mathbf{r}. \tag{3.2}$$

The number of contributing nuclei in the constant-frequency plane will be proportional to the spectral amplitude at each frequency. Hence, the NMR spectrum of an object in the presence of a gradient corresponds to the projection of spins along the direction of the gradient, as shown in Figure 18.

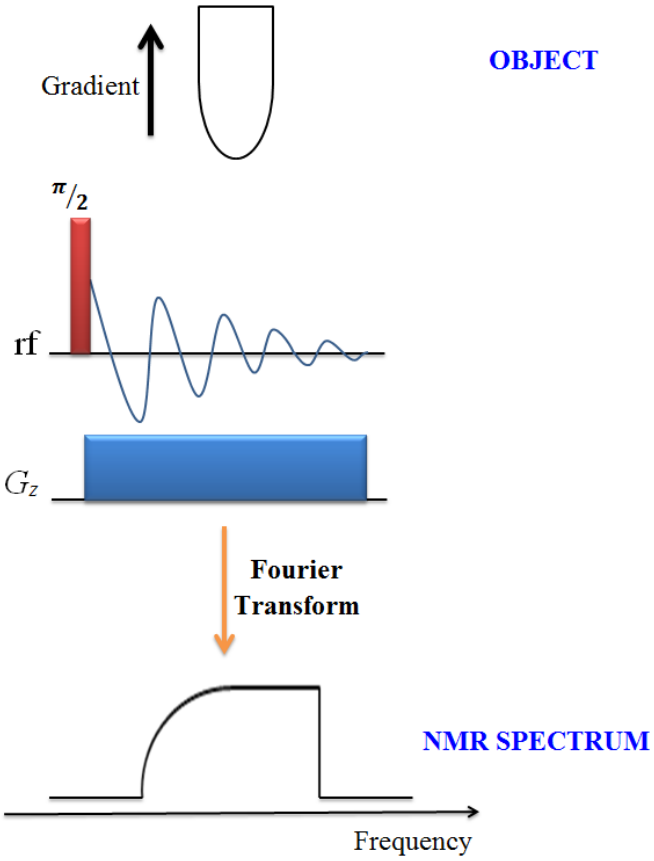

Figure 18: A schematic showing the use of a magnetic gradient to obtain a one-dimensional image in the form of an NMR spectrum, where the gradient and the external magnetic field are applied in the *z*-direction. As the Larmor frequency becomes a function of the *z*-position due to the applied gradient, the NMR spectrum represents the distribution of the Larmor frequencies with the signal-amplitude at each frequency proportional to the number of spins in that frequency region. The 1D projection of ρ in the direction of the gradient is the image.

3.1.2 Multi-Dimensional Imaging

The spatial information of one-dimensional objects can be accurately obtained from one-dimensional images. However, one-dimensional projection images of two or three-dimensional objects cannot be obtained, as the internal structures on different planes cannot be visualised. Therefore, imaging a two-dimensional object requires a procedure capable of identifying the coordinates of the volume elements that span two dimensions, and three in the case of three-dimensional objects. To account for the spatial axes in three dimensions, the application of three orthogonal gradients is required. These gradients can be described as slice selective, frequency encoding and phase encoding gradients.

3.1.2.1 Slice Selection

Slice selection is used to selectively excite the equilibrium magnetisation corresponding to a thin slice of an object. This involves applying a gradient (i.e., the slice gradient) along (in this case) the *z*-axis in conjunction with a frequency selective rf pulse. As depicted in Figure 19, the precession frequency of the spins is varied by the slice gradient, G_z, while only the spins with the selected frequency range are rotated into the transverse plane by the rf pulse. This results in only a limited part of the sample (i.e., the slice) being excited. As only the magnetisation from the slice is rotated into the transverse plane, it is the only contribution to the NMR signal. The thickness of the slice, Δz, can be adjusted by changing the frequency width of the rf pulse, $\Delta\omega_{rf}$, and the strength of the applied gradient [93, 95],

$$\Delta z = \frac{\Delta\omega_{rf}}{\gamma G_s}. \tag{3.3}$$

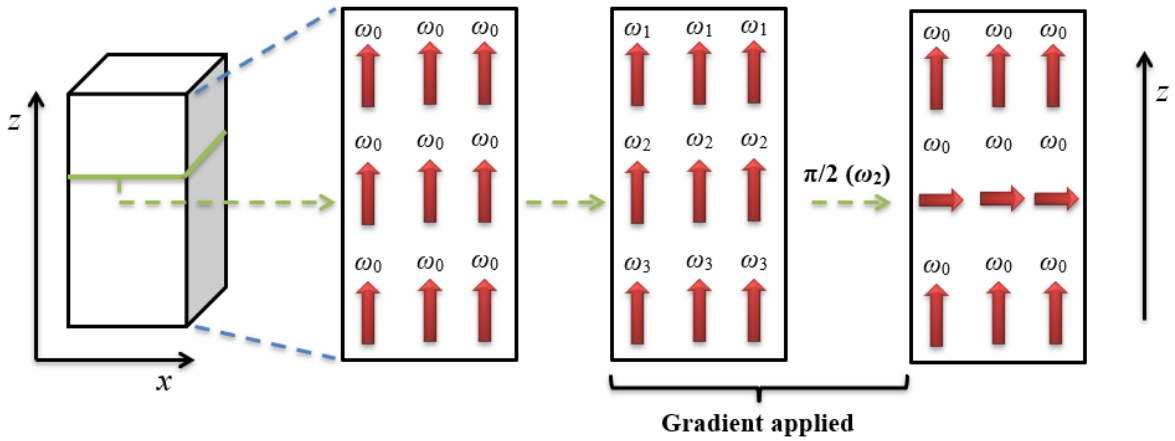

Figure 19: A schematic representation of the slice selection process along the *z*-axis. The spins (represented by the arrows) are initially precessing at ω_0. The application of the slice selective gradient causes the spins at different *z*-positions to precess at slightly different frequencies (ω_1, ω_2 and ω_3). If a frequency selective rf pulse is applied at ω_2, only the corresponding spins are rotated into the transverse plane, thus selecting the slice (denoted as the region in green on the 3D block).

3.1.2.2 Frequency Encoding

In this chapter, the frequency encoding gradient will be considered to be applied along the *x*-axis. The application of the gradient results in the Larmor frequencies of the voxels becoming spatially dependent along the *x*-axis. This is similar to the effect that was discussed for one-dimensional imaging with the exception that the spatial dependence is along a particular axis (in this case, *x*). Hence, Eq. (3.1) can be written as

$$\omega_0(x) = \gamma \mathbf{B}_0 + \gamma G_f x, \tag{3.4}$$

where G_f is the frequency gradient [93, 95]. This process is referred to as frequency encoding and is shown in Figure 20.

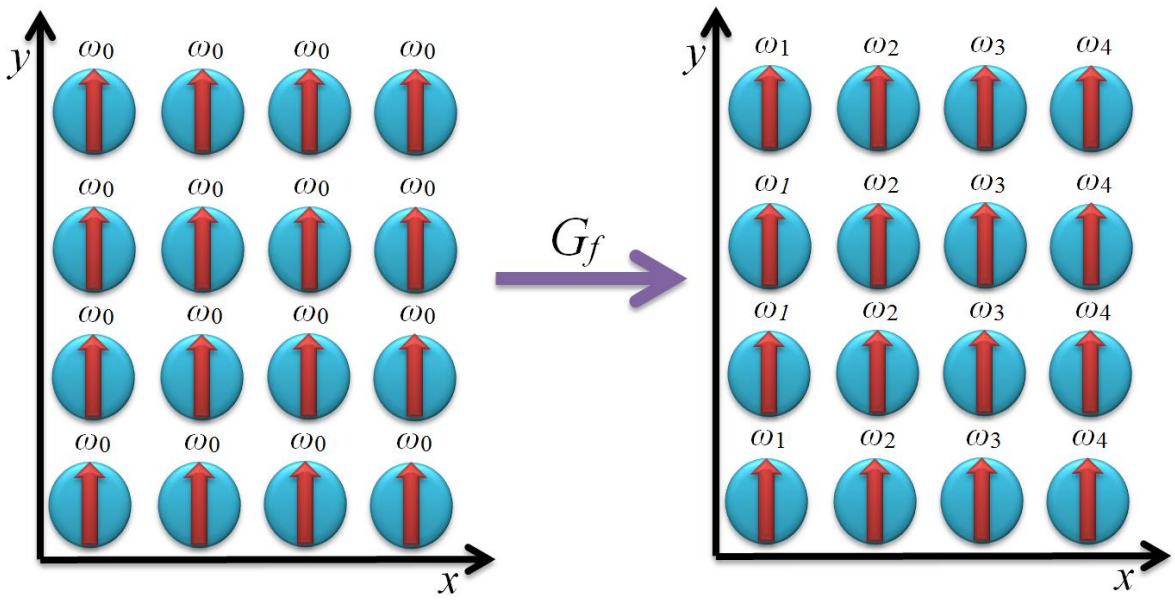

Figure 20: A schematic representation of frequency encoding along the *x*-axis following the application of a frequency encoding gradient. The red arrows denote the phase, which is not changed during the frequency encoding process.

3.1.2.3 Phase Encoding

As the frequency encoding gradient was considered to be applied along the *x*-axis, the phase encoding gradient will be considered to be applied on the *y*-axis. For such a gradient applied for a fixed time, *t*, the phase, φ, prior to signal acquisition can be expressed as a function of position *y* [93, 95],

$$\varphi(y) = \gamma \int_0^t \left(B_0 + G_\varphi y \right) dt \tag{3.5}$$

where G_φ is the phase gradient. In the presence of a phase gradient, the nuclear spins will begin to precess at slightly different frequencies along the *y*-axis. This will in turn generate different spin phases along the *y*-axis. When the phase gradient is removed, the spin will return to the frequency that was present prior to the application of the phase gradient, but will maintain the phase differences that were generated by the phase gradient. This process is referred to as phase encoding (Figure 21).

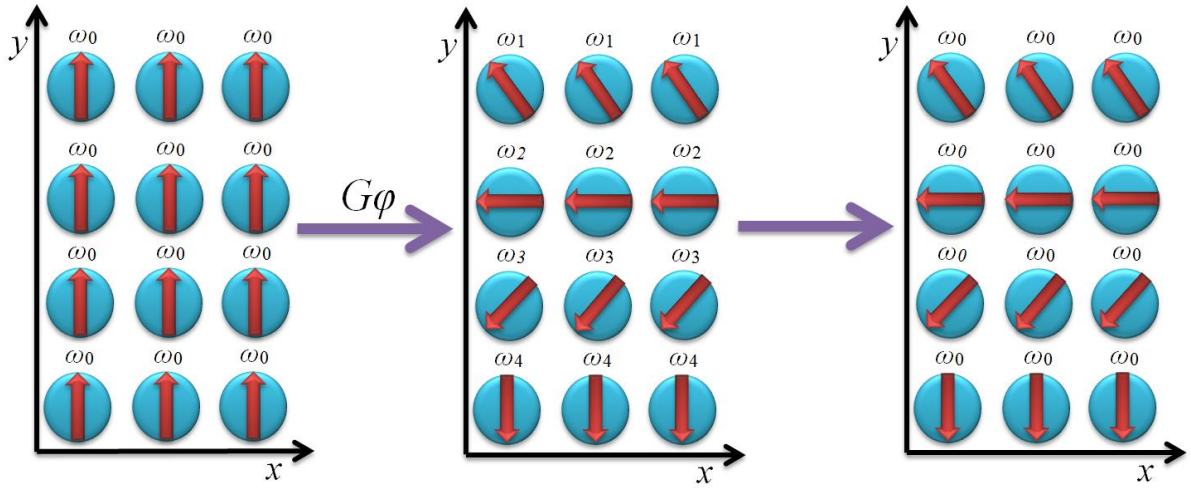

Figure 21: A schematic representation of phase encoding along the *y*-axis following the application of a phase encoding gradient. The application of the gradient results in a change in the frequency and hence phase of the spins along the *y* axis. Removing the gradient returns the frequency to ω_0, however the phase differences are retained as a function of position.

3.1.3 MRI Pulse Sequences

Two basic MRI pulse sequences, which form the basis of many others, are the spin-echo and gradient-echo pulse sequences, as shown in Figure 22 and Figure 23, respectively. It should be noted that in the discussion above and the following figures, the frequency, phase and slice gradients have been assumed to be along the *x*, *y* and *z*-axes, respectively. However, in practice, the three gradients can be applied along any three orthogonal directions.

In the spin-echo sequence, the sign of the magnetic gradient is effectively negated by the π pulse, and phase dispersion due to magnetic inhomogeneities, chemical shifts and gradient-induced dispersions are refocussed [92, 96, 97]. In the gradient-echo sequence, only gradient-induced dispersions are refocussed.

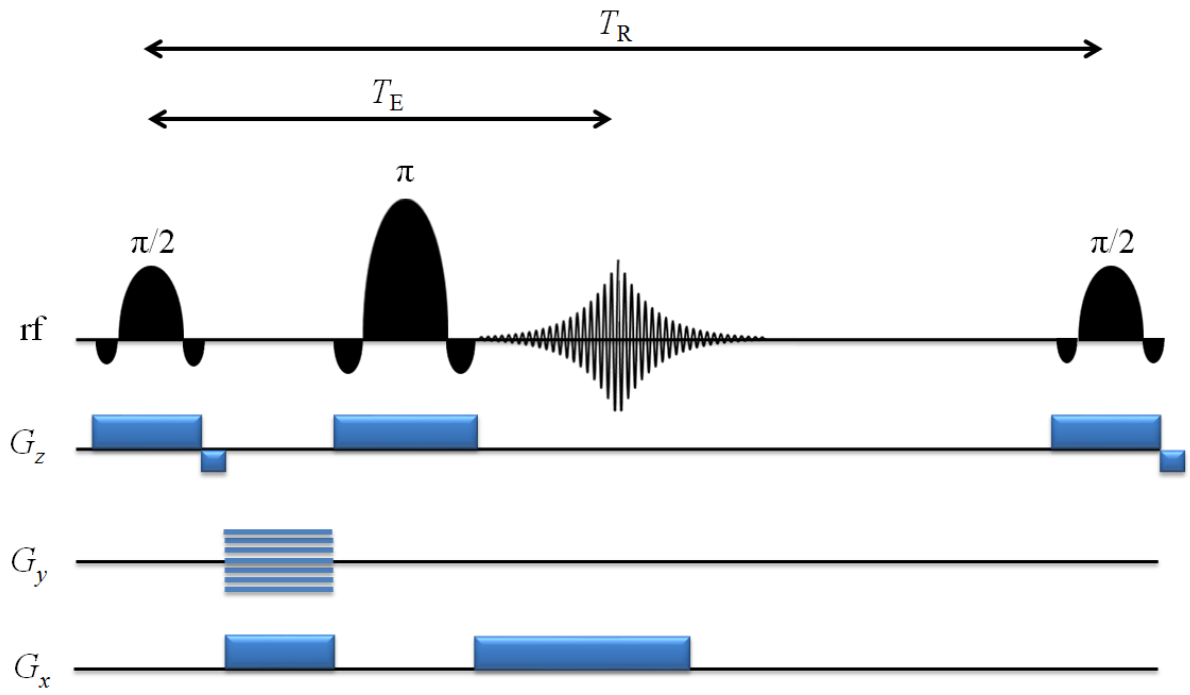

Figure 22: A spin-echo MRI pulse sequence. A short negative slice selective gradient is applied following the π/2 rf pulse to refocus the magnetisation that has been dephased due to the application of the π/2 rf pulse. Equally spaced stacked lines have been used to represent the phase gradient to show that its magnitude is increased gradually when the sequence is repeated. In this sequence, the π pulse refocusses phase dispersion originating from magnetic inhomogeneities, chemical shifts and gradient-induced dispersions. T_E is the echo time (i.e., the time between the application of the first rf pulse and the acquisition of the signal) and T_R is the repetition time.

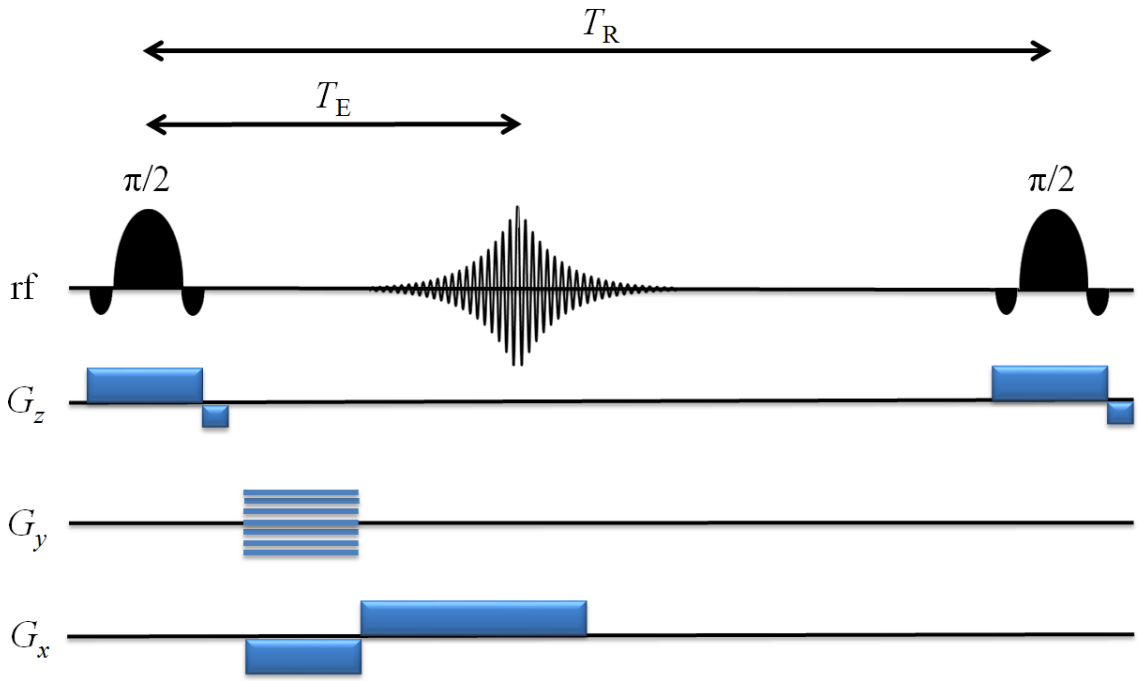

Figure 23: A gradient-echo MRI pulse sequence. The frequency-encoding gradients have been presented above and below the line to indicate antiphase gradients, which only refocus gradient-induced dispersions.

3.1.4 Image Reconstruction

The frequency encoded signal, which exists in the form of a time-dependent MR signal, is transformed into its different frequency components using Fourier transformation as shown in Figure 24. The relative amount of signal at each location along the frequency encoding gradient can be determined by mapping the amplitude of each frequency component. The range of frequencies across the defined field of view (FOV) in the frequency encoding direction is known as the receiver bandwidth and is determined by the amplitude required for the frequency encoding gradient [98].

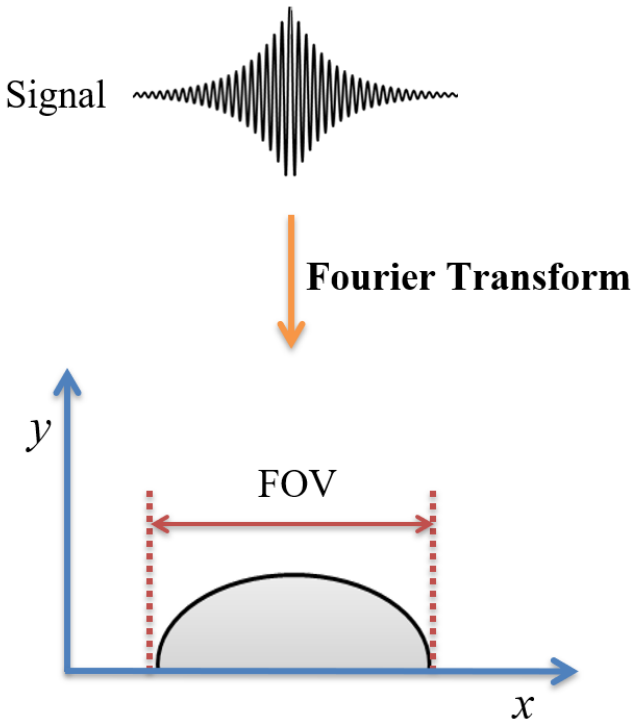

Figure 24: The frequency encoded signal is analysed by Fourier transformation, measuring the signal amplitude to map the contribution of each of the frequency components along the frequency encoding gradient (within the FOV). In the schematic, the *x* axis represents the frequency while the *y* axis represents the signal amplitude.

A similar process cannot be used to decode the phase changes imparted by the phase encoding gradient, as Fourier transform can only analyse a signal that changes over time. To allow the phase data to be analysed by Fourier transformation, a number of signal echoes are generated by repeating the pulse sequences discussed earlier. The time interval between each repetition is the repetition time, T_R. At each repetition, the slice selection and frequency encoding gradients are kept constant, while the phase encoding gradient is increased in equal increments from negative to positive, as depicted in Figure 25. The signal echo is measured for each phase encoding step and stored in a raw data matrix. After the signal for each of the phase encoding steps have been acquired and stored, it is analysed by a two-dimensional Fourier transform to decode both the frequency and phase information.

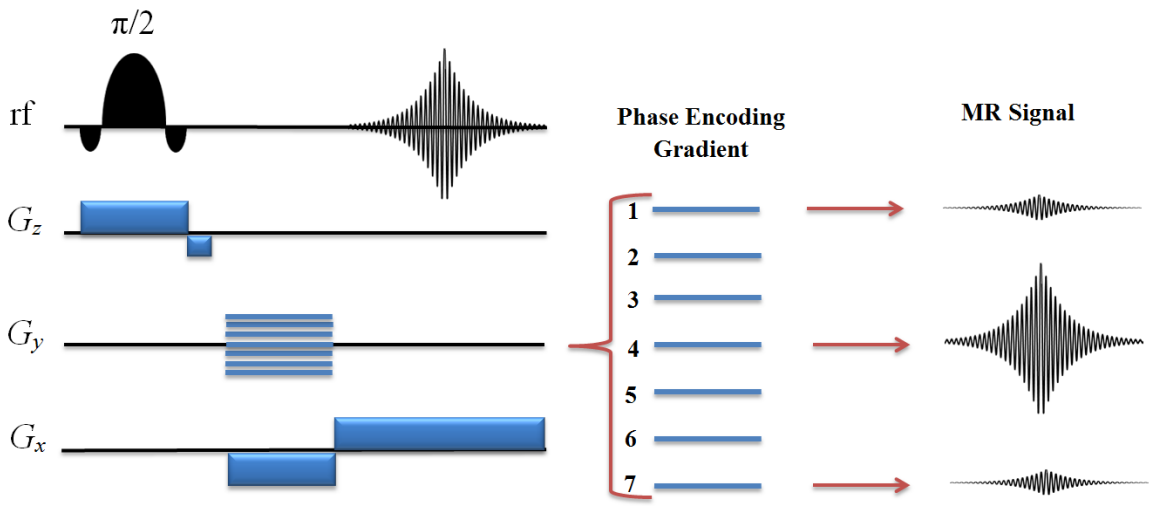

Figure 25: To acquire sufficient information for image reconstruction, the pulse sequence is repeated a number of times. At each repetition, the strength of the phase encoding gradient is increased from negative to positive. In the schematic, 7 increments are used for the phase encoding gradient. As the strength of the gradient is increased (either positive or negative), the amount of dephasing along the gradient also increases. As shown by the MR signals, the phase encoding gradient labelled 4 is of strength zero, resulting in no dephasing of the signal, hence producing a signal of maximum amplitude.

3.1.4.1 Repetition Time and Image Acquisition Time

In addition to determining the time required for MR images to be acquired, T_R also affects image contrast. The number of phase encoding steps, N_p, determines the number of pixels in the phase encoding direction of the reconstructed image. The spatial resolution of the image therefore depends on the number of phase encoding steps, which in most cases is limited by the image acquisition time, T_{aq},

$$T_{aq} = T_R \times N_p. \tag{3.6}$$

Hence if greater spatial resolution in the phase encoding direction is required, the number of pixels in that direction must be increased, resulting in a greater number of repetitions and a longer T_{aq}.

3.1.4.2 k-Space

The use of magnetic field gradients to generate and encode MR signals give rise to a particular relationship between the data points in the signal and the image. In image space, each pixel occupies a unique location. Similarly, each point of an MR echo signal belongs to

a unique location in a space referred to as k-space (Figure 26) [99]. Each point in k-space represents the particular spatial frequency contained within the corresponding image [98].

An image with a single spatial frequency can be pictured as a wave propagating across the image with bright and dark peaks and troughs. Peaks and troughs positioned far apart represent a low spatial frequency. This mainly contributes the signal content and contrast of the image. Conversely, peaks and troughs positioned close together represent a high spatial frequency. This defines the fine details, thus defining the spatial resolution of the image.

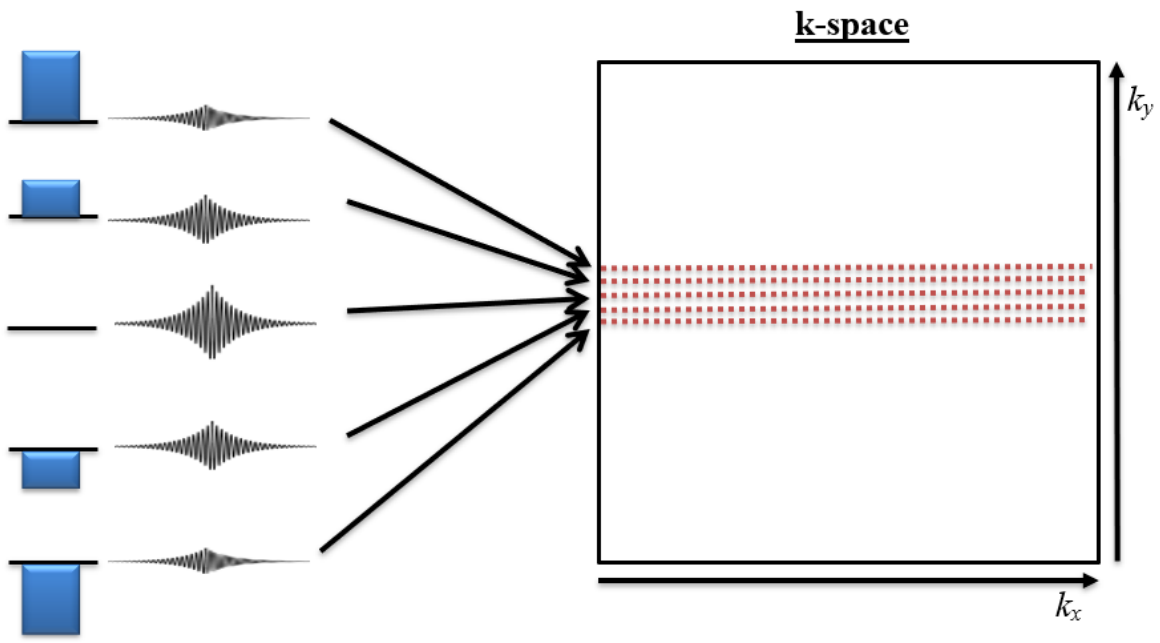

Figure 26: The MR signal from each phase encoding step is stored in a raw data matrix called k-space (with axes k_x and k_y). The phase encoding gradient (depicted by the rectangular blocks) determines which line of k-space is filled. In this schematic, five different phase encoding gradients are used, resulting in five sets of data along the k_y axis (depicted by the dotted lines).

3.1.5 Image Contrast and Weighting

The ability to generate contrast between different tissues types is one of the greatest advantages of MRI over other imaging modalities. The sources of contrast in MRI can emanate from nuclear spin relaxation times [100], spin density, chemical shift [101, 102], magnetic susceptibility [103, 104] and diffusion [105]. In MRI, it is also possible to experimentally further enhance the contrast of the image with respect to a particular factor,

such as longitudinal (i.e., T_1) and spin-spin (i.e., T_2) relaxation. This process is referred to as weighting. T_1 and T_2-weighting is of particular importance in enhancing contrast of different tissue types, as different types of soft tissue have different characteristic T_1 and T_2 relaxation times [98].

The two key parameters to adjust to enhance contrast with respect to relaxation are T_R and T_E. Considering a gradient-echo experiment, the contrast between two tissues, *A* and *B*, can be expressed as the difference in the signal of each tissue,

$$\begin{aligned} C_{AB} &= S_A - S_B \\ &= \rho^A \left(1 - e^{-T_R / T_1^A}\right) e^{-T_E / T_2^{*A}} - \rho^B \left(1 - e^{-T_R / T_1^B}\right) e^{-T_E / T_2^{*B}}, \end{aligned} \tag{3.7}$$

where C_{AB} is the contrast between the two tissues.

3.1.5.1 T_1-Weighted Images

To obtain effective T_1-weighting, T_2^* (i.e., effective T_2) effects need to be minimised. This can be achieved by reducing T_E, such that $T_E \ll T_2^{*A,B}$, thus reducing Eq. (3.7) to

$$C_{AB} = \rho^A \left(1 - e^{-T_R / T_1^A}\right) - \rho^B \left(1 - e^{-T_R / T_1^B}\right). \tag{3.8}$$

3.1.5.2 T_2-Weighted Images

Conversely, to obtain effective T_2-weighting, T_1 effects need to be minimised. This can be achieved by selecting a long T_R ($T_R \gg T_1$). The exponential associated with T_1 in Eq. (3.7) will then approach zero. Hence, (3.7) can be reduced to

$$C_{AB} = \rho^A e^{-T_E / T_2^{*A}} - \rho^B e^{-T_E / T_2^{*B}}. \tag{3.9}$$

As per the relationship in Eq. (3.9), optimal T_2 contrast can be obtained by maximising C_{AB} relative to T_E [106].

Chapter 4. MRI Contrast Agents

4.1 Introduction

In MRI, the relaxation rate of the water signal can be used as contrast to distinguish between different tissues. Such contrast can be enhanced using a contrast agent administered prior to scanning. These agents utilise paramagnetic metal ions and are evaluated on their ability to increase the relaxation rate of nearby water protons relative to their concentration. This evaluation is referred to as relaxivity. Whilst extensive research has looked into increasing the relaxivity of MRI contrast agents, very limited work has been undertaken to extend these properties to hypoxia-specific contrast agents (as mentioned in Chapter 1). Hence, the purpose of this chapter is to identify the most commonly used class of clinical contrast agents (i.e., positive contrast agents), and observe the different properties of the types of contrast agents in this class, thus determining the structure most favourable to be used in the development of the hypoxia-specific paramagnetic agents in this thesis.

4.2 Principles of MRI Contrast Agents

The concept of contrast enhancement in an MRI image was first demonstrated using manganese (II) salts in animal studies to achieve tissue discrimination [107]. Since then, Gd(III) (i.e., Gd^{3+}), due to its seven unpaired electrons resulting in the shortening of the relaxation time of water protons, has become the most widely used metal centre for the production of paramagnetic contrast agents. This has led to Gd-based agents now becoming the most commonly used agents in the clinic [65, 108].

While contrast agents containing Gd(III) increase both the longitudinal and transverse relaxation rates (i.e., $R_1 = 1/T_1$ and $R_2 = 1/T_2$, respectively), the relative change in R_1 is much greater than R_2 [109], hence such agents are predominantly visualised with T_1-weighted imaging [65]. The most commonly used contrast agents, as shown in Figure 27, utilise polyaminocarboxylate ligands. In these agents, the Gd(III) centre is coordinated with nitrogen and oxygen donor atoms. The complexes shown in Figure 27 act as nonspecific extracellular agents. Following intravascular injection, such compounds distribute rapidly amongst plasma and interstitial spaces, after which are eliminated through the renal route with half-lives of approximately 1.6 h [110, 111].

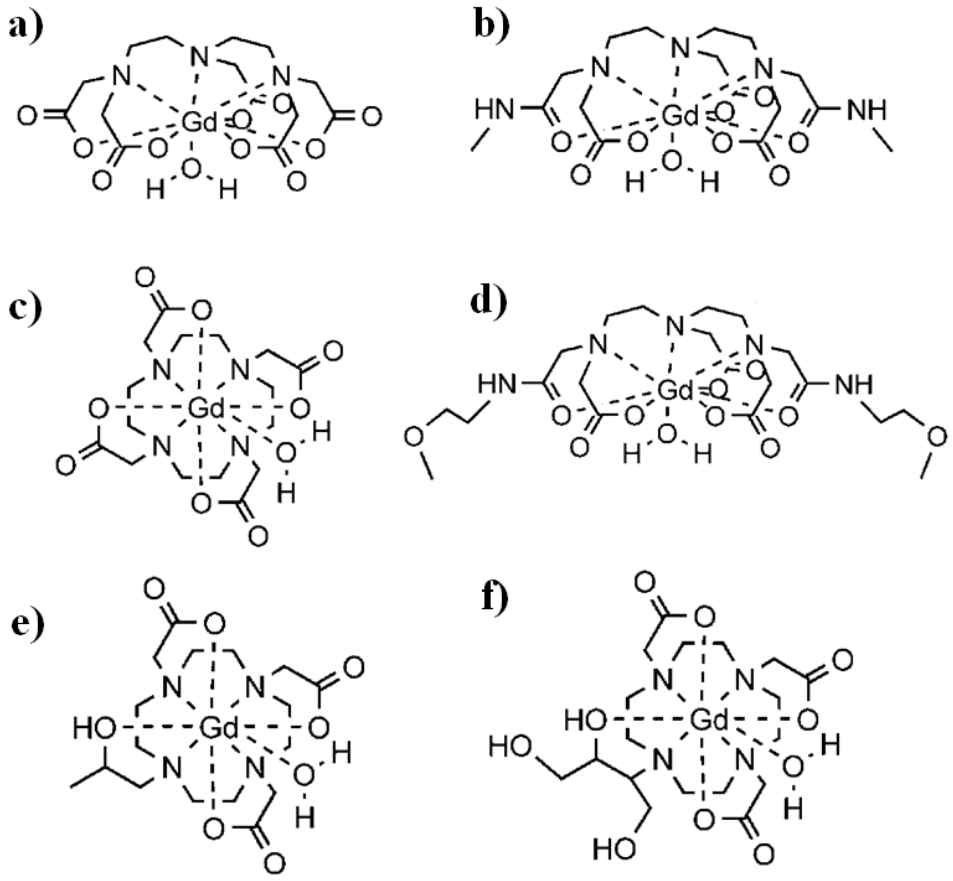

Figure 27: Structures of commonly used commercial MRI contrast agents: a) Magnevist® [Gd(DTPA)(H$_2$O)]$^{2-}$, b) Omniscan® [Gd(DTPA-BMA)(H$_2$O)], c) Dotarem® [Gd(DOTA)(H$_2$O)]$^-$, d) OptiMARK® [Gd(DTPA-BMEA)(H$_2$O)], e) ProHance® [Gd(HP-DO3A)(H$_2$O)], and f) Gadovist® [Gd(DO3A-butrol)(H$_2$O)] [112-114]. The above structures are classified as cyclic contrast agents, where the Gd ions are fully enclosed, in this case, by nitrogen and oxygen atoms. Alternatively, linear Gd contrast agents, where the Gd ions are not enclosed, are not discussed in the context of commercially available contrast agents in this thesis due to the recent suspension of such agents by the European Medicines Agency [115].

As mentioned previously in section 4.1, relaxivity (r_1 or r_2) is a measure of the efficiency of a contrast agent, and is defined as the change in the relaxation rate of the water protons normalised to its concentration, as given by

$$r_i = \frac{\Delta\left(1/T_i\right)}{[\mathrm{CA}]}, \tag{4.1}$$

where i = 1, 2 and [CA] is the concentration of the contrast agent. Relaxivity can be characterised with respect to T_1 or T_2 (i.e., r_1 or r_2, respectively) depending on whether the contrast agent is a positive (i.e., T_1) or negative (i.e., T_2) contrast agent. However, in practice, a simpler method to calculate r_1 and r_2 is to measure the T_1 and T_2, respectively of at least three dilutions of the contrast agent. In this way, the relaxivity is equal to the slope of $1/T_i$ versus [CA] (e.g. Figure 28), as can be seen by rearranging Eq. (4.2),

$$\frac{1}{T_i} = \frac{1}{T_{i,d}} + r_i[\mathrm{CA}], \tag{4.2}$$

where $T_{i,d}$ is the diamagnetic relaxation of the water protons (i.e., the relaxation of the solution without the contrast agent).

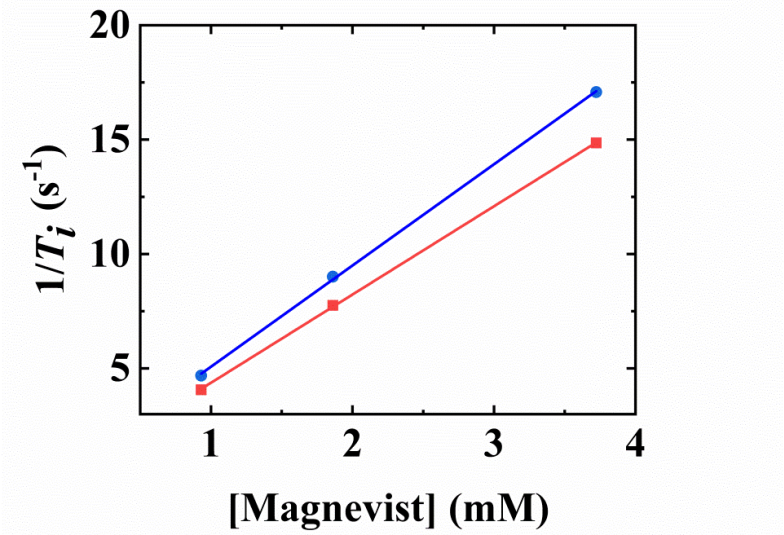

Figure 28: Experimental results showing the ^{1}H longitudinal (■) and transverse (●) relaxation rates for Magnevist plotted against concentration at 1 T (25 °C). From the slopes of the linear fits, r_1 and r_2 were determined to be 3.9 and 4.5 mM^{-1}s^{-1}, respectively.

4.3 Types of MRI Contrast Agents

As mentioned in the previous section, contrast agents can be classed as negative or positive contrast agents. Negative contrast agents usually have an r_2/r_1 as high as 10 or more [65]. This means that such agents reduce T_2 a lot more than T_1. Negative contrast agents are predominantly made from superparamagnetic iron oxide (SPIO) and induce negative contrast in an MR image by decreasing the signal intensity of the affected water protons [116, 117]. SPIO MR contrast agents are effectively used to visualise and detect lesions in the liver, as

SPIO particles are sequestered by phagocytic Kupffer cells in the normal reticuloendothelial system but not retained in lesions, which lack Kupffer cells [118].

Positive contrast agents usually have an r_2/r_1 of approximately 1-2, comprising of paramagnetic metal ions chelated to multi-dentate ligands. These types of contrast agents induce a positive contrast by increasing the signal intensity of the surrounding water protons. The images produced by such agents exhibit hyper-intense regions via contrast agent accumulation, and thus are more commonly used in the clinics [119, 120]. For this reason, the following discussions deal with types of positive contrast agents.

Positive contrast agents can be sub-divided into two categories based on their molecular weight: low and high molecular weight contrast agents, and these will be discussed below. As high molecular weight contrast agents are favourable for high relaxivities relative to low molecular weight contrast agents, such agents will then be discussed in terms of macromolecular and supramolecular contrast agents. By observing the properties of supramolecular contrast agents, in particular liposomes, it will be discussed why this type of contrast agent was chosen as the structure of choice for the synthesis of the hypoxia-specific paramagnetic agents in this thesis.

4.3.1 Low Molecular Weight Contrast Agents

Structurally, Gd-based contrast agents can be categorised as linear or macrocyclic agents based on the type of ligand. The ligands of linear agents are elongated and wrap around the Gd ion, while macrocyclic agents form a cage-like ligand structure, trapping the ion in a central cavity. Most of the current commercially available contrast agents take the form of either the linear-diethylenetriaminepentaacetic acid (DTPA) or cyclic-tetraazacyclododecane-N,N,N,N-tetraacetic acid (DOTA) complexes of Gd(III). These contrast agents can be broadly classified as low molecular weight contrast agents (e.g., molecular weight ≈ 600 [121]). However, the use of such contrast agents has also been linked with nephrogenic systemic fibrosis, especially in patients with acute renal failure [122, 123]. It is suspected that the Gd-ligand complex dissociates due to the prolonged clearance as a result of renal failure. This further emphasises the need for more stable contrast agents [122]. Whilst low molecular contrast agents have been used clinically, the use of high molecular weight contrast agents (e.g., Gadomer: molecular weight ≈ 40,000 [121]) are more favourable in obtaining higher relaxivities. This will be discussed in the following section, and such contrast agents are the focus of this chapter.

4.3.2 High Molecular Weight Contrast Agents

The relaxivity of a contrast agent is affected by the reorientational correlation time (τ_R), mean water residency time (τ_m), electronic relaxation times (T_{ie} where i = 1,2) and hydration number (q). Increasing the molecular weight of a contrast agent slows down the molecular reorientation of the contrast agent, resulting in a longer τ_R and thus, a higher relaxivity. Hence, such contrast agents are desired in the clinics as it enables for better contrast at low doses [124]. High molecular weight contrast agents take the form of macromolecular or supramolecular contrast agents, and will be discussed in the following sections.

4.3.2.1 Macromolecular Contrast Agents

Macromolecular contrast agents are formed by the conjugation of chelates onto macromolecular carriers. This involves attaching low molecular weight Gd chelates to large molecules such as proteins or polymers. The chelates can also be incorporated within dendrimers, zeolites, fullerenes and nanotubes to form macromolecular contrast agents. Irrespective of the method, the molecular reorientation of the contrast agent is reduced (i.e., restricted by the larger molecule), thus resulting in higher relaxivities.

Macromolecular contrast agents can be classified as block, graft, dendritic or micellar macromolecular contrast agents according to the position of the Gd(III) chelates in the carriers [125]. In block agents, the condensation polymerisation of DTPA dianhydride with diol or diamine monomers is used to incorporate Gd chelates into the polymer [125]. In graft and dendritic agents, the reaction of bifunctional contrast agents with reactive groups on the polymer is used to conjugate the Gd chelates, while emulsion polymerisation is used to produce micellar agents [125]. Irrespective of the structure, macromolecular contrast agents deliver smaller payloads of Gd(III) ions than supramolecular agents. Hence, supramolecular contrast agents are favoured for use in MRI, and are the focus of this thesis, and are discussed below.

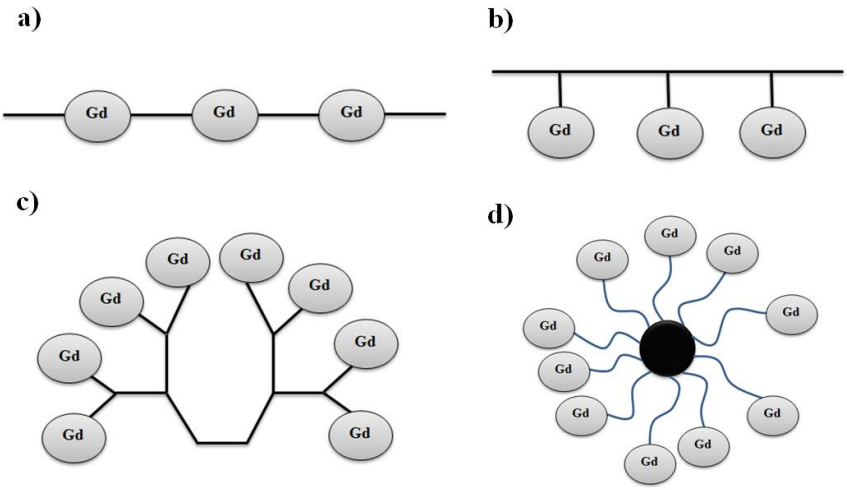

Figure 29: Schematic structures of the four classes of macromolecular contrast agents: a) block, b) graft, c) dendritic and d) micellar (with the structure depicted by the black circle representing an aggregate of surfactant molecules dispersed in a liquid colloid).

4.3.2.2 Supramolecular Contrast Agents

Supramolecular aggregates, such as micelles and liposomes, are obtained by spontaneous assembling of amphiphilic molecules in aqueous solution. These amphiphilic molecules consist of a hydrophobic and a hydrophilic moiety. In water, the hydrophobic associative interactions of the tails and the repulsive interactions between the hydrophobic head groups self-assemble these amphiphilic molecules into well-defined structures [126]. A wide variety of factors can be varied when designing the hydrophobic and hydrophilic moieties of amphiphilic molecules. The hydrophobic moiety can be varied in length, containing multiple chains. This thereby alters the size of the hydrophobic component, hence changing the ratio (with respect to size) between the hydrophobic and hydrophilic components. Furthermore, the hydrophilic head-group can be varied in size and charge, thus altering the molecules between ionic and non-ionic amphiphiles.

The type of supramolecular aggregates that form in solution can be predicted based on the steric relationship of the head-group and the side arm [127],

$$SP = \frac{v}{al}, \tag{4.3}$$

where SP is the surfactant parameter, v and l are the volume and length, respectively, of the hydrophobic chains, and a is the surface area of the hydrophilic head-group. Amphiphiles

with $SP \approx 1$ are likely to yield flat structures (e.g., vesicles or planar lamellar) due to the balance in sizes between the head and tail groups [128]. Amphiphiles with $SP < 1$ are likely to form structures curved towards the hydrocarbon chain (e.g., cubic phases), while amphiphiles with $SP > 1$ are likely to form structures curved towards water (e.g., inverse hexagonal structures [129]) [128]. These characteristics, along with other parameters such as pH, concentration, temperature and ionic strength, determine whether micelle-like structures, such as cylindrical, spherical or ellipsoidal micelles or bilayer-like structures, such as vesicles or liposomes, are formed [120].

Micellar aggregates are characterised by their unique core shell structure. In an aqueous solution, the inner core is formed by the segregation of the hydrophobic component of the amphiphilic molecules from the aqueous exterior. The hydrophilic components form the outer shell. The formation of micelles is driven by a decrease of free energy within the system. This results from the re-establishing of the hydrogen bond network in water following the removal of hydrophobic fragments from the aqueous solution. In addition, the formation of micelles results in Van der Waals interactions between hydrophobic moieties in the core [120, 130]. Micelles usually range in size from 5 to 50 nm [120].

Conversely, liposomes are self-enclosed artificial phospholipids vesicles, varying in size from 25 to 1000 nm [131]. Liposomes can be classified as unilamellar (i.e., one lipid bilayer) or multilamellar (i.e., multiple lipid bilayers), as shown in Figure 30. The preparation of liposomes usually involve the addition of cholesterol, which is used to stabilise the lipid bilayer. The addition of cholesterol also influences the water permeability of the liposome membrane [132]. However, water permeability is predominantly affected by the length of the phospholipid alkyl chain and the unsaturation of the hydrocarbon chain [120].

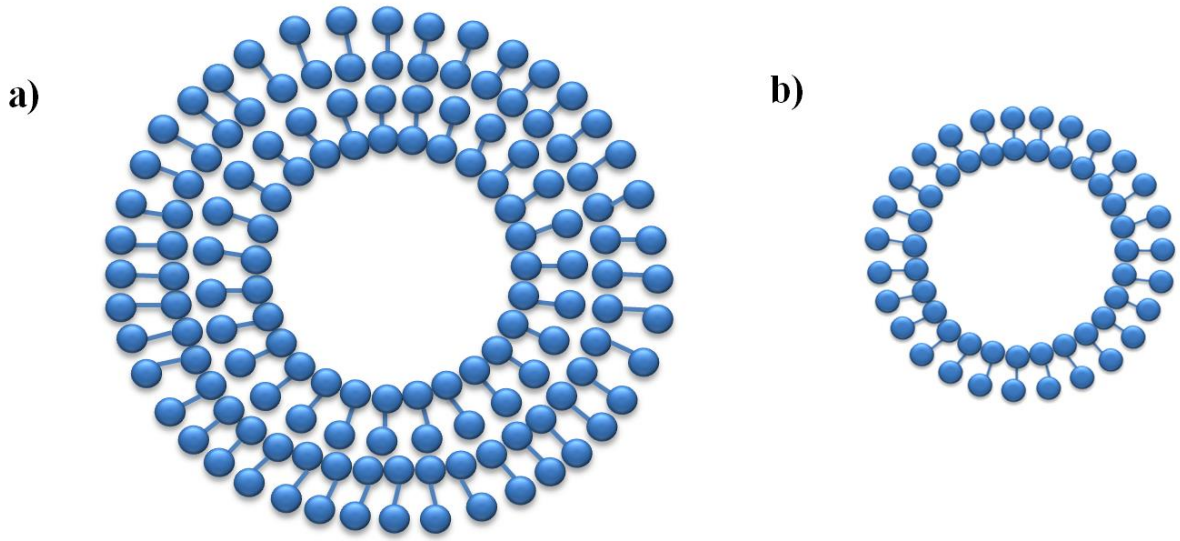

Figure 30: Liposomes can be classified depending on the number of lipid bilayers: a) multilamellar or b) unilamellar liposomes. Unilamellar liposomes range from approximately 25 – 200 nm (diameter) in size, whilst multilamellar liposomes can be up to 1000 nm [131].

The biodistribution of micelles and liposomes are controlled by easily altered physicochemical properties such as membrane composition, size or surface charge [120, 133-135]. This allows for the attainment of favourable pharmacological characteristics, thus making supramolecular aggregates excellent candidates as possible carriers for MRI contrast agents. Attaching a Gd-based contrast agent to a supramolecular aggregate would allow to enhance contrast efficacy and change the pharmacokinetic properties of the contrast agent. Studies dating back to the 1980s [136-138] have used two main approaches in the development of liposomal contrast agents. One approach is to entrap the contrast agent within the central region of the liposome [136], while the other incorporating the contrast agent in the lipid bilayer of the liposome [137, 138] (Figure 31).

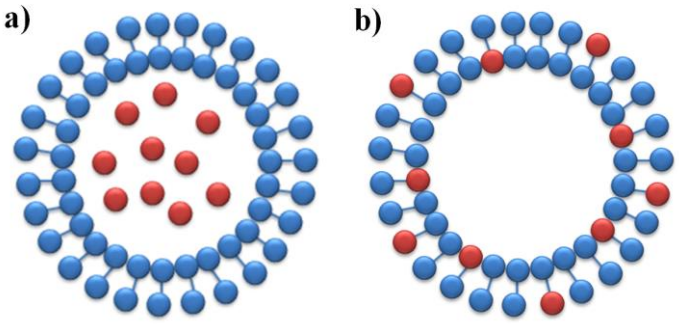

Figure 31: Two main approaches in the development of liposomal contrast agents: a) the contrast agent (red) is trapped within the central region of the liposome, and b) the contrast agent is incorporated into the lipid bilayer of the liposome.

Studies entrapping the contrast agent within the centre of the liposome have shown a low relaxivity, of approximately two to five times lower compared to free Gd complexes [139]. This is believed to be due to the limited exchange of bulk water with the contrast agent, resulting from the low water permeability of the liposomal membrane [136, 140, 141]. On the contrary, incorporating the contrast agent in the lipid bilayer and localising it on the liposome surface, increases the relaxivity of the contrast agent relative to both encapsulation method complexes and low molecular weight complexes [142], hence presents an ideal design to be used in the development of new contrast agents.

The Nuclear Magnetic Relaxation Dispersion (NMRD) profile of supramolecular contrast agents typically show a peak at higher frequencies, indicating an increase in reorientational correlation times relative to low molecular weight contrast agents. More importantly, these peaks occur at clinical relevant magnetic field strengths (≈1 T), meaning that the highest relaxivities will be able to be utilised in the clinic. The use of supramolecular contrast agents further enhances the total relaxivity per contrast agent particle as the ratio of Gd(III) complexes per supramolecular particle is in the order of 50:1 for small micelles and upwards of several thousand for liposomes [120].

As mentioned previously, low water permeability of the liposomal membrane results in low relaxivities. This can be increased by using smaller liposomes, thus improving the exchange with external bulk water. The reduction in relaxivity in larger liposomes is most likely due to the reduced surface area to volume ratio and the presence of multilamellar bilayers, which slow water exchange between the interior and the exterior of the liposome

[136, 140]. Hence, small, unilamellar liposomes with a permeable bilayer would be an optimal formulation for the purpose of increased relaxivities. However, careful consideration needs to be made with such formulations as permeable liposomes tend to be less stable than those with more rigid bilayers.

Furthermore, liposomes can be surface functionalised with targeting ligands to enhance tumor selective targeting. Despite the demonstration of clinically useful anti-tumor activity with passively targeting liposomes [143, 144], further specificity for the tumor cell can be achieved via ligand-mediated targeting (more commonly referred to as active targeting). Use of such ligand-mediated targeting in drug delivery has yielded significantly increased drug delivered to target cells compared to when free drugs or passive targeting was used. Such a concept can be extended to the development of contrast agents which target tissue hypoxia.

Hence, for the reasons discussed above, in particular, the biocompatibility, synthesis simplicity, high relaxivity properties and targeting capabilities, supramolecular aggregates in the form of liposomes will be the structure of choice used in the development of the hypoxia-specific paramagnetic agents in this thesis, as will be detailed in Chapter 7.

Chapter 5. A Complete Derivation of the Kärger Equations

This chapter contains verbatim passages from:

Dj Wijesekera, Timothy Stait-Gardner, Abhishek Gupta, Johnny Chen, Gang Zheng, Allan M. Torres, William S. Price, A Complete Derivation of the Kärger Equations for Analysing NMR Diffusion Measurements of Exchanging Systems, *Concepts in Magnetic Resonance Part A*, 2018 *(in press)*.

5.1 Introduction

Being able to characterise binding and exchange is fundamental to understanding chemical reactions. For example, the biological activity of drugs at the molecular level corresponds to the binding of small molecules to macromolecular receptors, such as protein-ligand interactions, and lies at the heart of pharmacology [145]. NMR spectroscopy is widely used to study binding and exchange in chemical and biological systems due to its general applicability and non-invasive nature [146-149]. A range of NMR techniques have been used to study exchange in a diverse range of systems, with a particular emphasis on solution-state NMR to probe protein-ligand interactions [149, 150]. All NMR techniques rely on some NMR observable that is sensitive to exchange such as chemical shift, relaxation (including nuclear Overhauser effects), saturation transfer or diffusion.

This chapter focusses on the use of diffusion measurements to study (intermolecular) exchange. The mathematical framework for analysing such data is provided by the Kärger equations [151-153]. In fact, the Kärger model and adaptations have found wide application to chemical and biological systems including brain imaging [154-156]. Here, a detailed derivation of these equations for the case of two freely diffusing exchanging species is presented along with the simplifications that result in the slow and fast exchange limits. Considerable emphasis is given to the physical interpretation and limitations of these equations. With the intention of studying ligand binding using NMR diffusion measurements in the following chapter of this thesis, some consideration is given to the analysis of protein-ligand binding using diffusion NMR. Finally, the extension of the Kärger equations to cover a three-state model is briefly considered. First, however, it is considered how the Bloch equations, exchange equations and diffusion equation can be combined in various ways to describe these phenomena.

5.2 The Bloch Equations, Chemical Exchange and Diffusion

Here introduced in turn are: (1) the Bloch equations describing the evolution of the nuclear magnetisation in the presence of a magnetic field, magnetic gradients and rf pulses; (2) the equations governing chemical exchange in situations involving conformational changes or intermolecular binding; and (3) the diffusion equation in the differential form. Each of these equations is then reduced to a simpler form in terms of the complex magnetisation $M(z,t) = M_x(z,t) + iM_y(z,t)$, which is more suitable for the development of the theory later in

the chapter. These three equations will be combined together in various ways in later sections.

5.2.1 The Bloch Equations

The evolution of nuclear magnetisation for an uncoupled population of spin-half nuclei can be described by the Bloch equations [157, 158],

$$\begin{aligned}
\frac{dM_x(\mathbf{r},t)}{dt} &= \gamma\left(\mathbf{M}(\mathbf{r},t)\times\mathbf{B}(\mathbf{r},t)\right)_x - \frac{M_x(\mathbf{r},t)}{T_2},\\
\frac{dM_y(\mathbf{r},t)}{dt} &= \gamma\left(\mathbf{M}(\mathbf{r},t)\times\mathbf{B}(\mathbf{r},t)\right)_y - \frac{M_y(\mathbf{r},t)}{T_2},\\
\frac{dM_z(\mathbf{r},t)}{dt} &= \gamma\left(\mathbf{M}(\mathbf{r},t)\times\mathbf{B}(\mathbf{r},t)\right)_z - \frac{M_z(\mathbf{r},t)-M_0}{T_1},
\end{aligned} \tag{5.1}$$

where $\mathbf{M}(\mathbf{r},t) = M_x(\mathbf{r},t)\mathbf{i} + M_y(\mathbf{r},t)\mathbf{j} + M_z(\mathbf{r},t)\mathbf{k}$ is the macroscopic magnetisation density of the population; $\mathbf{B}(t)$ is the magnetic field – typically this is of the form $\mathbf{B}(\mathbf{r},t) = (B_0 + \mathbf{G}(t)\cdot\mathbf{r})\mathbf{k} + B_{rf}\cos(\omega_{rf}t + \phi)\mathbf{i}$ where B_0 is the strength of the main magnetic field and, if a gradient is present, its magnitude and direction are given by $\mathbf{G}(t)$ ($\mathbf{r}$ denotes the position of the nuclear population); B_{rf} is the magnitude of the rf pulse (and is significantly smaller than B_0), ω_{rf} is its frequency and ϕ is its phase. The effects of the rf pulse do not need to be considered here and this term will be ignored from now on. It can also be assumed the gradient is along the longitudinal direction and to be of the form $\mathbf{G}(t) = gf(t)\mathbf{k}$, where g is the strength of the magnetic gradient and $f(t)$ is a temporal shape function (having a maximum value of one). In this case, $\mathbf{B}(\mathbf{r},t)$ only has a component in the longitudinal ($\mathbf{k}$) direction and the Bloch equations simplify to,

$$\begin{aligned}
\frac{dM_x(\mathbf{r},t)}{dt} &= \gamma\left(B_0 + gf(t)z\right)M_y(\mathbf{r},t) - \frac{M_x(\mathbf{r},t)}{T_2},\\
\frac{dM_y(\mathbf{r},t)}{dt} &= -\gamma\left(B_0 + gf(t)z\right)M_x(\mathbf{r},t) - \frac{M_y(\mathbf{r},t)}{T_2},\\
\frac{dM_z(\mathbf{r},t)}{dt} &= -\frac{M_z(\mathbf{r},t)-M_0}{T_1}.
\end{aligned} \tag{5.2}$$

This is a set of coupled differential equations – but only the transverse components $M_x(\mathbf{r},t)$ and $M_y(\mathbf{r},t)$ are coupled together. Thus, if the interest is only in the evolution of the transverse magnetisation under delays and gradients (and also under 180° pulses), the transverse components of Eqs. (5.2) can be written in complex form by defining $M(\mathbf{r},t) = M_x(\mathbf{r},t) + iM_y(\mathbf{r},t)$ and noting,

$$\frac{dM(z,t)}{dt} = i\omega_0 M(z,t) - i\gamma g f(t) z M(z,t) - \frac{M(z,t)}{T_2}, \tag{5.3}$$

where $\omega_0 = -\gamma B_0$ (i.e., the Larmor frequency) and the x and y directions have been eliminated since it can be assumed M is only a function of z and t. By making the replacement $M \rightarrow M\exp(i\omega_{rf}t)$, Eq. (5.3) becomes,

$$\frac{dM(z,t)}{dt} = i(\omega_0 - \omega_{rf})M(z,t) - i\gamma g f(t) z M(z,t) - \frac{M(z,t)}{T_2}, \tag{5.4}$$

where ω_{rf} is the precession frequency of the rotating reference frame (this can be any frequency selected). When radiofrequency pulses are involved it's convenient to set ω_{rf} equal to the frequency of the rf pulse (the subscript rf can then be interpreted either as **r**otating **f**rame or **r**adio**f**requency). For the purposes of this chapter, it is convenient to choose ω_{rf} as ω_0, which eliminates the first term on the right-hand-side from Eq. (5.4). The last term can also be eliminated by making the replacement $M \rightarrow M\exp(-t/T_2)$ yielding,

$$\frac{dM(z,t)}{dt} = -igf(t)M(z,t). \tag{5.5}$$

5.2.2 Chemical Exchange

Chemical exchange, in the NMR context, refers to any process where a nucleus exchanges between two or more environments in which its NMR parameters differ. Chemical exchange can be categorised as intramolecular exchange, where a molecule undergoes a conformational change, or intermolecular exchange, where the molecule binds to another molecule, such as a protein (see Figure 32).

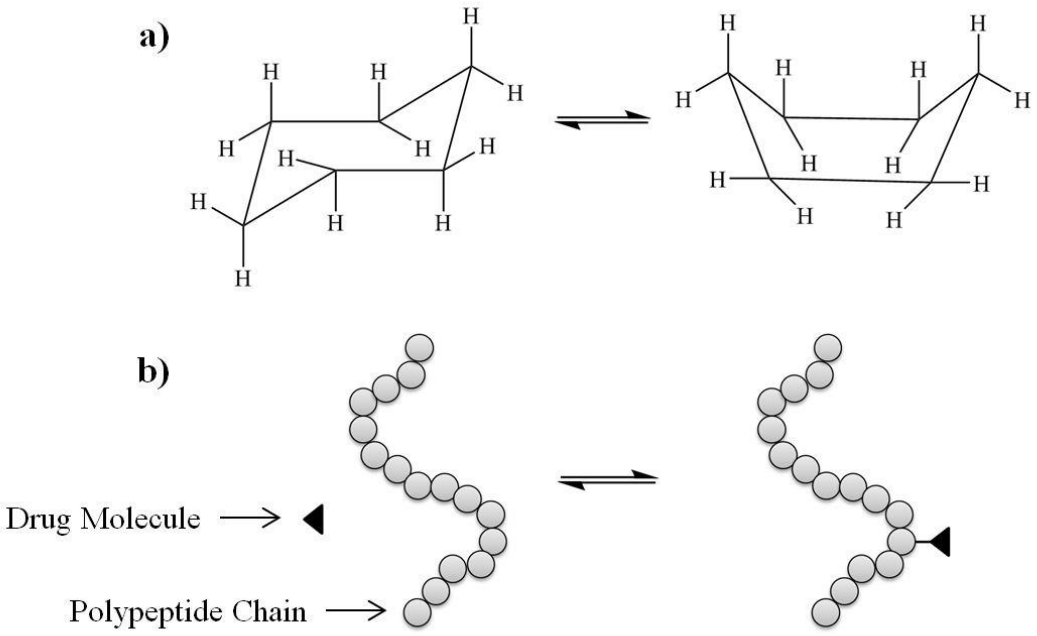

Figure 32: Two types of chemical exchange: (a) intramolecular exchange, showing a conformational change of the molecule cyclohexane, and (b) intermolecular exchange, showing the binding of one molecule to another. Diffusion NMR is particularly applicable to studying intermolecular exchange.

Consider an exchanging chemical system,

$$\mathrm{A} \underset{k_B}{\overset{k_A}{\rightleftharpoons}} \mathrm{B}, \tag{5.6}$$

where A and B represent different conformations or binding states of the same molecule with rate constants k_A and k_B. The quantities of molecules in forms A and B, denoted [A] and [B], respectively, and measured in moles are given by,

$$\begin{aligned}\frac{d[A]}{dt} &= -k_A[A] + k_B[B],\\ \frac{d[B]}{dt} &= k_A[A] - k_B[B].\end{aligned} \tag{5.7}$$

However, this system needs to be viewed from the NMR observable perspective, where both A and B contain NMR observable nuclei (e.g., ^{1}H) and assume that some subset of these are labelled (i.e. have, on average, a spin aligned along some direction denoted by a unit vector $\hat{\mathbf{M}}$). Now [A] and [B] denote the number of moles per unit volume of these labelled nuclei. Then the macroscopic magnetisation densities corresponding to the NMR active nucleus are proportional to [A] and [B], respectively, and aligned along $\hat{\mathbf{M}}$, giving,

$$\begin{aligned}\frac{d\mathbf{M}_A(\mathbf{r},t)}{dt} &= -k_A\mathbf{M}_A(\mathbf{r},t) + k_B\mathbf{M}_B(\mathbf{r},t),\\ \frac{d\mathbf{M}_B(\mathbf{r},t)}{dt} &= k_A\mathbf{M}_A(\mathbf{r},t) - k_B\mathbf{M}_B(\mathbf{r},t),\end{aligned} \tag{5.8}$$

where $\mathbf{M}_A$ and $\mathbf{M}_B$ are the magnetisation densities corresponding to states A and B, respectively. Furthermore, at equilibrium (i.e., when $\mathbf{M}_A(\mathbf{r},t) = \mathrm{M}_{0A}\mathbf{k}$ and $\mathbf{M}_B(\mathbf{r},t) = \mathrm{M}_{0B}\mathbf{k}$) the time derivatives in Eq. (5.8) are zero, giving,

$$k_A M_{0A} = k_B M_{0B}\,. \tag{5.9}$$

The fractional populations in pools A and B at equilibrium are denoted by P_A and P_B, respectively. Since these are fractional populations,

$$P_A + P_B = 1. \tag{5.10}$$

Also, since P_A and P_B are proportional to M_{0A} and M_{0B}, respectively, with the same constant of proportionally, Eq. (5.9) gives (the principle of detailed balance),

$$k_A P_A = k_B P_B. \tag{5.11}$$

If the interest is only in the transverse magnetisation and the magnetisation is considered to be independent of x and y, $M(z,t)=M_x(z,t) + iM_y(z,t)$ can be set, giving,

$$\begin{aligned} \frac{dM_A(z,t)}{dt} &= -k_A M_A(z,t) + k_B M_B(z,t), \\ \frac{dM_B(z,t)}{dt} &= k_A M_A(z,t) - k_B M_B(z,t). \end{aligned} \tag{5.12}$$

The rate constants k_A and k_B are related to the average lifetimes τ_A and τ_B of the two sites by $k_A = \tau_A^{-1}$ and $k_B = \tau_B^{-1}$. Eq. (5.12) can therefore be written more simply as,

$$\begin{aligned} \frac{dM_A}{dt} &= -\frac{M_A}{\tau_A} + \frac{M_B}{\tau_B}, \\ \frac{dM_B}{dt} &= \frac{M_A}{\tau_A} - \frac{M_B}{\tau_B}. \end{aligned} \tag{5.13}$$

and Eq. (5.11) as,

$$\frac{P_A}{\tau_A} = \frac{P_B}{\tau_B}. \tag{5.14}$$

5.2.3 Diffusion

In the context of this chapter, it will be useful to model diffusion using the diffusion equation (Fick's second law; which is mathematically equivalent to the equation for heat conduction) (e.g., refs.[159-161]),

$$\frac{\partial \vartheta(\mathbf{r},t)}{\partial t} = D\nabla^2 \vartheta(\mathbf{r},t), \tag{5.15}$$

where ϑ is the concentration. In addition to describing mutual diffusion – that is diffusion in the presence of a chemical potential gradient, e.g. the diffusion of some substance A within another substance B where $\vartheta(\mathbf{r},t)$ represents the concentration of A in B at position **r** and time *t* – Eq. (5.15) can also be used to describe self-diffusion, where the chemical potential gradient equals zero. For the measurement of self-diffusion $\vartheta(\mathbf{r},t)$ can represent the concentration of some non-invasive label at position **r** and time *t*. This label in NMR is the nuclear spin state represented by the magnetisation density **M**, giving,

$$\frac{\partial \mathbf{M}(\mathbf{r},t)}{\partial t} = D\nabla^2 \mathbf{M}(\mathbf{r},t). \tag{5.16}$$

If the magnetisation is initially independent of *x* and *y*, then it will remain so and **M** can be considered to be a function of only *z* and *t*. Eq. (5.16) then becomes,

$$\frac{\partial \mathbf{M}(z,t)}{\partial t} = D\frac{\partial^2 \mathbf{M}(z,t)}{\partial z^2}. \tag{5.17}$$

Furthermore, if only the transverse magnetisation is of interest (which is often the case), then the equations for M_x and M_y can be combined into one equation,

$$\frac{\partial M(z,t)}{\partial t} = D\frac{\partial^2 M(z,t)}{\partial z^2}, \tag{5.18}$$

where $M(z,t) = M_x(z,t) + iM_y(z,t)$.

5.3 Probing Binding and Exchange Using Diffusion NMR

5.3.1 Diffusion and its Measurement

D is an NMR observable that can be used to probe binding and exchange. As discussed in Chapter 2, a diffusion coefficient can be physically interpreted through the Stokes-Einstein-Sutherland equation, which in essence states that the larger molecules diffuse more slowly than the smaller molecules. Hence, if a species is exchanging and becoming larger (e.g., self-association) or effectively larger (e.g., a ligand binding to a protein) then this will be reflected in the measured diffusion coefficient. The effects of exchange also affect the measured diffusion coefficient as will be illustrated below.

There are many NMR sequences that can be used to measure diffusion [76]. Here, the PGSE method which is the progenitor of most of the other sequences is considered. Combining the Bloch equations (Eq. (5.5)) with the diffusion equation (Eq. (5.18)) provides an equation that describes how the magnetisation evolves in the presence of a gradient while diffusion is occurring. The combination is straightforward: the time derivative of the transverse magnetisation is simply given by the right-hand-side of Eq. (5.5) added to the right-hand-side of Eq. (5.18), viz. [162],

$$\frac{dM(z,t)}{dt} = -igf(t)M(z,t) + D\frac{\partial^2 M(z,t)}{\partial z^2}. \tag{5.19}$$

These equations are known as the Torrey-Bloch equations and can be used to compute the signal attenuation resulting from diffusion occurring during the sequence.

In brief, NMR diffusion measurements are conducted in using a spin-echo or stimulated echo pulse sequence modified to include a pair of magnetic pulsed field gradients of duration δ and amplitude g separated by a delay Δ. The first gradient pulse winds the spin magnetisation into a helix and the second gradient pulse unwinds the helix. The pitch of the helix is given by q^{-1} (m) where q is defined by

$$\mathbf{q} = \frac{\gamma\delta\mathbf{g}}{2\pi} \text{ (m}^{-1}\text{).} \tag{5.20}$$

Recall that the magnetic gradient is a vector quantity and that **g** (or equivalently **q**) defines the direction in which diffusion is measured (some nice illustrations of this are given in ref.[163]). In an isotropic system such as the one considered here, the same result will be obtained irrespective of the direction of the gradient. However, were the system to be anisotropic this would not be the case.

Diffusion occurring between (and during) the gradient pulses causes the magnetisation helix to attenuate so that after the second gradient pulse the unwound magnetisation is of a reduced magnitude than would have been the case had there been no diffusion. This results in acquisition of a smaller signal S. The degree of attenuation depends on D, g, Δ and δ. The spin-echo signal for a freely diffusing species is given by [76, 90, 164],

$$S = M_0 \exp\left(-(\gamma\delta g)^2 D\left(\Delta - \frac{\delta}{3}\right)\right)\exp\left(-\frac{2\tau}{T_2}\right), \tag{5.21}$$

(which, as stated previously, can be computed from the Torrey-Bloch equations) where M_0 is the initial magnetisation. The $\delta/3$ term is the correction factor for diffusive attenuation that occurs during the gradient pulses (i.e. during the winding and unwinding of the magnetisation helix). Eq. (2.8) is typically normalised to the signal acquired without an applied gradient

($S_{g=0}$) to remove the attenuation of the spin-spin relaxation, giving the attenuation of the echo signal, *E*,

$$E = \frac{S}{S_{g=0}} = \exp\left(-(\gamma\delta g)^2 D\left(\Delta - \frac{\delta}{3}\right)\right). \tag{5.22}$$

Analysis for the stimulated echo based pulse sequence is very similar except that Eq. (2.8) must be modified to also include the effects of spin-lattice relaxation during the delay τ_2 where the magnetisation is longitudinal. However, normalising the signal to get the attenuation *E* in the same manner as used for the PGSE sequence results in exactly the same attenuation expression as PGSE (Eq. (2.9)). Experimentally, the molecular self-diffusion coefficient can be measured by conducting a series of measurements with different *g* values. *D* can then be determined using non-linear regression of Eq. (2.9) onto the echo attenuation data (i.e., *E* versus *g*. Δ defines the timescale of the diffusion measurement.

In the short gradient pulse (SGP) approximation in which it is assumed that the gradient pulses are infinitely short (but $g\delta$ is finite), the expression for the signal and attenuation take the simpler forms

$$S = M_0 \exp\left(-(2\pi q)^2 D\Delta\right)\exp\left(-\frac{2\tau}{T_2}\right) \tag{5.23}$$

and

$$E = \exp\left(-(2\pi q)^2 D\Delta\right). \tag{5.24}$$

Experimentally it is normally impossible to even closely approximate the requirements for the SGP condition. However, the analysis of the echo attenuation is greatly simplified in the SGP condition since the effects of diffusion during the gradient pulse (i.e., during the δ periods) can be neglected. This is why Eqs. (5.23) and (5.24) lack the δ/3 term found in Eqs. (2.8) and (2.9) that corrects the attenuation for the effects of diffusion during δ . Note, however, that the correction for diffusion during the gradient pulses is extremely difficult to

compute analytically for anything more complicated than straight free diffusion of a single non-exchanging species (e.g., see ref.[165]).

Now consider a system in which a molecule is undergoing exchange, where it is assumed that binding is between free and bound states. If the exchange is slow on the timescale of Δ (i.e., $\Delta << \tau_A, \tau_B$), then during the diffusion measurement timescale Δ it will appear as though there are two species present, the free species and the bound species. Then the signal intensity should be the signal from the free species added to the signal from the bound species, viz.,

$$S = P_b \exp\left(-(2\pi q)^2 D_b \Delta\right) + P_f \exp\left(-(2\pi q)^2 D_f \Delta\right), \tag{5.25}$$

where P_b and P_f are the populations of the bound and free species, respectively, and D_b and D_f are their respective diffusion coefficients. The effects of spin relaxation during the PGSE sequence have been ignored.

Now assume that the exchange is fast – so during the diffusion measurement period Δ there are many exchanges back and forth between the free and bound states (i.e., $\Delta >> \tau_A, \tau_B$). Thus, it appears that there is one diffusing species with a population-weighted diffusion coefficient,

$$D = P_f D_f + P_b D_b . \tag{5.26}$$

What is not so clear is what diffusion measurements should yield in the case of intermediate exchange between the fast and slow limits, and even under what conditions the fast and slow limits can be said to hold. To answer these questions, the Kärger equations must be developed [151-153].

5.3.2 The Two-Site Kärger Model for Two Freely Diffusing Species

The two-site Kärger model describes the signal intensity following a PGSE experiment for a diffusing species that can exist in both a free and a bound state. To make the analysis more mathematically tractable the equations are developed within the SGP approximation (see Section 5.3.1) although efforts have been made to extend their validity beyond the SGP approximation [166]. Thus, diffusion and exchange are ignored during the gradient pulses and the model becomes an analysis of the signal attenuation occurring during the Δ period where the magnetisation is in the form of a helix. The Kärger model can be derived by combining the Bloch equations (Eq. (5.4)), with the equations governing chemical exchange (Eqs. (5.13)) and with the diffusion equation (Eq. (5.18)). To recap: the diffusion equations are,

$$\begin{aligned} \frac{\partial M_f(z,t)}{\partial t} &= D_f\left(\frac{\partial^2 M_f(z,t)}{\partial z^2}\right), \\ \frac{\partial M_b(z,t)}{\partial t} &= D_b\left(\frac{\partial^2 M_b(z,t)}{\partial z^2}\right); \end{aligned} \quad , \tag{5.27}$$

the exchange equations are,

$$\begin{aligned} \frac{dM_f(z,t)}{dt} &= -\frac{M_f(z,t)}{\tau_f} + \frac{M_b(z,t)}{\tau_b}, \\ \frac{dM_b(z,t)}{dt} &= -\frac{M_b(z,t)}{\tau_b} + \frac{M_f(z,t)}{\tau_f}; \end{aligned} \tag{5.28}$$

and the Bloch equations (in the form useful here are),

$$\frac{dM_f(z,t)}{dt} = i\left(\omega_{0f} - \omega_{rf}\right)M_f(z,t) - \frac{M_f(z,t)}{T_{2f}},$$
$$\frac{dM_b(z,t)}{dt} = i\left(\omega_{0b} - \omega_{rf}\right)M_b(z,t) - \frac{M_b(z,t)}{T_{2b}}. \tag{5.29}$$

M represents the complex-valued transverse nuclear magnetisation (with M_f being the component belonging to the free state and M_b belonging to the bound state); D_f and D_b are the diffusion coefficients for the free and bound states, respectively; τ_f and τ_b represent the lifetimes in the free and bound states, respectively; ω_{0f} and ω_{0b} are the Larmor frequencies of the resonance of interest for the free and bound states of the molecule; and T_{2f} and T_{2b} are the relaxation times of the resonance of interest for the free and bound states of the molecule, respectively. The time rate of change of M_f and M_b can be obtained by adding the right-hand-sides of Eqs. (5.27), (5.28) and (5.29), viz.,

$$\frac{dM_f(z,t)}{dt} = i\left(\omega_{0f} - \omega_{rf}\right)M_f(z,t) + D_f\left(\frac{\partial^2 M_f(z,t)}{\partial z^2}\right) - \frac{M_f(z,t)}{\tau_f} + \frac{M_b(z,t)}{\tau_b} - \frac{M_f(z,t)}{T_{2f}},$$
$$\frac{dM_b(z,t)}{dt} = i\left(\omega_{0b} - \omega_{rf}\right)M_b(z,t) + D_b\left(\frac{\partial^2 M_b(z,t)}{\partial z^2}\right) - \frac{M_b(z,t)}{\tau_b} + \frac{M_f(z,t)}{\tau_f} - \frac{M_b(z,t)}{T_{2b}}. \tag{5.30}$$

If $\omega_{0f} = \omega_{0b}$ then ω_{rf} can be set equal to both ω_{0f} and ω_{0b} which eliminates the first term in both equations in Eq. (5.30), giving,

$$\frac{\partial M_f(z,t)}{\partial t} = D_f\left(\frac{\partial^2 M_f(z,t)}{\partial z^2}\right) - \frac{M_f(z,t)}{\tau_f} + \frac{M_b(z,t)}{\tau_b} - \frac{M_f(z,t)}{T_{2f}} \tag{5.31}$$

$$\frac{\partial M_b(z,t)}{\partial t} = D_b\left(\frac{\partial^2 M_b(z,t)}{\partial z^2}\right) - \frac{M_b(z,t)}{\tau_b} + \frac{M_f(z,t)}{\tau_f} - \frac{M_b(z,t)}{T_{2b}}. \tag{5.32}$$

This elimination can only occur if the chemical shifts of the free and bound states are identical. This is a not uncommon occurrence (e.g., refs. [84, 167]). Different chemical shifts complicate the analysis, and will not be considered here. A similar elimination of the last term can be made in Eqs. (5.31) and (5.32) if $T_{2f} = T_{2b}$. So in effect, the Kärger equations will only rely on the combination of the diffusion and exchange equations (Eqs. (5.27) and (5.28)) with all the Bloch equation terms vanishing under the conditions being considered.

Eqs. (5.31) and (5.32) describe the evolution of the transverse magnetisation under diffusion, exchange between the free and bound states, and the effects of spin-spin relaxation. Given an initial magnetisation profile for the free and bound states, $M_f(z,0)$ and $M_b(z,0)$, Eqs. (5.31) and (5.32) can be used to get the transverse magnetisation profile at a later time. However, the real interest is in determining the degree of signal attenuation of a magnetisation helix after time Δ (at this time the helix is unwound and the signal intensity measured). Fortunately, it is quite easy to obtain ordinary differential equations that describe such signal attenuation by substituting,

$$M_f(z,t) = S_f(t)\exp(2\pi iqz) \tag{5.33}$$

and,

$$M_b(z,t) = S_b(t)\exp(2\pi iqz), \tag{5.34}$$

into Eqs. (5.31) and (5.32) where q is defined as in Eq. (5.20).

All the information about the magnitudes of the helices is contained in $S_f(t)$ and $S_b(t)$. If the helix is unwound at time Δ and a signal acquired, then the signal strength is proportional to $S_f(\Delta)$ and $S_b(\Delta)$. The equations governing $S_f(t)$ and $S_b(t)$ are called the Kärger equations, which can be obtained by making the substitutions given above (Eqs. (5.33) and (5.34) in Eqs. (5.31) and (5.32) and then dividing out the factor of $\exp(2\pi iqz)$), viz.,

$$\frac{dS_f(t)}{dt} = -GD_f S_f(t) - \frac{S_f(t)}{\tau_f} + \frac{S_b(t)}{\tau_b} - \frac{S_f(t)}{T_{2f}}, \tag{5.35}$$

and,

$$\frac{dS_b(t)}{dt} = -GD_bS_b(t) - \frac{S_b(t)}{\tau_b} + \frac{S_f(t)}{\tau_f} - \frac{S_b(t)}{T_{2b}} \tag{5.36}$$

where $G = (2\pi q)^2$.

According to these equations, the change in the signal intensity of the free species over time, t, is a result of the signal intensities lost due to diffusion and T_2 decay, and the intensities added via exchange (i.e., signal intensity from the bound species) [168]. This is represented schematically in Figure 33.

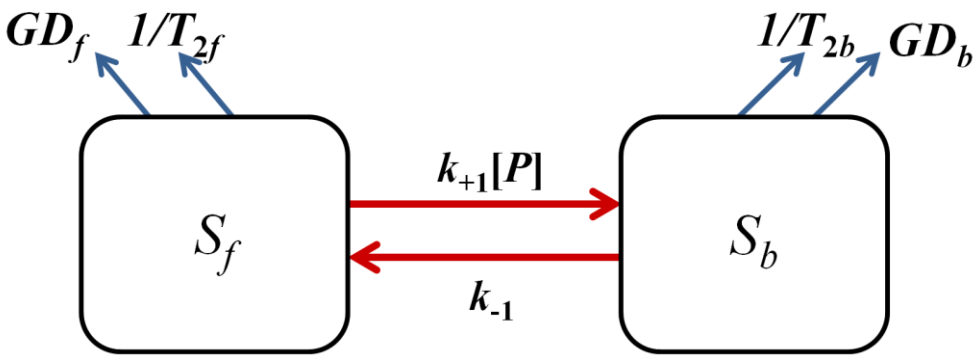

Figure 33: S_f and S_b represent the signal intensities of a free and bound species, respectively. The two species in exchange are linked by the forward and reverse rate constants. *GD* represents the rate constant associated with signal intensity loss due to diffusion and $1/T_2$ the rate constant associated with signal intensity loss due to spin-spin relaxation over time.

If it is assumed that T_2 is either the same for the free and bound complex (i.e., $T_{2f} = T_{2b} = T_2$) or is significantly long relative to the timescale of the experiment [76], the equations can be simplified to,

$$\frac{dS_f(t)}{dt} = -GD_fS_f(t) - \frac{S_f(t)}{\tau_f} + \frac{S_b(t)}{\tau_b} \tag{5.37}$$

and

$$\frac{dS_b(t)}{dt} = -GD_bS_b(t) - \frac{S_b(t)}{\tau_b} + \frac{S_f(t)}{\tau_f} \tag{5.38}$$

by making the substitutions $S_f(t) \rightarrow S_f(t)\exp(-t/T_2)$ and $S_b(t) \rightarrow S_b(t)\exp(-t/T_2)$ in Eqs. (5.37) and (5.38) in the first case and by neglecting the relaxation terms in the second case (i.e., approximating $1/T_2$ as zero).

5.3.3 Solving the Two-Site Kärger Equations for Two Freely Diffusing Species

5.3.3.1 General Solution

To solve the two-site Kärger equations, Eqs. (5.37) and (5.38), which are two coupled first-order differential equations, the first task is to uncouple them. Making $S_b(t)$ the subject of Eq. (5.37) gives,

$$S_b(t) = \tau_b\left[\frac{dS_f(t)}{dt} + GD_fS_f(t) + \frac{S_f(t)}{\tau_f}\right], \tag{5.39}$$

which upon differentiation yields,

$$\frac{dS_b(t)}{dt} = \tau_b\left[\frac{d^2S_f(t)}{dt^2} + \left(GD_f + \frac{1}{\tau_f}\right)\frac{dS_f(t)}{dt}\right]. \tag{5.40}$$

Substituting Eq. (5.39) into Eq. (5.38) and simplifying yields,

$$\frac{dS_b(t)}{dt} + GD_bS_b(t) + \frac{dS_f(t)}{dt} + GD_fS_f(t) = 0. \tag{5.41}$$

Eqs. (5.39) and (5.40) are then substituted into Eq. (5.41) and simplified,

$$\frac{d^2S_f(t)}{dt^2}+\left(G(D_f+D_b)+\frac{1}{\tau_f}+\frac{1}{\tau_b}\right)\frac{dS_f(t)}{dt}+\left(G^2D_bD_f+\frac{GD_b}{\tau_f}+\frac{GD_f}{\tau_b}\right)S_f(t)=0\ . \quad (5.42)$$

Eq. (5.42) is a second order homogenous linear ordinary differential equation (ODE) (e.g., Ref.[161]). Note that it is uncoupled from $S_b(t)$. A similar expression can be obtained for $S_b(t)$, but note that $S_b(t)$ can be obtained from Eq. (5.39) by substituting the solution for $S_f(t)$.

The next task is to solve Eq. (5.42). Substituting $S_f(t) = \exp(\lambda t)$ into Eq. (5.42) and dividing out the common factor $\exp(\lambda t)$ gives a characteristic equation of the form $a\lambda^2 + b\lambda + c = 0$, viz.,

$$\lambda^2+\left(G(D_f+D_b)+\frac{1}{\tau_f}+\frac{1}{\tau_b}\right)\lambda+\left(G^2D_bD_f+\frac{GD_b}{\tau_f}+\frac{GD_f}{\tau_b}\right)=0. \quad (5.43)$$

The roots of the above quadratic equation can then be determined by considering $\lambda_1,\lambda_2=\frac{-b\pm\sqrt{b^2-4ac}}{2a}$, where $a=1$, $b=G(D_f+D_b)+\frac{1}{\tau_f}+\frac{1}{\tau_b}$ and $c=G^2D_bD_f+\frac{GD_b}{\tau_f}+\frac{GD_f}{\tau_b}$.

The general solution is,

$$S_f(t)=C_1\exp(\lambda_1 t)+C_2\exp(\lambda_2 t)\,, \quad (5.44)$$

where, after simplification,

$$\lambda_1, \lambda_2 = \frac{1}{2}\left[-\left(G(D_f + D_b) + \frac{1}{\tau_f} + \frac{1}{\tau_b} \right) \pm G\sqrt{\left(D_b - D_f + \frac{1}{G}\left(\frac{1}{\tau_b} - \frac{1}{\tau_f} \right) \right)^2 + \frac{4}{G^2 \tau_b \tau_f}} \right], \quad (5.45)$$

and C_1 and C_2 are arbitrary constants.

Eq. (5.44) with Eq. (5.45) give the general solution to Eq. (5.42). The final step is to find appropriate expressions for C_1 and C_2 in terms of the initial populations of the free and bound states.

At $t = 0$, the signal of the free and bound components are proportional to the free P_f and bound P_b populations, respectively. Since only relative signal amplitudes are of concern, the constant of proportionality can be set to unity and the signals at $t = 0$ are then given by $S_f(0) = P_f$ and $S_b(0) = P_b$. From Eq. (5.44), it is seen $S_f(0) = C_1 + C_2$. Therefore,

$$C_1 = P_f - C_2 . \quad (5.46)$$

Writing $\lambda_1 = -GD_1$ and $\lambda_2 = -GD_2$, Eq. (5.44) can be written as,

$$S_f(t) = (P_f - C_2)\exp(-GD_1 t) + C_2 \exp(-GD_2 t), \quad (5.47)$$

where,

$$D_1 = \frac{1}{2}\left[D_f + D_b + \frac{1}{G}\left(\frac{1}{\tau_f} + \frac{1}{\tau_b} \right) - \sqrt{\left(D_b - D_f + \frac{1}{G}\left(\frac{1}{\tau_b} - \frac{1}{\tau_f} \right) \right)^2 + \frac{4}{G^2 \tau_b \tau_f}} \right] \quad (5.48)$$

and

$$D_2 = \frac{1}{2}\left[D_f + D_b + \frac{1}{G}\left(\frac{1}{\tau_f} + \frac{1}{\tau_b} \right) + \sqrt{\left(D_b - D_f + \frac{1}{G}\left(\frac{1}{\tau_b} - \frac{1}{\tau_f} \right) \right)^2 + \frac{4}{G^2 \tau_b \tau_f}} \right]. \quad (5.49)$$

Now to obtain an expression for C_2. The initial rate of change of the free signal with respect to time is obtained by differentiating Eq. (5.47) with respect to time and evaluating at $t = 0$, viz.,

$$\left.\frac{dS_f(t)}{dt}\right|_{t=0} = -GD_1(P_f - C_2) - GD_2C_2 . \tag{5.50}$$

Eq. (5.37) can also be evaluated to obtain the initial rate of change of the free signal with respect to time,

$$\left.\frac{dS_f(t)}{dt}\right|_{t=0} = -GD_fP_f - \frac{P_f}{\tau_f} + \frac{P_b}{\tau_b}, \tag{5.51}$$

where $S_f(0)$ and Sb(0) have been replaced by P_f and P_b, respectively. Note, however, Eq. (5.14) means that the last two terms on the right hand side of Eq. (5.51) vanish. Thus equating the right hand sides of Eqs. (5.50) and (5.51) and solving for C_2 gives,

$$C_2 = \frac{D_fP_f - D_1P_f}{D_2 - D_1} . \tag{5.52}$$

If Eq. (5.38) is solved for $S_b(t)$, an equation identical in form to Eq. (5.47) can be derived,

$$S_b(t) = (P_b - C_2^{'})\exp(-GD_1\Delta) + C_2^{'}\exp(-GD_2\Delta). \tag{5.53}$$

Applying the same method used to determine C_2, C_2':

$$C_2' = \frac{D_b P_b - D_1 P_b}{D_2 - D_1}. \tag{5.54}$$

Therefore, the solutions for the free and bound signal intensities are,

$$S_f(t) = \frac{D_2 P_f - D_f P_f}{D_2 - D_1} \exp(-GD_1 t) + \frac{D_f P_f - D_1 P_f}{D_2 - D_1} \exp(-GD_2 t) \tag{5.55}$$

and

$$S_b(t) = \frac{D_2 P_b - D_b P_b}{D_2 - D_1} \exp(-GD_1 t) + \frac{D_b P_b - D_1 P_b}{D_2 - D_1} \exp(-GD_2 t), \tag{5.56}$$

respectively. The total attenuation E is defined to be the sum of the signal originating from the free and bound states at time $t = \Delta$ (the time at which the magnetisation helix is actually unwound and the signal acquired),

$$E = S_b(\Delta) + S_f(\Delta), \tag{5.57}$$

giving,

$$E = P_1 \exp(-GD_1 \Delta) + P_2 \exp(-GD_2 \Delta), \tag{5.58}$$

where,

$$P_1 = \frac{D_2 P_f - D_f P_f + D_2 P_b - D_b P_b}{D_2 - D_1} \tag{5.59}$$

and

$$P_2 = \frac{D_f P_f - D_1 P_f + D_b P_b - D_1 P_b}{D_2 - D_1}. \tag{5.60}$$

Note that $P_1 + P_2 = P_f + P_b$. Now that the general solutions have been developed, Eq. (5.58) can be examined in the limits of slow and fast exchange.

5.3.3.2 Slow Exchange Limit

For $\tau_b, \tau_f \to \infty$, the second order term, $4/\left(G^2\tau_b\tau_f\right)$ in Eqs. (5.48) and (5.49), approaches zero and D_1 and D_2 become,

$$D_1 = D_f + \frac{1}{G\tau_f} \tag{5.61}$$

and

$$D_2 = D_b + \frac{1}{G\tau_b} \tag{5.62}$$

Substituting Eqs. (5.61) and (5.62) into (5.58) yields the solution in the slow exchange limit,

$$\begin{aligned} E = &\left(\frac{D_2 - D_b P_b - D_f P_f}{D_2 - D_1}\right) \\ &\times \exp\left(-(2\pi q)^2\left(D_f + \frac{1}{2\pi q\tau_f}\right)\Delta\right) + \left(\frac{D_b P_b + D_f P_f - D_1}{D_2 - D_1}\right)\exp\left(-(2\pi q)^2\left(D_b + \frac{1}{2\pi q\tau_b}\right)\Delta\right) \end{aligned} \tag{5.63}$$

5.3.3.3 Fast Exchange Limit

When $\tau_b, \tau_f \to 0$, $\left(1/\tau_f + 1/\tau_b\right) \to \infty$, hence D_2 in Eq. (5.58) becomes infinite (see the definition of D_2 in Eq. (5.49)) and therefore, the term $\exp(-GD_2\Delta)$ vanishes. The same approach applied to D_2 cannot be applied to D_1 and the first term in Eq. (5.58) must be considered in detail. By completing the square to match the non-square root component of Eq. (5.48), D_1 can be rewritten as

$$D_1 = \frac{1}{2}\left[D_b + D_f + \frac{1}{G}\left(\frac{1}{\tau_f} + \frac{1}{\tau_b}\right) - \sqrt{\left[D_b + D_f + \frac{1}{G}\left(\frac{1}{\tau_b} + \frac{1}{\tau_f}\right)\right]^2 - 4D_bD_f - \frac{4D_b}{G\tau_f} - \frac{4D_f}{G\tau_b}}\right] \tag{5.64}$$

Since, the typical diffusion values are of the order of magnitude of 10^{-9} m^2s^{-1}, $4D_bD_f$ can be neglected. Therefore,

$$D_1 \approx \frac{1}{2}\left[D_b + D_f + \frac{1}{G}\left(\frac{1}{\tau_f}+\frac{1}{\tau_b}\right) - \sqrt{\left[D_b + D_f + \frac{1}{G}\left(\frac{1}{\tau_b}+\frac{1}{\tau_f}\right)\right]^2 - \frac{4\left(D_b\tau_b + D_f\tau_f\right)}{G\tau_b\tau_f}}\right]$$
$$= \frac{1}{2}\left[D_b + D_f + \frac{1}{G}\left(\frac{1}{\tau_f}+\frac{1}{\tau_b}\right) - \left[D_b + D_f + \frac{1}{G}\left(\frac{1}{\tau_b}+\frac{1}{\tau_f}\right)\right]\sqrt{1 - \frac{\frac{4\left(D_b\tau_b + D_f\tau_f\right)}{G\tau_b\tau_f}}{\left[D_b + D_f + \frac{1}{G}\left(\frac{1}{\tau_b}+\frac{1}{\tau_f}\right)\right]^2}}\right]. \quad (5.65)$$

Noting that to first order $\sqrt{1-x} = 1-\frac{1}{2}x$, Eq. (5.65) becomes,

$$D_1 \approx \frac{\frac{\left(D_b\tau_b + D_f\tau_f\right)}{G\tau_b\tau_f}}{\left[D_b + D_f + \frac{1}{G}\left(\frac{1}{\tau_b}+\frac{1}{\tau_f}\right)\right]}. \quad (5.66)$$

The sum of D_b and D_f in the denominator is very small compared to the other term and therefore can be neglected. Eq. (5.66) then simplifies to,

$$D_1 \approx \frac{D_b}{\frac{\tau_f}{\tau_b}+1} + \frac{D_f\frac{\tau_f}{\tau_b}}{\frac{\tau_f}{\tau_b}+1}. \quad (5.67)$$

By considering the ratio of the lifetimes of the two states relative to the ratio of the populations of the two states (see Eq. (5.14)), it can be seen

$$\frac{\tau_f}{\tau_b} = \frac{P_f}{P_b}, \tag{5.68}$$

which yields

$$D_1 \approx \frac{D_b P_b + D_f P_f}{P_f + P_b} \ . \tag{5.69}$$

Recalling Eq. (5.10), D_1 simplifies to

$$D_1 \approx D_b P_b + D_f P_f . \tag{5.70}$$

Thus, E for the fast exchange limit becomes,

$$E = P_1 \exp\left(-(2\pi q)^2 (D_b P_b + D_f P_f)\Delta\right) \tag{5.71}$$

To use Eq. (5.26), the exchanging system must be in fast exchange relative to the measurement timescale. As the primary concern is with events on the timescale of Δ in diffusion measurements of an exchanging system, a cogent choice of Δ allows the switch between slow and fast exchange.

As an example to the application of Eq. (5.70), the simple and commonly used intermolecular exchange model of a ligand (L) exchangeably binding with a macromolecule receptor (P), forming a complex (LP) with n identical independent ligand binding sites is considered. The system at equilibrium is described by

$$L + P \underset{k_{-1}}{\overset{k_{+1}}{\rightleftharpoons}} LP \tag{5.72}$$

where the forward rate constant, k_{+1} ($M^{-1}s^{-1}$), favours the binding of the protein and ligand molecules and the reverse rate constant k_{-1} (s^{-1}), favours the separation of the protein and ligand. Hence, the dissociation constant of the complex, K_d (M), is defined by,

$$K_d = \frac{[L][P]}{[LP]} = \frac{k_{-1}}{k_{+1}}. \tag{5.73}$$

The lifetimes of the ligand molecule in the free (*f*) and bound (*b*) states can be related to the forward and reverse rate constants by

$$\tau_f = \frac{1}{k_{+1}[P]} \text{ and } \tau_b = \frac{1}{k_{-1}}. \tag{5.74}$$

The fractional ligand populations in the free and bounds states are given by

$$P_f = \frac{[L]}{C_L} \tag{5.75}$$

and

$$P_b = \frac{[LP]}{C_L} \tag{5.76}$$

where $[L]$ is the concentration of the free ligand, $[LP]$ is the concentration of the bound ligand and C_L is the total ligand concentration.

To use this model in the analysis of diffusion NMR experiments, it is necessary to express P_b in terms of C_L, the total protein concentration, C_P, n and K. As each protein molecule can bind n ligand molecules,

$$nC_P = [P] + [LP]. \tag{5.77}$$

The total ligand concentration is the sum of the free ligand concentration and the ligand concentration of the bound complex,

$$C_L = [L] + [LP]. \tag{5.78}$$

[LP] needs to be obtained in terms of C_L, C_P and K_d, and thus rearranging Eq. (5.77) yields

$$[LP] = nC_P - [P]. \tag{5.79}$$

Substituting [P] and [L] from Eqs. (5.73) and (5.78), respectively,

$$[LP] = nC_P - \frac{K_d[LP]}{C_L - [LP]}. \tag{5.80}$$

Rearranging Eq. (5.80) to form a quadratic equation yields

$$[LP]^2 - (C_L + nC_P + K_d)[LP] + nC_P C_L = 0. \tag{5.81}$$

This can then be solved for [LP] giving,

$$[LP] = \frac{(C_L + nC_P + K_d) \pm \sqrt{(C_L + nC_P + K_d)^2 - 4nC_P C_L}}{2} \quad . \tag{5.82}$$

Substitution of Eq. (5.82) into Eq. (5.76) yields,

$$P_b = \frac{(C_L + nC_P + K_d) \pm \sqrt{(C_L + nC_P + K_d)^2 - 4nC_P C_L}}{2C_L}, \tag{5.83}$$

or more concisely,

$$P_b = \alpha - \sqrt{\alpha^2 - \beta} \quad , \tag{5.84}$$

where $\alpha = \frac{(C_L + nC_P + K_d)}{2C_L}$ and $\beta = \frac{nC_P}{C_L}$. By substituting Eq. (5.83) into Eq. (5.70), it is possible to quantitatively characterise binding interactions via *n* and *K* using the measured diffusion coefficient (e.g., refs.[83, 84, 169]).

5.3.4 Extension to a Three-State Binding Model

The two-site binding model distinguishes two states (e.g. bound and free) during equilibrium binding interactions. However, in some cases, it is unrealistic to define only two states and a third state may be applicable. Such cases arise when structural distortions caused by covalent interactions are not fully captured by the two-site/two-state model, or multiple binding sites are present (e.g., in albumin). In such cases, it may be appropriate to define an intermediate state, in addition to the free and bound states. In the context of protein-ligand binding, an intermediate state may serve as one where the ligands bind to a different site relative to those defined as bound, with different binding properties (i.e., weak binding relative to those that are “bound”), as shown in Figure 34.

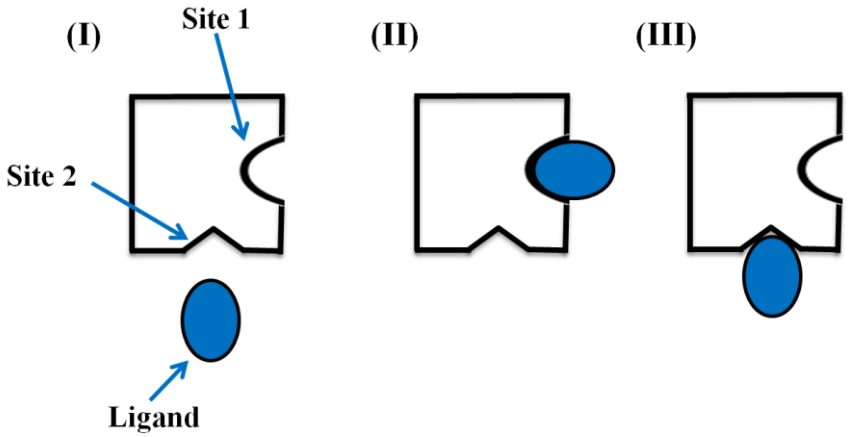

Figure 34: Schematic showing the three possible independent states where (I) - the ligand is free (free state), (II) – the ligand is bound (bound state), and (III) – where the ligand is weakly bound (intermediate state).

The presence of a third state expands the two-state model (i.e., Eq. (5.26)) to

$$D = P_b^{'} D_b + P_b^{"} (D_b + \varepsilon_b) + (1 - P_b^{'} - P_b^{"}) D_f \tag{5.85}$$

where $P_b^{'}$ and $P_b^{"}$ are the populations of the bound and intermediate state, respectively, and ε_b is the diffusion coefficient difference between the bound and intermediate complexes. If P_b^{*} is the total population of the bound states (i.e., bound and intermediate states, as the intermediate state is still considered a bound state),

$$P_b^{*} = P_b^{'} + P_b^{"} \tag{5.86}$$

and ΔD is defined as

$$\Delta D = D_b - D_f, \tag{5.87}$$

then Eq. (5.85) can be rewritten as

$$D = P_b^{*} \Delta D + D_f + P_b^{"} \varepsilon_b. \tag{5.88}$$

5.4 Conclusions

The routine use of NMR methods to quantitatively determine association/dissociation constants of ligand-protein binding has long been established, predominantly due to the non-invasive nature of NMR. NMR measurements preserve the chemical environment of the ligand-protein solution, which is an important aspect of equilibrium measurements. Of these methods, NMR diffusion measurements allow binding ligands (which assume the diffusion properties of the protein) to be easily differentiated from non-binding molecules by significant differences in the diffusion coefficients. From such measurements, the Kärger model allows association constants to be determined.

This chapter provides a comprehensive derivation of the two-site Kärger model for two freely diffusing species and considers both the slow and fast exchange limits. The derivation of the Kärger model begins by combining the diffusion and exchange equations, ultimately leading to the population weighted diffusion equation under fast exchange conditions. This equation will be used to analyse the binding interactions discussed in the following chapter.

Chapter 6. Binding Interactions of Different Hypoxia-Targeting Vectors

This chapter contains verbatim passages from:

Dj Wijesekera, Scott A. Willis, Abhishek Gupta, Allan M. Torres, Gang Zheng, William S. Price, NMR diffusion and relaxation studies of 2-nitroimidazole and albumin interactions, *Spectrochimica Acta Part A: Molecular and Biomolecular Spectroscopy*, 193 (2018) 318-323.

6.1 Introduction

With the numerous hypoxia-targeting vectors available as discussed in Chapter 1, it becomes paramount to determine which holds the most promise to be used as a hypoxia-targeting vector prior to developing any pO_2 detection methods involving these vectors. A suitable model for such determinations can be obtained from drug development processes, where early stages usually involve characterising drug interactions with plasma proteins [170-174]. Plasma proteins, e.g., serum albumin, provide key physiological functions such as transport to externally administered drugs due to its abundance and numerous binding sites (i.e., covalent, specific and non-specific) [170, 175]. Bovine serum albumin (BSA) is a single-chain 582 amino acid globular non-glycoprotein cross-linked with 17 cystine residues, with a structure similar to human serum albumin (HSA) and is considered an ideal *in vitro* model for studying drug-protein binding [171, 176, 177].

Drug-protein interactions can be studied using various techniques such as optical spectroscopy [178-180], radioactive isotope labelling [181], high performance liquid chromatography [182] and NMR [149, 150, 183-187]. Of these, NMR is particularly useful since it can provide information on the molecular motion (diffusion) and the local environment of the drugs/protein (relaxation). NMR diffusion measurements can probe the change in the apparent self-diffusion coefficient of the drug molecule as a function of concentration [188]. As the drug molecule binds to the protein, its apparent diffusion coefficient decreases due to its interactions with the much larger and more slowly diffusing protein molecule. Similarly, NMR relaxation experiments exploit the differences in the free and bound relaxation properties of the drug molecule [185]. The relaxation time constants of the molecules are dependent on their molecular reorientational motion (and thus, reorientational correlation time, τ_c). For small, fast reorientating molecules (where $\omega_0\tau_c << 1$), the relaxation time constants decrease with increasing τ_c [88]. The protein-bound drug molecules are expected to relax at a different rate to the unbound, freely diffusing molecules.

In this chapter, the binding of three hypoxia-targeting vectors to BSA via NMR diffusion and relaxation measurements will be investigated. The three hypoxia-targeting vectors selected are 2-nitroimidazole, 4-nitroimidazole and 6-nitroquinoline. Where applicable, the binding process will be quantified using a two-site binding model for both diffusion and relaxation measurements. The different protein concentrations studied are in

accordance to a previous NMR binding study [189], with variable hypoxia-targeting vector concentrations.

6.2 Experimental

6.2.1 Materials

BSA (heat shock fraction, pH 7, ≥ 98%), 2-nitroimidazole (98%), 4-nitroimidazole (97%) and 6-nitroquinoline (98%) were purchased from Sigma-Aldrich (Australia). Deuterium oxide (D_2O) (99.8% D) and sodium deuteroxide (99.5% D, 40% in D_2O) were purchased from Cambridge Isotope Laboratories Inc (USA). NMR tubes (5 mm, 535-PP-7) were purchased from Wilmad LabGlass (USA).

6.2.2 Sample Preparation

Stock solutions of 2-nitroimidazole and 4-nitroimidazole in D_2O of 0.3 M were adjusted to pH ≈ 9.4 and 10.9, respectively using dilute NaOD solution. A 0.3 M stock solution of 6-nitroquinoline in dimethylformamide (DMF) was also prepared. The stock solutions were further diluted to prepare samples for each vector (i.e., 2-nitroimidazole, 4-nitroimidazole and 6-nitroquinoline) of concentrations ranging from 0.001 - 0.16 M, with protein concentrations of 0.23, 0.30 or 0.38 mM. The protein and drug concentrations were based on an earlier study investigating the binding of a similar drug and protein molecule [190].

6.2.3 NMR Measurements

All NMR experiments were performed on a Bruker Avance III 500 MHz spectrometer (Bruker Biospin, Germany) using a 5 mm PABBI-Z inverse probe at 298 K (This temperature was chosen to facilitate comparison with an earlier study investigating protein-ligand binding by NMR [191]). The calibrated maximum gradient amplitude along the z-axis was 53.5 G cm^{-1}. Diffusion measurements were obtained using a PGSTE sequence [192], with a diffusion time (Δ) of 70 ms and gradient pulse durations (δ) of 1.5 ms. Twenty gradient strengths, ranging from 0.11 to 50.93 G cm^{-1} in increments of 2.68 G cm^{-1}, were used and each spectrum was acquired with 8 scans. Longitudinal and transverse relaxation decay constants, T_1 and T_2, respectively, were obtained using the inversion recovery [72] and CPMG sequences [74, 75], respectively. The signal from the inversion recovery pulse sequence ($\pi - \tau - \pi/2 -$ acquire) was acquired for 16 different values of time, τ while the CPMG sequence ($\pi/2 - [\tau/2 - \pi - \tau/2]_n -$ acquire) was acquired for 16 different values of n, with τ_{CPMG} fixed to 3 ms. The signal was averaged over 4 scans for T_1 and T_2, with the recycle delay set to $\geq 5T_1$.

6.2.4 Data Fitting

All data fitting was performed using OriginPro 9.1 (OriginLab, USA). Diffusion coefficients, D, were determined by regressing the equation [76, 90, 193, 194]

$$E = C\exp\left(-bD\right) + E_{Off}, \tag{6.1}$$

onto the PGSTE attenuation data. In this equation, E is the attenuation of the echo signal. $b = \left(\gamma\delta g\right)^2\left(\Delta - \frac{\delta}{3}\right)$, where γ and g are the gyromagnetic ratio and gradient pulse amplitude, respectively. Eq. (6.1) includes a floating amplitude, C, and baseline offset, E_{off} to accommodate for the slow diffusing protein component, whose signal shows little attenuation for the b values used [193, 194]. Likewise, to accommodate for the differently relaxing species, biexponential fits, Eqs. (6.2) and (6.3), were used for analysing the relaxation measurements,

$$\begin{aligned} M_z &= M_{zA}^{eq}\left[1 - 2\exp\left(\frac{-\tau}{T_{1A}}\right)\right] + M_{zB}^{eq}\left[1 - 2\exp\left(\frac{-\tau}{T_{1B}}\right)\right] \\ &= a_1 - a_2\exp\left(\frac{-\tau}{T_{1A}}\right) - a_3\exp\left(\frac{-\tau}{T_{1B}}\right) \end{aligned} \tag{6.2}$$

$$M_{xy} = M_{xyA}^{eq}\left[\exp\left(\frac{-n\tau_{CPMG}}{T_{2A}}\right)\right] + M_{xyB}^{eq}\left[\exp\left(\frac{-n\tau_{CPMG}}{T_{2B}}\right)\right] \tag{6.3}$$

where M_z and M_{xy} represent the longitudinal and transverse magnetisation at times τ or $n \times \tau_{CPMG}$, respectively, M^{eq} is the equilibrium magnetisation, and T_1 and T_2 are the relaxation decay constants of the two components, A and B. A and B refers to the vector and BSA, respectively. a_1 is $M_{zA}^{eq} + M_{zB}^{eq}$, a_2 is $2M_{zA}^{eq}$ and a_3 is $2M_{zB}^{eq}$.

The two-site Kärger model [151, 152, 167, 181] was simultaneously fit (i.e., global fit) to all NMR measurements (D, T_1 and T_2) to determine the number of binding sites, n and the association constant, K. Eqs. (6.4) and (6.5) were used for diffusion and relaxation measurements, respectively,

$$D = \left(\alpha - \sqrt{\alpha^2 - \beta}\right)D_b + \left(1 - \left(\alpha - \sqrt{\alpha^2 - \beta}\right)\right)D_f \tag{6.4}$$

$$R = \left(\alpha - \sqrt{\alpha^2 - \beta}\right) R_b + \left(1 - \left(\alpha - \sqrt{\alpha^2 - \beta}\right)\right) R_f \tag{6.5}$$

where

$$\alpha = \frac{\left(C_{vector} + nC_{BSA} + 1/K\right)}{2C_{vector}} \tag{6.6}$$

and

$$\beta = \frac{nC_{BSA}}{C_{vector}} \, . \tag{6.7}$$

R denotes the relaxation rate (where b and f represent the bound and free states). C_{vector} and C_{BSA} are the concentrations of the vector and BSA, respectively.

6.3 Results and Discussion

6.3.1 2-nitroimidazole

As the hydrogen from the amine of 2-nitroimidazole exchanges with the deuterium in solution and is not visible in the ^{1}H spectra, the 2-nitroimidazole NMR spectrum (Figure 35) gives a single ^{1}H signal at 7.25 ppm. In this study, it is important to note the slight overlap in the ^{1}H spectra between the 2-nitroimidazole and BSA peaks as shown in Figure 35. To account for this overlap, the diffusion data was analysed with a monoexponential fit with an offset (Eq. (6.1)), and the relaxation data was analysed using biexponential fits (Eqs. (6.2) and (6.3)). It should be noted that the relaxation of BSA was fixed for the biexponential fits of the 2-nitroimidazole T_1 data. However, the contribution (i.e., signal fraction) of the BSA component was negligible in T_1 measurements as the corresponding a_i term, where i = 2 or 3, in Eq. (6.2) was approximately zero.

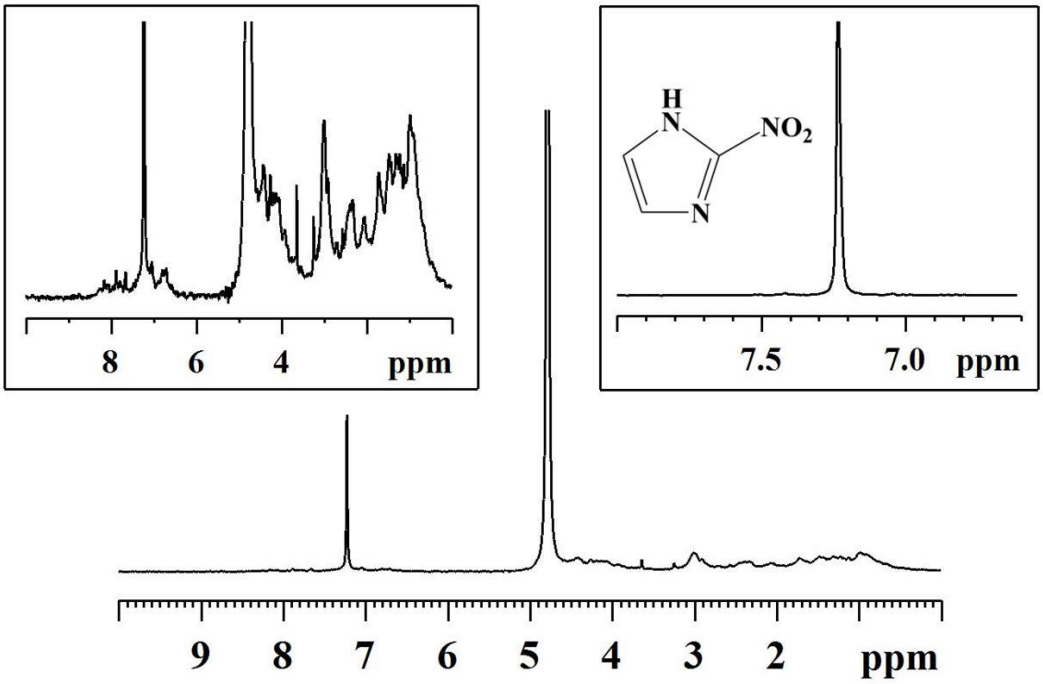

Figure 35: ^{1}H NMR spectra of 0.005 M 2-nitroimidazole and 0.38 mM BSA solution in D_2O. Left Inset: Magnified view showing the effect of BSA on the baseline of the spectrum. Right Inset: ^{1}H NMR spectrum of 0.005 M 2-nitroimidazole (and molecular structure) in D_2O between 6.6 – 8.0 ppm. The region from 7.0 – 7.5 ppm was integrated for all diffusion and relaxation measurements.

The attenuation of the 2-nitroimidazole signal was a single exponential in all cases, indicating that the 2-nitroimidazole was in fast exchange between the free and bound states on the time-scale of Δ [167, 195]. According to the two-site binding model for first-order reversible fast exchange [196-198], the observed diffusion coefficient, D, is the population weighted average of the bound and free diffusion coefficients D_b and D_f, respectively via

$$D = P_b D_b + P_f D_f \tag{6.8}$$

where the populations of bound (P_b) and free (P_f) states are;

$$P_f = 1 - P_b. \tag{6.9}$$

Assuming that the 2-nitroimidazole takes the diffusion coefficient of BSA when it's bound, the data in Figure 36 shows a greater proportion of 2-nitroimidazole in the bound state at low concentrations of the drug (i.e., higher relative BSA concentration shifts the binding equilibrium towards more bound 2-nitroimidazole). In addition, the increase in diffusion with

decreasing BSA concentration further confirms the binding of 2-nitroimidazole to BSA. As there is neither a change in the chemical shift of 2-nitroimidazole nor a loss of its NMR signal, it is unlikely that any form of chemical binding is occurring. The diffusion coefficient of the solvent (i.e., HDO in D_2O) was calculated to be $\approx 1.9 \times 10^{-9}$ m^2s^{-1} for all three protein concentrations at 0.16 M 2-nitroimidazole concentration, verifying any changes in the solution viscosity due to different protein concentrations, to be negligible. Furthermore, the protein spectra did not show any linewidth changes with increasing protein concentration. This suggests that the data was not influenced by protein aggregation. Therefore, surface binding through inter-molecular forces such as van der Waals and hydrogen bonding forces are likely to be driving the binding processes of this system [199].

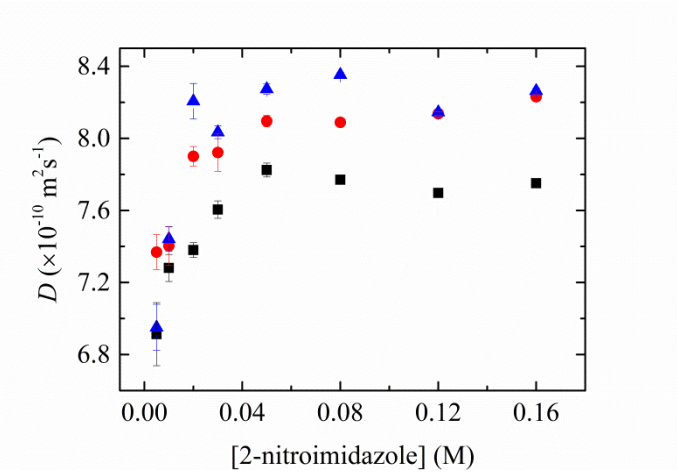

Figure 36: Diffusion coefficients of 2-nitroimidazole in BSA solutions at 298 K with BSA concentrations of 0.23 (▲), 0.3 (●) and 0.38 (■) mM.

The spin-lattice relaxation rate (R_1) and spin-spin relaxation rate (R_2) were also measured as shown in Figure 37. Applying a two-site binding model to the relaxation measurements, Eq. (6.5), the observed relaxation rates, R_1 and R_2 are the weighted average of the respective relaxation rates in the bound and free states. Similar to the diffusion measurements, a greater proportion of the 2-nitroimidazole molecules are expected to be found in the bound state at lower concentrations of the drug than at higher concentrations. Hence, the relaxation time should increase with increasing 2-nitroimidazole concentration, resulting in a corresponding decrease in the relaxation rate. This was observed in the present study, as shown in Figure 37.

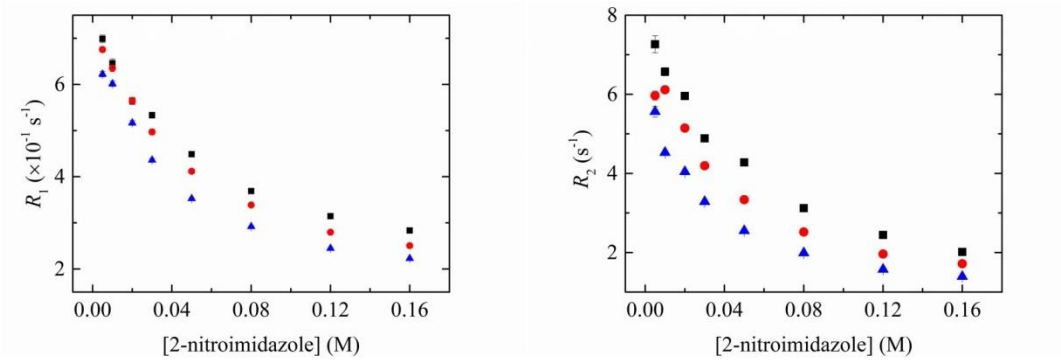

Figure 37: Relaxation measurements of 2-nitroimidazole in BSA solutions at 298 K with BSA concentrations of 0.23 (▲), 0.3 (●) and 0.38 (■) mM. Error bars for most data points lie within the symbol.

The binding model, Eq. (6.4) and (6.5), was simultaneously fit to all the datasets (i.e., D, R_1 and R_2 for all three protein concentrations and all 2-nitroimidazole concentrations) using the Levenberg Marquardt algorithm [193]. The protein concentrations were fixed. The diffusion of 0.23, 0.30 and 0.38 mM BSA (i.e., D_b) was determined to be (8.36 ± 0.28), (5.53 ± 0.11) and (4.78 ± 0.04) × 10^{-11} m^2s^{-1}, respectively. The diffusion and relaxation of 2-nitroimidazole in the absence of BSA was measured as a function of 2-nitroimidazole concentration and the results were interpolated with a second-order polynomial. In the case of relaxation, R_{1f} and R_{2f} denote the spin-lattice and spin-spin relaxation rates in the free state, respectively. The adjusted R-squared values of the second-order polynomials describing D_f, R_{1f} and R_{2f} were 0.93, 0.95 and 0.86, respectively. It is noted that seven 2-nitroimidazole concentrations were used to determine the second-order polynomial for R_{2f}, as one data point was deemed to be an outlier. The parameters, n and K were shared across all data sets. The number of binding sites was calculated to be 21 ± 3 and the association constant 53 ± 4 M^{-1}. The other calculated parameters, R_{1b} and R_{2b}, which represent the calculated relaxation measurements for 2-nitroimidazole in the bound state, are tabulated in Table 1. However, these results may suffer from imprecision. In the case of the relaxation measurements, the bound parameters (R_b) were estimated as these could not be measured directly. These parameters are strongly correlated to K, hence a small change in the relaxation of the bound values could cause a significant change to the calculated parameters of the model.

Table 1: Fitted bound state parameters for 2-nitroimidazole in BSA solutions at 298 K for different BSA concentrations where n = 21 ± 3 and K = 53 ± 4 M^{-1}. The parameters were obtained from analysis of the data over the 2-nitroimidazole concentration range of 0.005 – 0.16 M.

BSA (mM)	R_{1b} (s^{-1})	R_{2b} (s^{-1})
0.23	4.31 ± 0.57	28.68 ± 3.69
0.30	3.62 ± 0.49	29.19 ± 3.67
0.38	3.18 ± 0.45	31.25 ± 3.92

The fitted models for each data set are shown in Figure 38. The relaxation data appears to be more accurate for describing this system. This could be partly due to the increased signal-to-noise ratio for relaxation spectra compared to diffusion spectra, where the pulsed field gradients significantly reduce the signal intensity. However, care should be taken when interpreting relaxation measurements for molecules with different functional groups. This is because local molecular rotation and site dependency can complicate relaxation data, conducing to different relaxation rates for different peaks of the same molecule [181]. In contrast, the diffusion coefficient is a molecular property where different NMR peaks of a molecule describe the motion of the same molecule [181]; hence diffusion measurements can be more easily interpreted.

The NMR-based determinations of n and K in this study are in contrast to those obtained using other methods [177, 191, 200], where near equivalent protein and ligand concentrations were used to observe high-affinity specific binding, obtaining $n \approx 1$ or 2. Albumin, despite having two main binding sites (Sudlow site I & Sudlow site II) [170], has the ability to 'soak up' ligands in a non-specific manner via weak affinities. In most cases, the interaction between albumin and most small molecules can be described by a single high affinity binding site and several non-specific binding sites [191]. NMR determined n and K from studies performed at high ligand to protein ratios (as in the current study) tend to be more sensitive to low-affinity non-specific binding. The n and K values determined in this study were similar to those obtained in other NMR studies for albumin ligand solutions [145, 191].

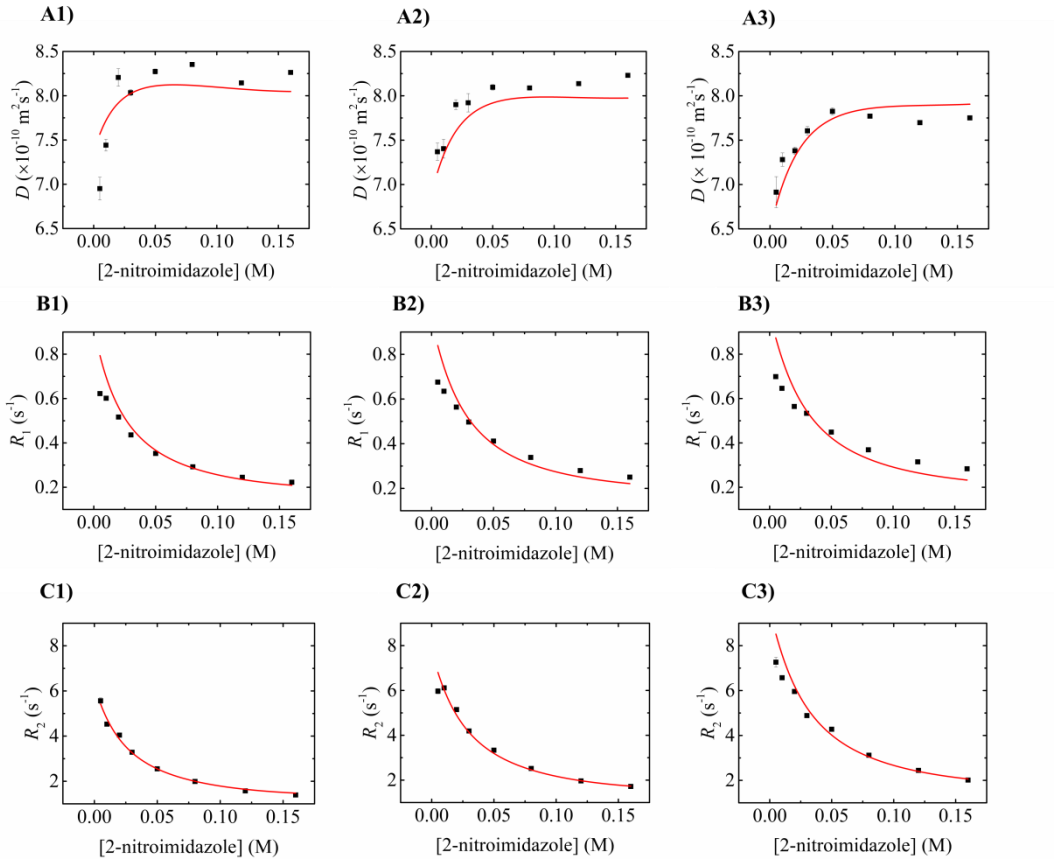

Figure 38: The two-site binding (Kärger) model fits to A) diffusion, B) R_1 and C) R_2 datasets with 1) 0.23, 2) 0.3 and 3) 0.38 mM BSA. The lines indicate the simultaneous fit of the two-site Kärger model to each of the datasets, as described in the text.

It should be noted that over-parameterisation of the binding model leads to a reduced robustness in the model, and depending on what initial values are used, multiple fits may be possible. Simultaneously fitting the data sets was deemed more appropriate than separating D, R_1 and R_2 and fitting those individually. This provided the most robust fit, with an adjusted R-squared of 0.99. A prior NMR study of salicylate binding to HSA determined n and K to be 33 and 62.5 M^{-1} (calculated from the dissociation constant, K_d = 0.016 M using $K = 1/K_d$), respectively [181]. An NMR diffusion study of salicylate binding to BSA yielded similar results for n and K of 31 ± 2 and 33 ± 4 M (calculated from K_d = 0.030 ± 0.004 M), respectively [167]. In both these studies, the samples were at pH 7.4. In the present study, a higher pH of 9.4 was used to accommodate for the insolubility of 2-nitroimidazole. It is important to note, the use of a higher pH can cause protein to unfold, which may increase the number of BSA-ligand interactions [201]. Although NMR spectroscopy revealed no significant structural changes to BSA at pH 9.4, the pH and the type of molecule can be

expected to change the binding equilibrium as observed in the results of this study. Furthermore, unlike the previous studies where each parameter was determined through individual fits, the current study fit all three NMR parameters for all BSA and 2-nitroimidazole concentrations simultaneously. To the best of our knowledge, this is the first such study involving a global fit to the data.

6.3.2 4-nitroimidazole

The molecular structure, as shown in Figure 39a, reveals three different proton (^{1}H) environments, thus should be represented as three different chemical shifts in the ^{1}H NMR spectra. In practice however, the amine of 4-nitroimidazole exchanges with the deuterium in solution and is not visible in the spectra, as shown in Figure 39b. Similar to 2-nitroimidazole, there is a slight overlap in the ^{1}H spectra between the 4-nitroimidazole and BSA peaks between 7-8 ppm. Hence the diffusion and relaxation data was analysed as reported previously (i.e., as for 2-nitroimidazole).

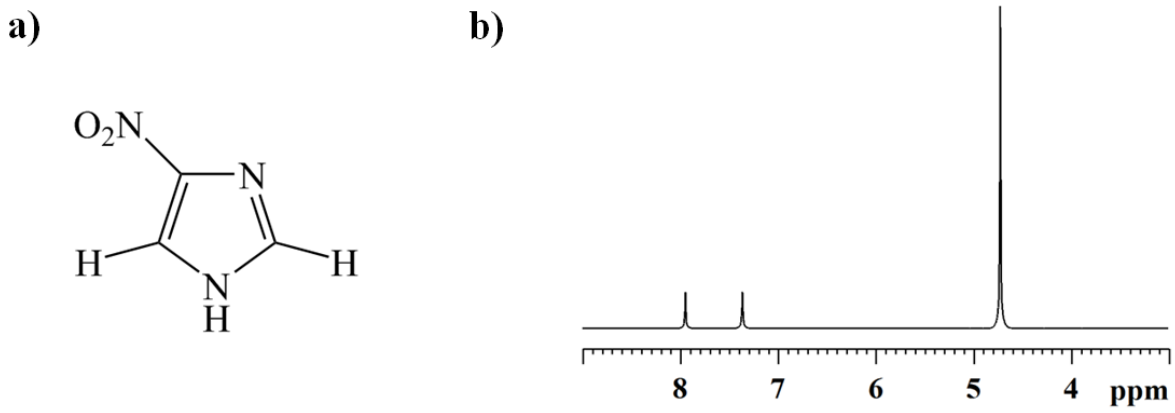

Figure 39: a) Molecular structure of 4-nitroimidazole b) ^{1}H NMR spectra of 0.005 M 4-nitroimidazole in D_2O. The ^{1}H NMR peaks of 4-nitroimidazole are found at 7.37 and 7.96 ppm.

The diffusion coefficients for 0.005, 0.02, 0.05 and 0.16 M 4-nitroimidazole in 0.30 mM BSA are shown in Figure 40. Assuming that the 4-nitroimidazole takes the diffusion coefficient of BSA when its bound, the two-site binding model states that the diffusion coefficient of the 4-nitroimidazole will increase with increasing concentration. This is not observed in Figure 40, which indicates a lack of binding between 4-nitroimidazole and BSA.

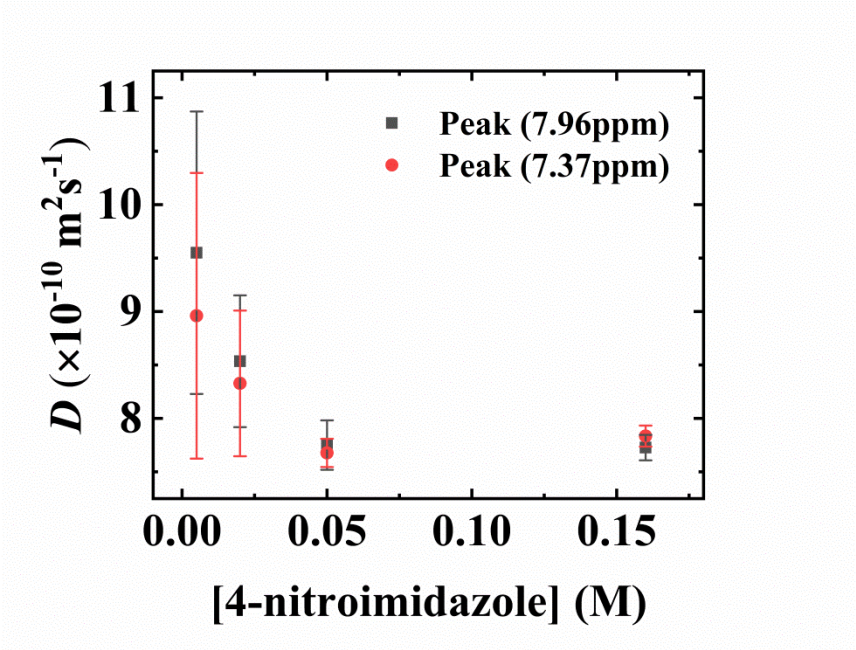

Figure 40: Diffusion coefficients of 4-nitroimidazole in 0.3 mM BSA at 298 K. The larger errors at lower concentrations are due to low signal-to-noise at these concentrations.

The diffusion coefficients in Figure 40 appear to decrease with increasing concentration. However, this is most likely exaggerated by the larger errors at low concentrations. Although, it is also possible that the diffusion coefficient decreases slightly with increasing concentration, which could be indicative of self-obstruction or aggregation, or both to a very small degree [76]. This was further confirmed to be likely by observing the diffusion coefficient of 4-nitroimidazole in D_2O for the same concentrations. The results obtained were almost identical to the diffusion coefficients obtained in the BSA solution, which indicates the behaviour of 4-nitroimidazole is no different in D_2O or BSA.

The relaxation measurements of 4-nitroimidazole in BSA are shown in Figure 41. R_{1f} of 4-nitroimidazole at peaks 7.96 and 7.37 ppm were estimated to approach 0.07 and 0.08, respectively with increasing 4-nitroimidazole concentration across the range of 0.005 – 0.16 M. R_{2f} of 4-nitroimidazole at peaks 7.96 and 7.37 ppm were estimated to approach 0.54 and 1.57 s^1, respectively. It is interesting to note that the R_1 and R_2 values of 4-nitroimidazole in BSA with increasing 4-nitroimidazole concentration approach R_{1f} and R_{2f} of 4-nitroimidazole, which would be indicative of binding according to the two-site model. Therefore, it is unclear why a similar trend was not seen with the diffusion data, and this is discussed below. With the diffusion data indicating no binding was occurring, and the global

fit in the previous section requiring all three datasets (diffusion, R_1 and R_2), no further protein concentrations were investigated for 4-nitroimidazole and no quantitative binding analysis was undertaken.

The contradicting trends between the diffusion and relaxation data are most likely due to the different time scales that these two methods (i.e., relaxation and pulsed-field gradient (PFG) NMR) report on. Generally, in experiments involving the solution state, relaxation measurements are sensitive to motions occurring in the picosecond to nanosecond time scale (i.e., motion on the time scale of the reorientational correlation of the nucleus), while in PFG measurements, motion is measured over the millisecond to second time scale [164]. Hence, it is possible that the binding interactions between BSA and 4-nitroimidazole are considerably weak, thus exchanging significantly quickly, such that it is not detected by PFG measurements (i.e., diffusion measurements).

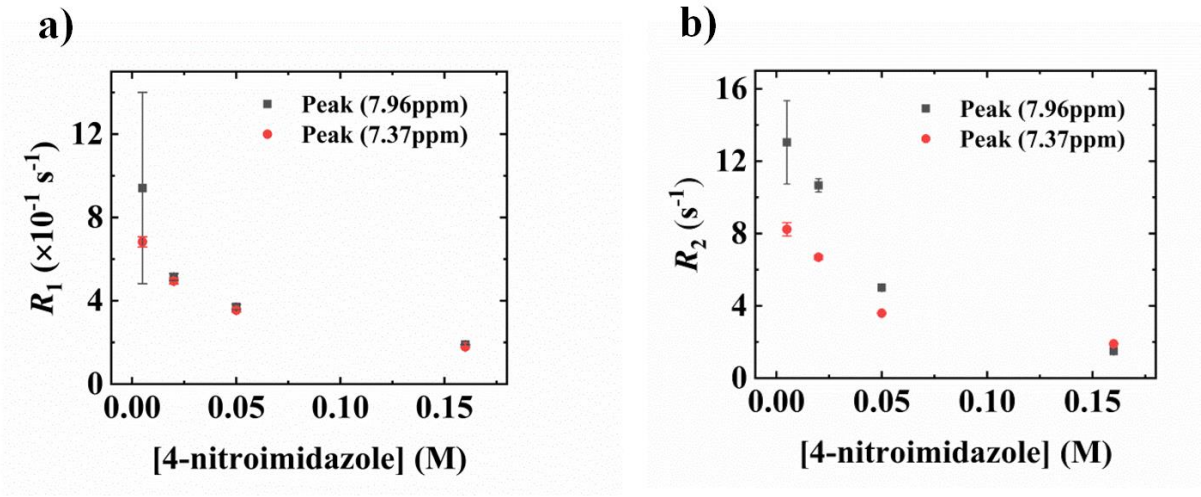

Figure 41: a) Spin-lattice and b) spin-spin relaxation rates of 4-nitroimidazole in 0.3 mM BSA at 298 K. Errors bars of most data points lie within the symbol.

6.3.3 6-nitroquinoline

The molecular structure of 6-nitroquinoline, as shown in Figure 42a reveals six different proton (^{1}H) environments, and is represented as six different chemical shifts in the ^{1}H NMR spectra (Figure 42b). Dissimilar to 2-nitroimidazole and 4-nitroimdazole, the peaks of 6-

nitroquinoline are present beyond 8 ppm, which eliminates any significant overlap with the BSA peaks. Hence the diffusion, T_1 and T_2 data were analysed with monoexponential fits;

$$E = C\exp\left(-bD\right) \tag{6.10}$$

$$M_z = M_z^{eq}\left[1-2\exp\left(\frac{-\tau}{T_1}\right)\right] \tag{6.11}$$

$$M_{xy} = M_{xy}^{eq}\left[\exp\left(\frac{-n\tau_{CPMG}}{T_2}\right)\right], \tag{6.12}$$

respectively.

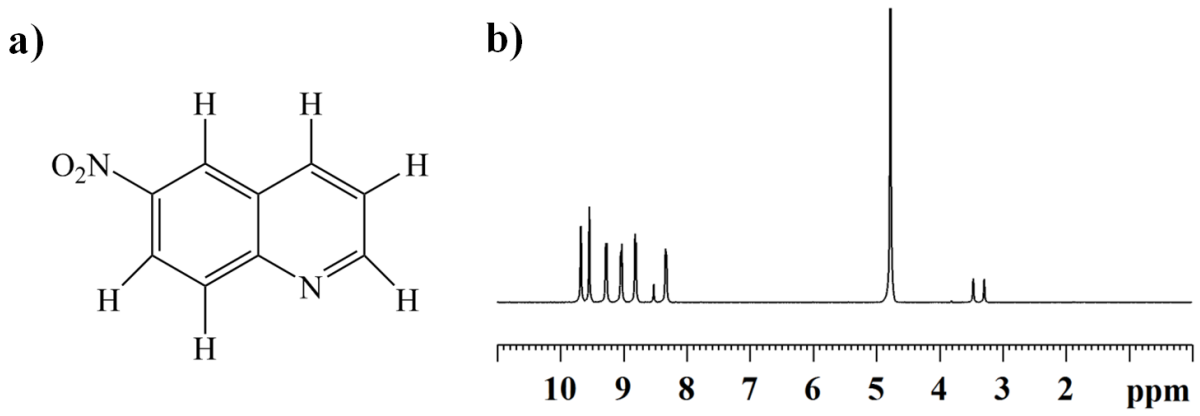

Figure 42: a) Molecular structure of 6-nitroquinoline b) ^{1}H NMR spectra of 0.16 M 6-nitroquinoline in D_2O and dimethylformamide (DMF). The ^{1}H NMR peaks of 6-nitroquinoline are found at 9.67, 9.54, 9.27, 9.03, 8.80 and 8.33 ppm. The D_2O peak is at 4.79 ppm, and the DMF peaks are at 3.31 (CH_3), 3.47 (CH_3) and 8.53 (CH) [202].

The diffusion coefficients of 6-nitroquinoline concentrations ranging from 0.001 to 0.16 M in 0.30 mM BSA are shown in Figure 43. The diffusion coefficients obtained by analysing the six peaks of 6-nitroquinoline do not conform to the trend indicative of 6-nitroquinoline binding to BSA. If the errors are considered, the diffusion coefficients either remain consistent across the defined concentration range, or otherwise, present a slight increase with decreasing concentration. If the former is considered, it is possible the diffusion coefficients may have plateaued, indicating the sample was saturated at those concentrations.

Given the low concentrations of 6-nitroquinoline studied starting at 1 mM, this is unlikely, and further lower concentrations cannot be practically investigated due to the time required to generate reasonable signal-to-noise (i.e., more scans). If the latter is considered, this is most likely indicative of self-obstruction or aggregation (again to a small degree), which is further suggested by the diffusion coefficients of the free 6-nitroquinoline samples (i.e., 6-nitroquinoline in D_2O), where a similar trend was observed with the diffusion coefficients approaching 4×10^{-10} m^2s^{-1} with increasing 6-nitroquinoline concentration.

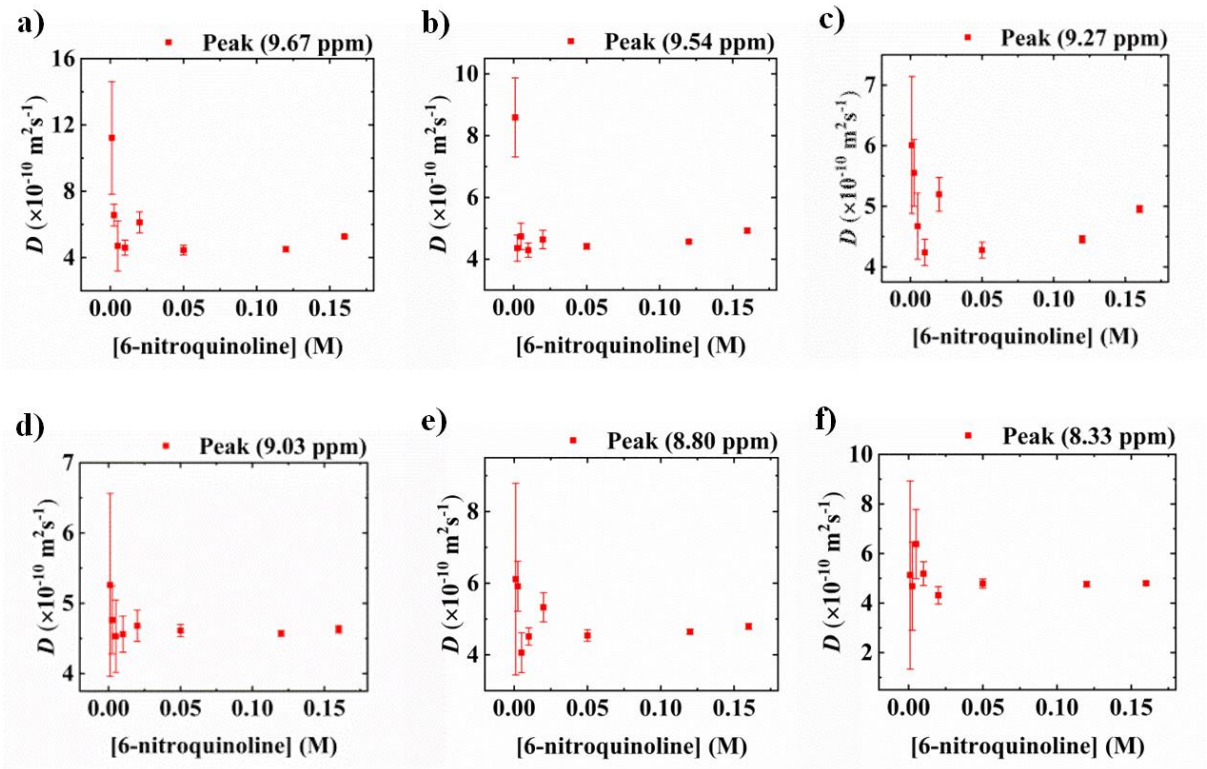

Figure 43: Diffusion coefficients of 6-nitroquinoline in 0.3 mM BSA at 298 K obtained from each of the six ^{1}H spectral peaks at a) 9.67 b) 9.54 c) 9.27 d) 9.03 e) 8.80 and f) 8.33 ppm.

Relaxation measurements of 6-nitroquinoline in BSA are shown in Figure 44 and Figure 45. R_{1f} and R_{2f} of 6-nitroquinoline across all six peaks were determined to approach ≈ 0.3 and 0.4 s^{-1}, respectively with increasing 6-nitroquinoline concentration across the range of 0.001 – 0.16 M. The R_1 measurements of 6-nitroquinoline in BSA (and R_2 to a lesser extent) is indicative of binding, with the relaxation rates decreasing with increasing concentration, and approaching R_{1f} and R_{2f} of 6-nitroquinoline. This does not align with the diffusion data

(which indicated that 6-nitroquinoline was not binding to BSA), hence for the same reasons outlined for 4-nitroimidazole, no further protein concentrations were investigated and no quantitative binding analysis was undertaken for 6-nitroquinoline. Furthermore, similar to 4-nitroimidazole, it is likely that significantly weak binding of 6-nitroquinoline to BSA is occurring. However, in this case, it is also possible that the combination of solvents used may have contributed to the nature of the binding interactions. The solvent was a mixture of DMF and D_2O, at a ratio 5:1, respectively, as 6-nitroquinoline is insoluble in water, while BSA is insoluble in DMF.

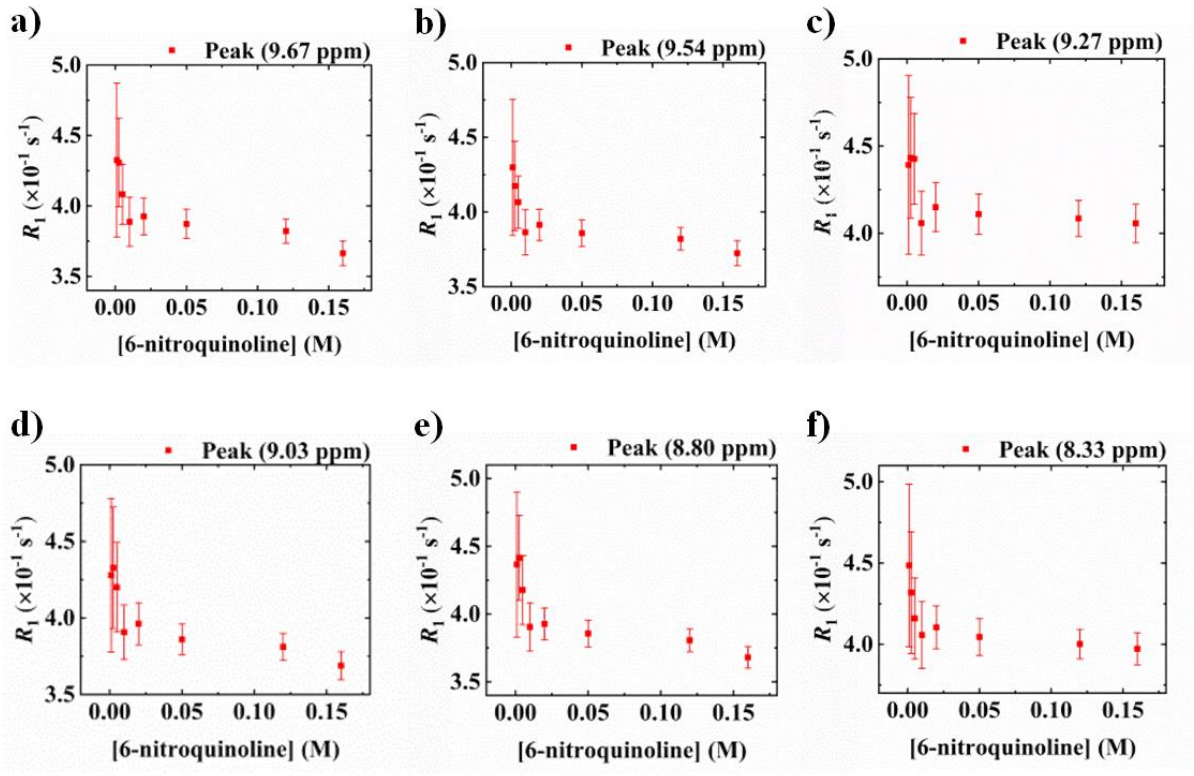

Figure 44: Spin-lattice relaxation rates of 6-nitroquinoline in 0.3 mM BSA at 298 K obtained from each of the six ^{1}H spectral peaks at a) 9.67 b) 9.54 c) 9.27 d) 9.03 e) 8.80 and f) 8.33 ppm.

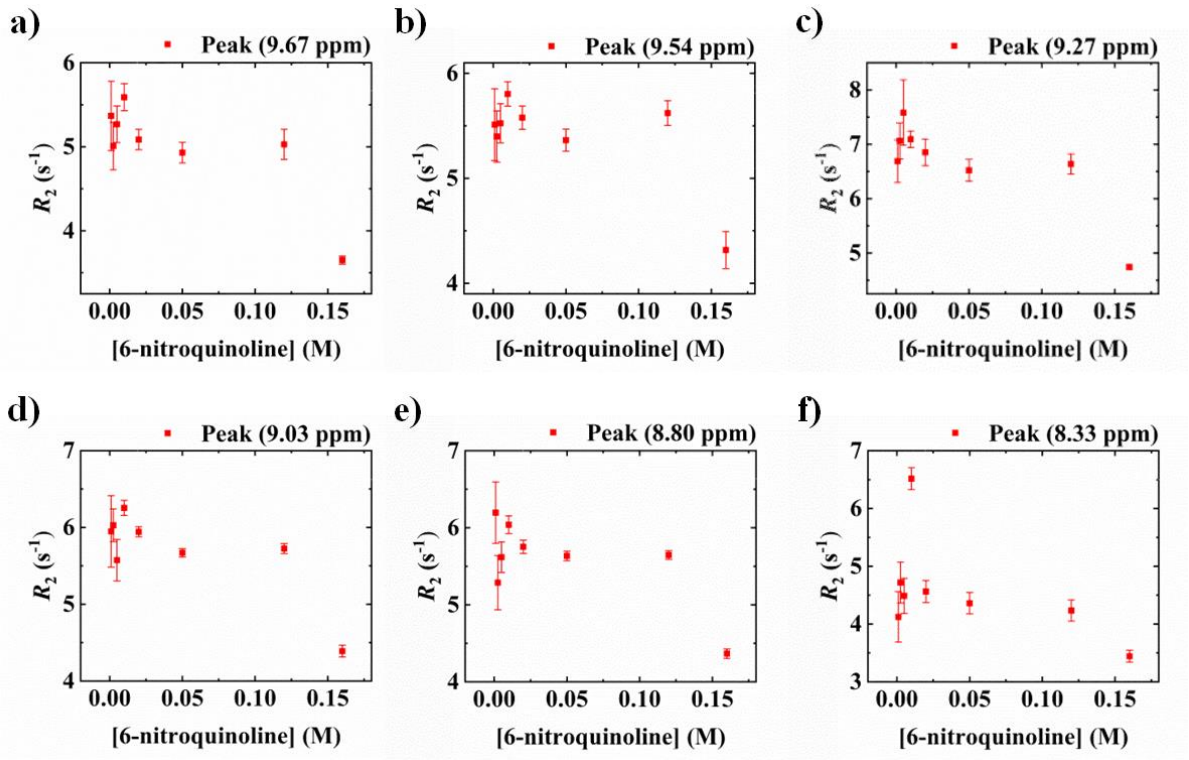

Figure 45: Spin-spin relaxation rates of 6-nitroquinoline in 0.3 mM BSA at 298 K obtained from each of the six ^{1}H spectral peaks at a) 9.67 b) 9.54 c) 9.27 d) 9.03 e) 8.80 and f) 8.33 ppm.

6.4 Conclusions

The binding interactions of 2-nitroimidazole, 4-nitroimidazole and 6-nitroquinoline to BSA were probed using NMR diffusion and relaxation measurements. Modified diffusion and relaxation attenuation equations were used to account for the overlap of the vector and protein components in the ^{1}H NMR spectra. The 2-nitroimidazole results demonstrated that both diffusion and relaxation measurements are suitable for studying such binding interactions, however, the relaxations measurements gave better agreement with the two-site Kärger model. Simultaneously fitting the data obtained from the NMR measurements (D, R_1 and R_2) yielded significantly more robust results than individually fitting each dataset. The number of binding sites and the association constant were determined to be 21 ± 3 and 53 ± 4 M^{-1}, respectively, for 2-nitroimidazole and BSA at 298 K and pH 9.4. It is likely the binding interactions between BSA and the vectors, 4-nitroimidazole and 6-nitroquinoline were considerably weak, and therefore not detected by PFG NMR. Hence the number of binding sites and the association constant were not determined for these vectors. As such, 2-nitroimidazole was determined to be the most favourable vector (i.e., the most likely to be the

strongest binding) of the three studied in this chapter, hence will be the vector used in the synthesis in the following chapter.

Chapter 7. Synthesis of Paramagnetic Liposomes

7.1 Introduction

Liposomes are well established drug delivery systems as they are biocompatible (due to being composed of phospholipids), have the ability to accommodate both hydrophilic (in the aqueous core) and hydrophobic (in the bilayer membrane) drugs, and are passively targeted to tumors due to the enhanced permeation and retention effect [143, 203]. As mentioned previously in Chapter 4, liposomes also possess favourable properties to be used as MRI contrast agents. For example, liposomes incorporating amphiphilic Gd-chelates are known to possess much better contrast enhancement efficiency (i.e., relaxivity) than small molecular Gd-chelates [204]. Such paramagnetic liposomes can also provide a large payload of Gd ions to a localised area, especially if they are actively targeted via the incorporation of targeting vectors. By incorporating hypoxia-targeting vectors and amphiphilic Gd-chelates within the bilayer membrane of the liposome, it presents the opportunity to develop hypoxia-targeting self-assembled amphiphilic paramagnetic/contrast agents.

The characterisation of a contrast agent, especially paramagnetic ions and superparamagnetic particles used as contrast agents in MRI, usually involves examining relaxivity. This is important as contrast agents tend to behave differently at different magnetic field strengths, and such characterisations aid in determining the potential suitability of new contrast agents for clinical applications, as clinics tend to utilise relatively low magnetic fields of approximately 1-3 T. Whilst relaxivity can be observed at specific magnetic fields as described in Chapter 4, relaxivity can also be measured as a function of magnetic field strength using a method referred to as relaxometry. The data curves obtained from relaxometry are known as NMRD profiles.

In this chapter, the synthesis of liposomal paramagnetic agents, incorporating 2-nitroimidazole for hypoxic targeting, and amphiphilic Gd-chelates for contrast enhancement, into the lipid bilayer, will be presented. These agents were characterised using dynamic light scattering (DLS) and inductively coupled plasma mass spectrometry (ICP-MS). The relaxivities of the paramagnetic agents with respect to composition and magnetic field strength are also reported.

7.2 Materials and Methods

7.2.1 Materials

2-nitroimidazole (98%), 1-bromooctadecane (97%) and all other chemicals were purchased from Sigma-Aldrich (Australia). 1,2-dipalmitoyl-*sn*-glycero-3-phosphocholine (DPPC), 1,2-distearoyl-*sn*-glycero-3-phosphoethanolamine-N-[methoxy(polyethyleneglycol)-2000] (PEG2000 PE), cholesterol, Gd-DTPA-bis(stearylamide) (Gd-DTPA-BSA) were purchased from Avanti Polar Lipids (USA). All solvents were purchased from Chem Supply (Australia).

7.2.2 Synthesis of (2-nitroimidazoyl)octadecane

The 2-nitroimidazole lipid component, (2-nitroimidazoyl)octadecane was synthesised according to a previously reported procedure [205] with minor modifications, as summarised in Scheme 1 and discussed below.

2-Nitroimidazole (0.27 g, 2.4 mmol) and 1-bromooctadecane (1.02 g, 3.05 mmol) were suspended in acetonitrile (20 mL) in the presence of excess potassium carbonate (2 g) and heated at 70 °C for five days. The solvent was evaporated under vacuum and the residue redissolved in dichloromethane (DCM). The base was then filtered and the filtrate purified over silica using DCM/methanol (with methanol varying from 0 – 5%) as eluent. The pure fractions (determined by TLC using 95/5 DCM/methanol) were combined and the solvents evaporated under vacuum to obtain 0.7 g (80%) of pure 1-(2-nitroimidazoyl)octadecane as a white powder.

^{1}H NMR (400 MHz, $CDCl_3$): 7.14 ppm (d, 1H, Ar), 7.07 ppm (d, 1H, Ar), 4.40 ppm (t, 2H, $C\underline{H}_2$– N_{ring}), 1.84 ppm (m, 2H, $C\underline{H}_2$–CH_2–N_{ring}), 1.36 – 1.22 ppm (m, 30H, CH_3–($C\underline{H}_2$)$_{15}$–CH_2–CH_2–N_{ring}), 0.88 ppm (t, 3H, $C\underline{H}_3$–(CH_2)$_{15}$–CH_2–CH_2–N_{ring}).

7.2.3 Liposome Preparation

Two sets of liposomes (Sets A and B) were prepared with each set divided into two types (Type I and II). Molar lipid compositions of DPPC:PEG2000PE:cholesterol:Gd-DTPA-BSA:(2-nitroimidazoyl)octadecane for Set A, Type I and II, respectively were 35:5:30:20:10 and 45:5:30:20:0, and Set B, Type I and II, respectively were 35:0:30:25:10 and 45:0:30:25:0. The total lipid concentration was 50 mM. Liposomes were prepared using the thin lipid film hydration method [206]. Lipids were first dissolved in chloroform/methanol and mixed thoroughly. Solvents were slowly dried under reduced pressure to form a thin lipid film, which was lyophilised overnight. The lipid film was rehydrated with PBS solution at 60

°C and vortexed for ~2 h. The samples were then extruded 12 times (at approximately 60 °C) through a 200 nm polycarbonate filter, followed by 12 extrusions through a 100 nm polycarbonate filter (Whatman, GE Healthcare, UK) using a mini-extruder (Avanti Polar Lipids, USA). The size of the liposomes was measured by DLS (Malvern Zetasizer μV, UK).

7.2.4 Dynamic Light Scattering

For DLS measurements, the liposomes were diluted to approximately 100 μM (lipid concentration) in PBS. The samples were equilibrated for 3 min. Each sample was run three times, with each run obtaining 15 measurements of 10 s duration each (i.e., one measurement). The average of the three runs was taken as the final result.

7.2.5 Relaxivity Studies

Four dilutions were prepared of each liposome formulation by adding Milli-Q water. NMR relaxation time measurements of the dilutions were measured at 25 °C on two spectrometers: a Magritek Spinsolve 43 MHz (1 T) benchtop spectrometer (Magritek, New Zealand) and a Bruker Avance 500 MHz (11.7 T) spectrometer (Bruker Biospin Corporation, Germany). T_1 measurements were performed using the inversion recovery method [72]. Samples were placed in straight capillary tubes (529-D, Wilmad LabGlass, USA) in 5-mm NMR tubes (528-PP-7, Wilmad Lab Glass, USA) and were equilibrated for 10 min at the set temperature prior to conducting the measurements. The recycle delay was set to ≥ 5 T_1 with the signal averaged over four scans. All data fitting for T_1 was performed using OriginPro 2018 (OriginLab, USA). The relaxivity was calculated from the slope of either the inverse relaxation time versus Gd concentration (determined by ICP-MS), or the inverse relaxation time versus relative chemical shifts [207].

The ^{1}H NMRD profiles were obtained at 25 °C using a Spinmaster Fast Field Cycling (FFC)-2000 NMR relaxometer (Stelar, Mede PV, Italy) over a continuum of magnetic fields from 2.35×10^{-4} to 0.94 T, corresponding to a ^{1}H Larmor frequency range of 0.01 – 40 MHz. The dead time of the spectrometer was approximately 10 μs.

7.2.6 Inductively-Coupled Plasma Mass Spectrometry

Concentrated nitric acid (Sigma-Aldrich, Australia) was added to the liposomal formulations in glass vials (4 ml) and left to digest over 2 days. The samples were then heated to 180 °C on a SPB 15-108 heating block (PerkinElmer, USA) for ≈ 4 h to complete the digestion and acid evaporation. Nitric acid (3% w/w, 3 ml) was added to resuspend the remaining sample (such that a 1 in 4000 dilution of the original liposomal solution was obtained), prior to transferring

samples into Falcon tubes (15 ml). ICP-MS of Gd concentrations was performed using a NexION 300X ICP-MS instrument (PerkinElmer, USA).

7.3 Results and Discussion

7.3.1 Synthesis of (2-nitroimidazoyl)octadecane

1-(2-nitroimidazoyl)octadecane was synthesised according to Scheme 1 and as discussed in the Methods, to act as an amphiphilic hypoxia-targeting vector. Hypoxia-specific paramagnetic liposomes were then formulated by incorporating commercially available paramagnetic amphiphilic chelates, and 1-(2-nitroimidazoyl)octadecane lipids within the bilayer membranes of the DPPC lipids as further discussed below.

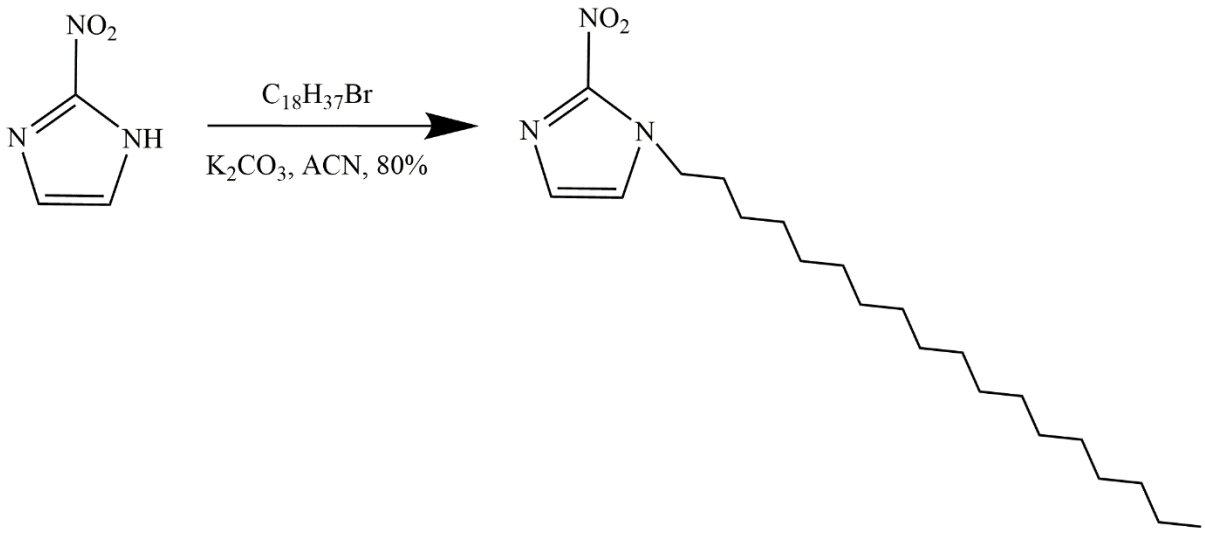

Scheme 1: Synthesis scheme of 1-(2-nitroimidazoyl)octadecane (Yield: 80%).

7.3.2 Liposome Preparation

As the liposomes were prepared as potential MRI contrast agents, a formulation that ensures long circulation times was required. The most popular method to obtain longer circulation times is to incorporate PEGylated lipids into the liposomal composition. PEG acts as a shield, protecting the liposome against interactions with molecular and biological components in the blood stream. In contrast, liposomes without PEG have short circulation times due to rapid uptake by phagocytic cells of the reticuloendothelial system [208].

In the present case, the 2-nitroimidazole amphiphiles were incorporated within the bilayer membrane and not at the distal end of the PEG spacers. As the incorporation of the PEGylated lipids had the potential to reduce the hypoxia-targeting ability of the liposomes [209-212], two sets of paramagnetic liposomes were formulated. PEGylated lipids were incorporated into one set of the liposomal membranes (Set A) but not in the other set (Set B) (Figure 46). Cholesterol was added to the liposomes to act as a spacer, and to improve their steric stabilisation [213]. The most optimal formulation for long circulation times is known to be a high cholesterol concentration of approximately 30% or greater, and a low PEG concentrations of 7% or less [206, 214]. As a result, 30% cholesterol was used for both sets of liposomes, with 5% PEG for Set A.

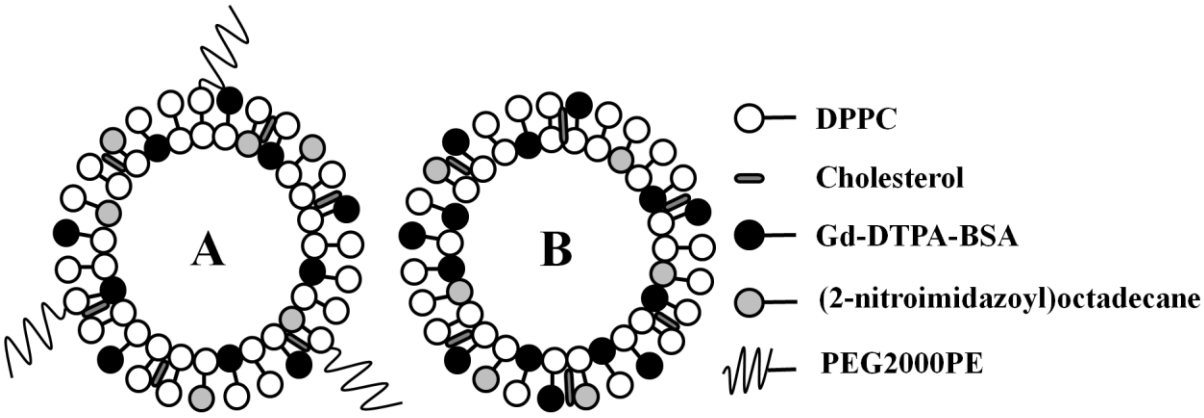

Figure 46: Schematic representation of the two sets of hypoxia-targeted paramagnetic liposomes formulated in this study. Set A liposomes were prepared with PEGylated lipids incorporated within their bilayer membrane to increase their *in vivo* circulation times. Set B liposomes were prepared without any PEGylated lipids to assess if there was any increase in the targeting ability of these liposomes in the absence of sterically hindering PEG spacers.

The preparation of the liposomes was divided into three stages: preparation of the lipid film, hydration of the lipid film and extrusion, as shown in Figure 47. In the first stage, the lipids were dissolved in a chloroform:methanol mixture to obtain a clear lipid solution, indicating complete mixing of the lipids (Figure 48a). Typically, lipid solutions are prepared at 10-20 mg of lipid per millilitre of organic solvent. In this study, approximately 12 mL of methanol:chloroform solution (50:50 ratio) was used for approximately 100 mg of lipid to ensure complete solubility of all components. The solvent was then removed by rotary

evaporation yielding a thin lipid film on the sides of the round bottom flask (Figure 48b), after which the lipid film was lyophilised overnight to remove residual organic solvent.

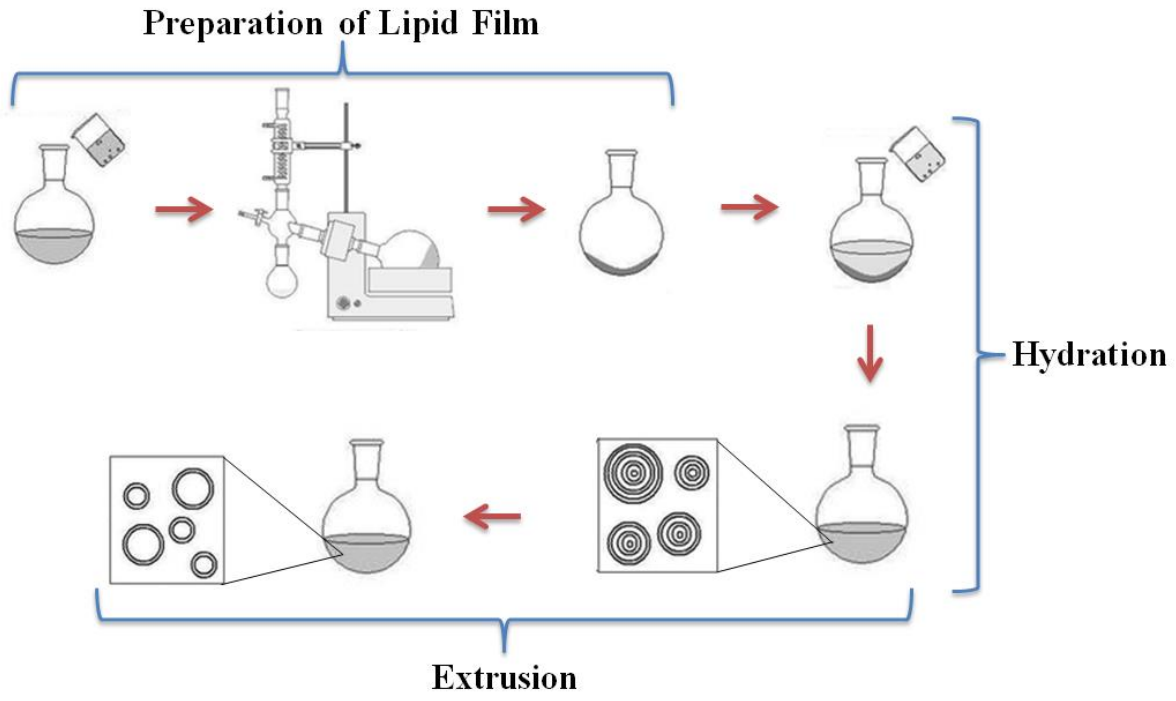

Figure 47: The three stages of liposome preparation – 1: The thin lipid film was prepared by dissolving the lipid components in an organic solvent, which was then removed using a rotary evaporator (the lyophilisation of the film has not been shown in this schematic), 2: 3 mL PBS solution was added to hydrate the dry lipid film, resulting in the formation of multilamellar vesicles, and 3: multilamellar vesicles were reduced to unilamellar vesicles by passing the solution through an extruder (image adapted from ref. [215]).

Hydration of the dry lipid film was accomplished by adding 0.01 M PBS and agitating the round bottom flask. The PBS was maintained at 60 °C to ensure the temperature of the hydrating medium was kept above the gel-liquid crystal transition temperature (T_M) of the lipid. The product of hydration is generally large, multilamellar vesicles. The multilamellar vesicles were reduced to small, uniform unilamellar vesicles via extrusion (Figure 48c). The liposomes were also extruded at 60 °C. At this point, translucent solutions were obtained (i.e., the liposomal formulations) (Figure 48d).

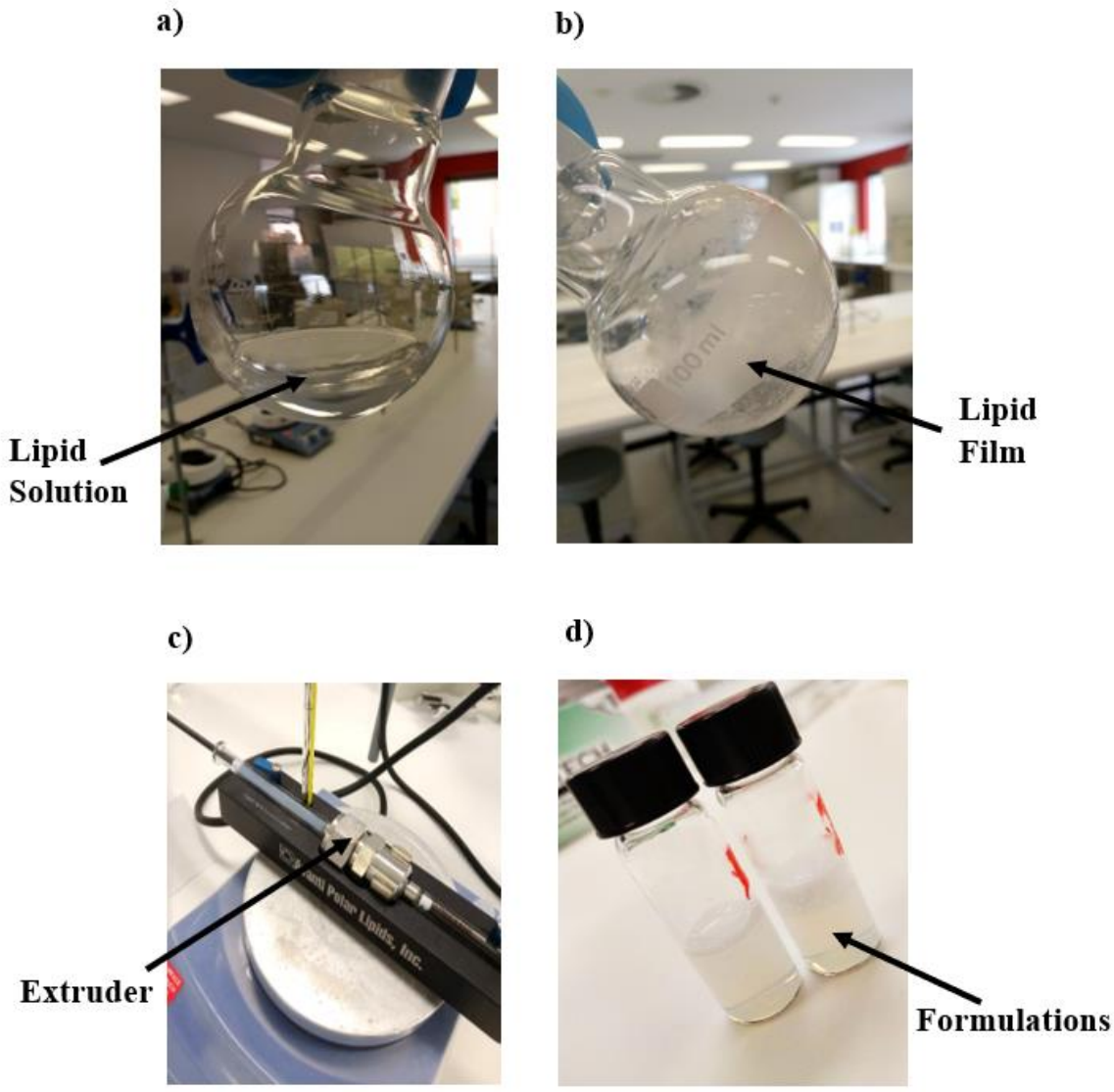

Figure 48: Images taken during the liposome preparation process showing a) the complete mixing of the lipids to obtain a clear lipid solution, b) the yielding of a thin lipid film inside the round bottom flask following rotary evaporation, c) the extrusion process, with the extruder maintained at 60 °C on a hot plate and d) the liposomal formulations obtained after extrusion.

7.3.3 DLS Measurements

The average size and polydispersity index (PDI) for each set and type of liposomes are shown in Table 2. On average, all liposomal formulations showed similar sizes (100 – 120 nm). The PDIs however, were different for liposomes with and without PEG. The wider size distribution of the liposomes without PEG as shown by the PDI and the distribution plots (Figure 49) may potentially indicate the instability of these liposomes due to the absence of PEG, thus possibly resulting in the aggregation and gravitational settling of the colloidal

particles [216]. However, there seemed to be no significant effect of the incorporation of 2-nitroimidazole amphiphiles on the size or PDI of the liposomes.

Table 2: The average size (diameter) and PDI of each liposomal formulation.

	Set A		Set B	
	Type I	**Type II**	**Type I**	**Type II**
Size (nm)	122.8	112.5	103.5	108.9
PDI	0.2	0.2	0.5	0.5

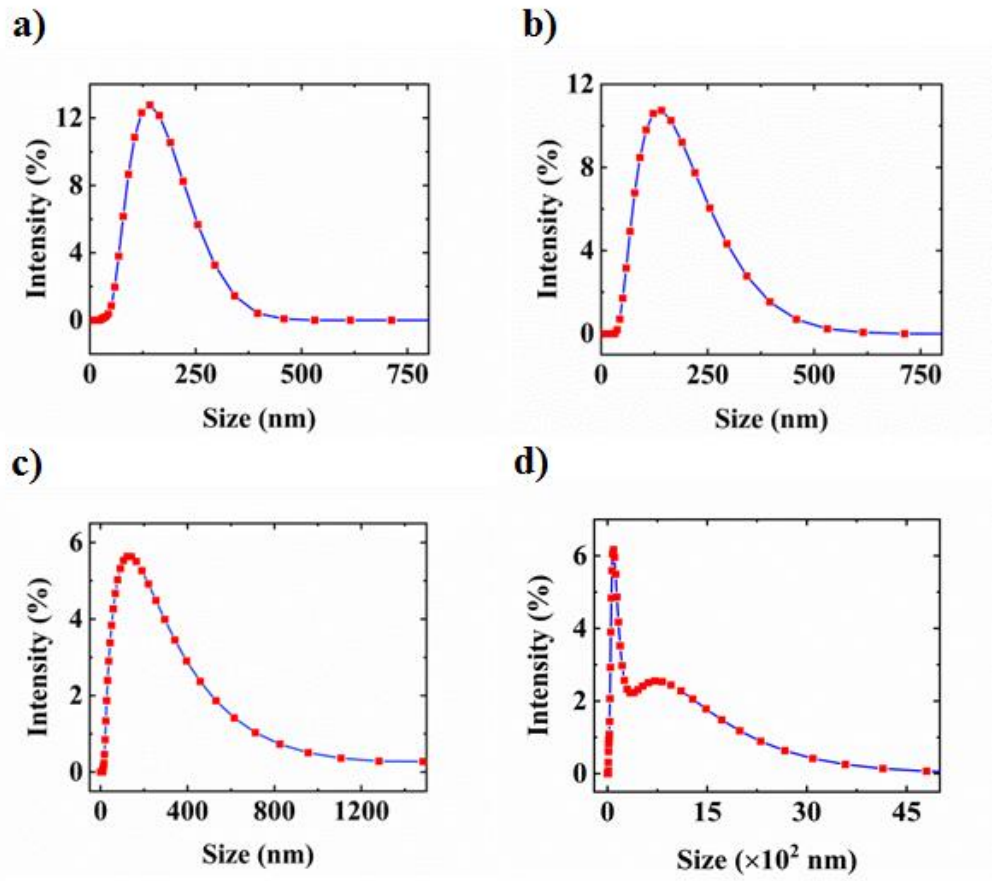

Figure 49: Liposome size distribution plots at 25 ℃ for a) Set A, Type I, b) Set A, Type II, c) Set B, Type I and d) Set B, Type II. The average count rate was 295 kilo counts per second (kcps).

7.3.4 ICP-MS

ICP-MS was then conducted on the samples to determine the exact Gd concentrations prior to calculating the relaxivities. The Gd concentration for each liposomal formulation is shown in

Table 3. The lower Gd concentration in Set B despite the higher Gd concentration of 25% (compared to 20% for Set A) added during the formulation is most likely the result of instability of the non-PEG liposomes [216]. Gravitational settling was observed for these liposomes following the synthesis, hence it is likely that some precipitation may have occurred during the extrusion process, yielding lower Gd concentrations in the liposomes without PEG.

Table 3: Gd concentrations (mM) of liposomes determined by ICP-MS.

Set A		**Set B**	
Type I	**Type II**	**Type I**	**Type II**
6.5	7.4	4.3	4.1

7.3.5 Relaxivity

The relaxivities of the liposomal formulations at 1 and 11.7 T are shown in Table 4 and Table 5, respectively. In general, the relaxivities at low magnetic fields (i.e., 1 T) were found to be higher than that reported for the commonly used commercial contrast agent, Magnevist (r_1 and $r_{2:}$ 3.8 and 4.2, respectively [217]). This is of significance in the clinics which use approximately 1-3 T magnets (e.g., [12]). At high magnetic fields (i.e., 11.7 T), r_2 was found to be significantly higher for all liposomal formulations (Table 5) than Magnevist (r_1 and $r_{2:}$ 3.8 and 4.9, respectively [217]). However, the r_1 at high fields for all liposomal formulations was lower, at approximately 2 $mM^{-1}s^{-1}$. Despite the lower r_1 for the liposomal formulations at 11.74 T (relative to 1 T), it is worthwhile noting the relaxivities are reported in terms of the Gd(III) ion concentrations, thus the relaxivity per liposome particle would be significantly higher. This is because each liposome contains numerous Gd(III) ions. For example, a 100 nm liposome with a lipid surface area of 0.6 nm^2 contains approximately 40,000 Gd(III) ions [208, 218]), which would result in a relaxivity in the order of 80,000 per nanoparticle s^{-1}.

The NMRD-profiles of the liposomal formulations are shown in Figure 50. This shows higher relaxivities in the 20-40 MHz region, indicating a longer τ_R of the Gd chelates. This was expected due to liposome incorporation.

Table 4: The relaxivities of each liposomal formulation at 1 T.

	Set A		Set B	
	Type I	**Type II**	**Type I**	**Type II**
r_1 ($mM^{-1}s^{-1}$)	6.98	6.82	9.97	10.26
r_2 ($mM^{-1}s^{-1}$)	8.24	8.02	12.14	12.53
r_2/ r_1	1.18	1.18	1.22	1.22

Table 5: The relaxivities of each liposomal formulation at 11.7 T.

	Set A		Set B	
	Type I	**Type II**	**Type I**	**Type II**
r_1 ($mM^{-1}s^{-1}$)	2.25	2.09	2.14	2.03
r_2 ($mM^{-1}s^{-1}$)	16.63	20.41	42.16	39.57
r_2/ r_1	7.39	9.77	19.70	19.49

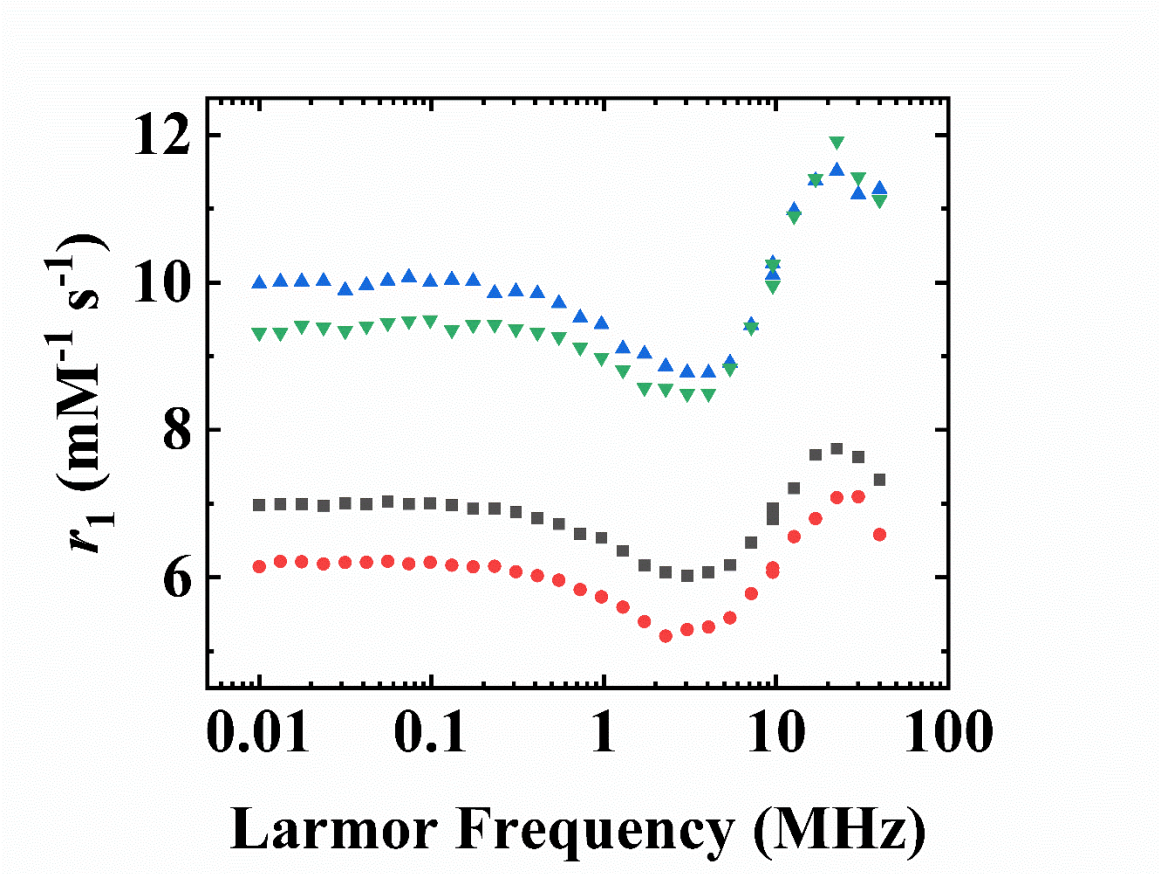

Figure 50: ^{1}H NMRD profile for each liposomal formulation: Set A – Type I (■), Set A – Type II (●), Set B – Type I (▲) and Set B – Type II (▼).

As seen in Table 4 and Figure 50, the liposomes without PEG present higher relaxivities compared to those containing PEG. This contradicts Bui, who found the inclusion of PEG on Gd-lipid nanoparticle surfaces resulted in approximately a 10-fold increase in r_1 relative to non-PEG liposomes [219]. Gløgård also investigated the effect of membrane composition on relaxivity, but observed no increase in relaxivity on PEG-modified Gd labelled liposomes [220]. To complicate this further, Issa reported a decrease in relaxivity of organic nanoparticles coated with PEG [221], where it was speculated that the reduction in relaxation rates is due to the increased distance of closest approach for the surrounding protons to the magnetic cores of the coated particles. However, as the liposomes of this current study contained Gd in the lipid bilayer, it is unlikely that PEG could have caused a similar level of shielding that was present in the organic nanoparticles, which were more rigid in structure compared to the liposomes of this current study. While the effect of PEG on the relaxivity of nanoparticles appears to not be completely clear at present (i.e., by observing the results from Bui and Gløgård), it worthwhile also considering the effective loading properties of liposomes as reported by Kabalka [137] to explain the results obtained in this thesis, as discussed below.

Kabalka reported the effect of increasing Gd concentration in liposomes on the relaxation rate, R_1, showing the most effective rate enhancement (i.e., R_1) was attained when the amphipathic Gd concentration was one-third of the lipid content of the liposome material. Theoretically, increasing the Gd concentration should see an increase in R_1. However, liposomes containing Gd concentrations greater than 33% of the lipid content reported a decrease in R_1. This indicates the effective loading capacities in liposomes. Hence, with the low molar composition of PEG (i.e., 5%), it is likely that the inclusion of PEG in the liposomal formulation for this current study had a minimal effect on r_1 (as reported by Gløgård), and the differences in relaxivity observed between the liposomal formulations with and without PEG were an effect of the loading capacities of the liposomes due to the 5% difference in Gd concentration.

Typically, r_2/r_1 is used to determine whether a contrast agent is classified as a positive (i.e., T_1) or negative (i.e., T_2) contrast agent. In general, an agent with a r_2/r_1 of approximately 1-2 is classified as a positive contrast agent, whereas any agent with a r_2/r_1 greater than 2 is classified as a negative contrast agent. Table 4 and Table 5 indicate the liposomes in this study are positive contrast agents at low field and negative contrast agents at high field, as reported in other studies [222]. It is interesting to note however, an approximate two-fold

increase in the r_2/r_1 at high field between liposomes with PEG and those without. At this stage, it is unclear whether this is related to the exclusion of PEG, or the different Gd concentrations, or both.

7.4 Conclusion

2-nitroimidazole conjugated to a saturated lipid chain was synthesised to be used as an active hypoxia-targeting amphiphilic vector. Liposomes were then formulated by incorporating 2-nitroimidazole lipids and commercially available paramagnetic amphiphiles within the bilayer membrane of phosphatidylcholine phospholipids. As the 2-nitroimidazole amphiphiles were incorporated within the bilayer membrane and not at the distal end of the PEG spacers, the incorporation of the PEGylated lipids also had the potential to reduce the hypoxia-targeting ability of the liposomes. As a result, two sets of paramagnetic liposomes were formulated: one set with PEGylated lipids and one set without. Size distribution analysis revealed the non-PEGylated liposomes to be less stable in comparison to the PEGylated liposomes, resulting in possible aggregation and gravitational settling of the colloidal particles. The contrast enhancement efficiency of the liposomes was comprehensively characterised as a function of magnetic field strength. At low magnetic fields, the relaxivities of all liposomal formulations were higher than that reported for the most commonly used commercial contrast agent, Magnevist.

Chapter 8. Investigating the Hypoxia-Specificity of the Paramagnetic Liposomes

This chapter contains verbatim passages from:

Dj Wijesekera, Abhishek Gupta, Mohammad S. Zaman, Shawan Karan, Scott A. Willis, Gary Dennis, William S. Price, Hypoxia-Specific Paramagnetic Liposomes, *ChemistryOpen*, 2018 *(submitted)*.

8.1 Introduction

As mentioned earlier in this thesis, the development of chemicals, incorporating hypoxia-targeting vectors, which specifically accumulate in hypoxic tissue has become of interest in developing methods to non-invasively detect tumor hypoxia. Such chemicals can be traced/imaged by an imaging modality, thus allowing delineation of hypoxic parts of a tumor. Markers for hypoxic tumors has long been realised [223-226], and have been extensively exploited in PET imaging [227, 228], but less so in MRI. In 2012, a Gd-based small molecular MRI contrast agent conjugated to 2-nitroimidazole was reported to display hypoxia specificity in cells and later in Dunning prostate tumors [63, 64]. These results presented an opportunity to extend the hypoxia-targeting capability of 2-nitroimidazole to self-assembled amphiphilic nanoparticulate systems.

This chapter reports on the hypoxia-targeting ability of the novel hypoxia-specific paramagnetic liposomes synthesised in Chapter 7, which incorporated 2-nitroimidazole amphiphiles as hypoxia-targeting vectors and commercially available amphiphilic Gd-chelates to impart MRI contrast. The hypoxia-specificity of the liposomes will be assessed in two different cell lines: SH-SY5Y human neuroblastoma and MCF-7 human breast adenocarcinoma. It is hypothesised that the paramagnetic liposomes with 2-nitroimidazole amphiphiles will show higher preference towards hypoxic cells in both cell lines compared to the paramagnetic liposomes without 2-nitroimidazole amphiphiles.

8.2 Materials and Methods

8.2.1 Materials

SH-SY5Y (human neuroblastoma) and MCF-7 (human breast adenocarcinoma) cells were purchased from American Type Culture Collection (ATCC, Australia). Fetal Bovine Serum (FBS), L-glutamine, penicillin/streptomycin, trypsin, phosphate buffered saline (PBS), Dulbecco's Modified Eagle's Medium/Nutrient Mixture F-12 Ham (DMEM/F12 Hams), nitric acid (69%) and all other chemical were purchased from Sigma-Aldrich (Australia).

8.2.2 *In Vitro* Cell Studies

In vitro cell studies were performed using a similar protocol as reported in ref.[63], with some modifications, as noted below.

Cells were cultured in DMEM/F12 Hams supplemented with 10% FBS, 1% penicillin/streptomycin and L-glutamine. Approximately 1×10^5 cells were seeded into a 25

cm^2 tissue culture flask (Greiner Bio-One, Germany) with 6 mL complete medium, incubated at 37 ^oC with 5% CO_2 in a Thermo Scientific HERA 150 (ThermoFisher Scientific, Australia) and grown to confluence. The complete medium was replaced with un-supplemented DMEM (6 ml) before the uptake experiment. One flask of cells was made hypoxic by passing nitrogen through it continuously at 0.8 L/min for 2 h. Air was passed through the two other flasks at 0.8 L/min to keep them normoxic (the experimental setup is shown in Figure 51). Set A, Type I paramagnetic liposomes (i.e., the liposomes with 2-nitroimidazole amphiphiles) were added to the hypoxic and one of the two normoxic flasks with SH-SY5Y cells, yielding the total lipid concentration of 6.1 mM (equating to 1.2 mM Gd) in each flask. PBS was added as the negative control in the remaining normoxic flask with SH-SY5Y cells. Three other SH-SY5Y samples were prepared using the same procedure to assess the cell uptake of Set A, Type II paramagnetic liposomes (i.e., the liposomes without 2-nitroimidazole). These samples were incubated for 2 h at room temperature (with nitrogen and air exposure as detailed previously), rinsed three times with PBS, trypsinised to release the cells and centrifuged in 15 mL Falcon tubes (Sigma-Aldrich, Australia) at 189 g for 5 min. Excess buffer was removed from the pellets and the samples were transferred into 0.2 mL microcentrifuge tubes for final centrifugation at 189 g for another 5 min.

The same procedure was followed to assess Set B (i.e., repeat study using a different cancer cell line); Types I and II paramagnetic liposomes in MCF-7 cell lines, except the total lipid concentration in each flask was 6.8 mM (equating to 1.7 mM Gd).

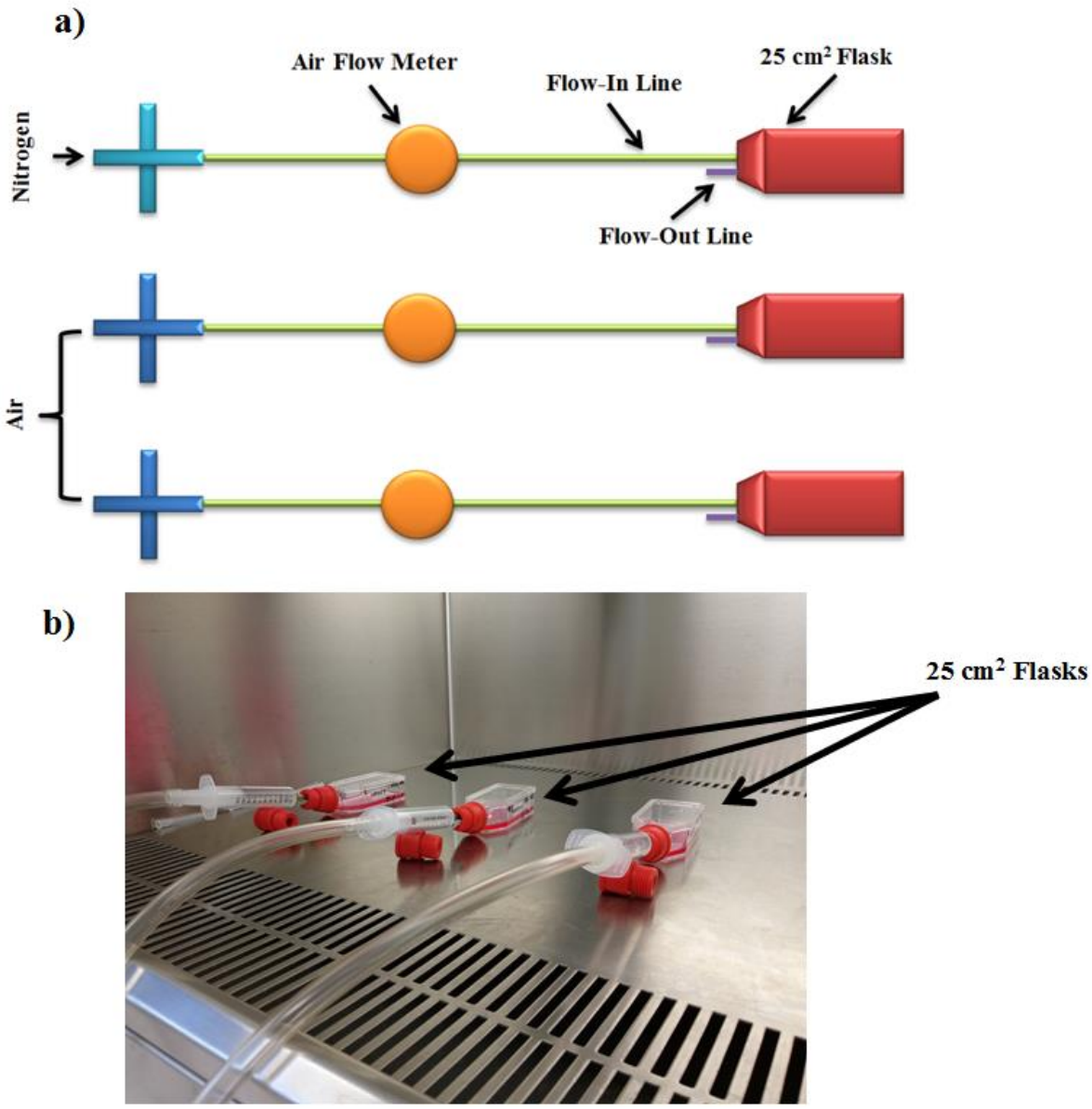

Figure 51: a) Schematic and b) image showing the setup used for obtaining hypoxic and normoxic conditions within a 25 cm^2 flask using nitrogen and air, respectively, flowing through a flow meter at a rate of 0.8 Lmin^{-1}.

8.2.3 Magnetic Resonance Imaging

All ^{1}H MRI was performed on a 600 MHz (14.1 T) wide-bore NMR spectrometer (Avance III, Bruker Biospin, Germany). An acrylonitrile butadiene styrene (ABS) holder (Figure 52) was printed on a uPrint SE 3D printer (Stratasys, USA) to position the 0.2 mL microcentrifuge tubes within the micro-imaging probe. T_1-weighted images were acquired with T_R/T_E = 900/5 ms for the SH-SY5Y cells, and T_R/T_E = 1000/4 ms for the MCF-7 cells.

A rapid acquisition with relaxation enhancement sequence with variable repetition time (RARE VTR) was used to obtain relaxation (T_1 and T_2) measurements. The typical image size was 256 × 128 pixels with a T_E of 7.95 ms and ten different T_R ranging from 70 to 7500 ms. Data acquisition was done using ParaVision 6.0 (Bruker Biospin). Raw data was then exported to MATLAB R2016a (MathWorks, Inc., USA) and T_1 maps were generated by fitting exponential relaxation curves on a voxel-by-voxel basis. The above detailed protocols were validated using water samples via NMR spectroscopy.

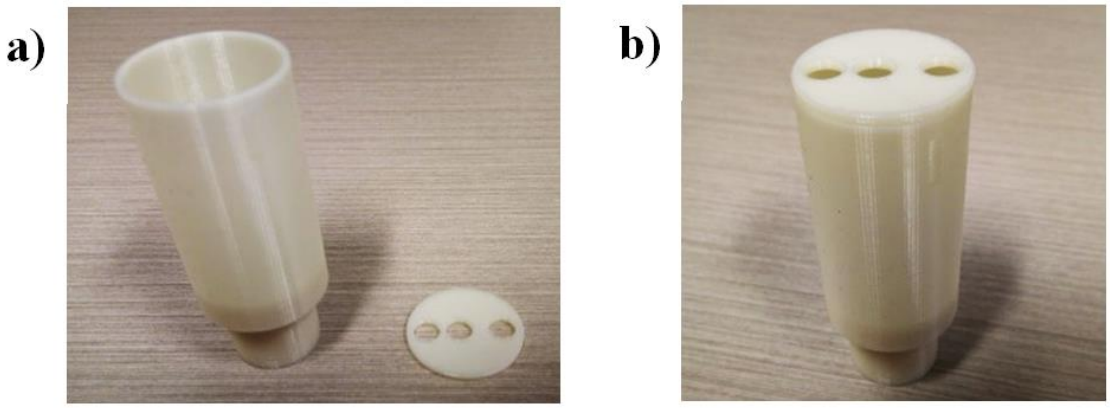

Figure 52: 3D printed 0.2 mL microcentrifuge tube holder designed on SketchUp Make (Version 15.3, United States) and printed on a uPrint SE 3D printer, measuring 70 mm in height and 28 mm in diameter. a) The lip and body of the holder were printed separately to ensure that the positioning of the microcentrifuge tube could be checked prior to inserting into the probe. b) This image shows the holder in the form that it was placed into the imaging probe.

8.2.4 Inductively-Coupled Plasma Mass Spectrometry

Concentrated nitric acid (140 µL, Sigma-Aldrich, Australia) was added to the cell pellets in glass vials (4 ml) and left to digest over 2 days. The samples were then heated at 180 °C on a SPB 15-108 heating block (PerkinElmer, USA) for ≈ 4 h to complete the digestion and acid evaporation. Nitric acid (3% w/w, 3 ml) was added to resuspend the remaining sample, prior to transferring into Falcon tubes (15 ml). ICP-MS of Gd concentrations was performed using a NexION 300X ICP-MS instrument (PerkinElmer, USA).

8.3 Results and Discussion

8.3.1 *In Vitro* Cell Studies

The hypoxia-specificity of the liposomes was assessed by measuring the cellular uptake of liposomes (both with and without hypoxia-targeting vectors) in two different cell lines: human neuroblastoma SH-SY5Y and human breast cancer MCF-7 cell lines, under normoxic and hypoxic conditions. Hypoxia was induced by passing N_2 at 0.8 L/min for 2 h at room temperature. Liposomes were then added and the cells were incubated for another 2 h under a continuous flow of N_2. Similar procedure was followed for normoxic cells except air was used instead of N_2. A negative control was also prepared in which PBS buffer (pH 7.4) was added to the cells instead of liposomes. After the incubation period, the cells were washed three times with PBS, detached from the flasks and centrifuged before imaging them on a 14.1 T MRI scanner.

8.3.2 Magnetic Resonance Imaging of the Cells

Cellular uptake of the liposomes in SH-SY5Y and MCF-7 cells in hypoxic and normoxic conditions were examined by observing the spin-lattice relaxation time (T_1) within the cell pellet. The T_1-weighted images and T_1 maps of the SH-SY5Y and MCF-7 cells incubated with Type I liposomes (i.e., with 2-nitroimidazole amphiphiles) under normoxic and hypoxic conditions are shown in Figure 53a and b, along with the negative control sample incubated with PBS alone. The average T_1 values of the cell pellets are plotted in Figure 53c. T_2-weighted images and T_2 maps of the SH-SY5Y and MCF-7 cells incubated with Type I liposomes (i.e., with 2-nitroimidazole amphiphiles) under normoxic and hypoxic conditions were also obtained. However, the results indicated negligible differences in the average T_2 values under the different conditions, hence T_2 measurements were not investigated further in this thesis.

If the 2-nitroimidazole components of the liposome underwent reduction and became trapped in the hypoxic cells, the accumulation of the Type I paramagnetic liposomes should have resulted in brighter T_1-weighted images as a result of the shortening of the T_1 of the water. However, as evident in Figure 53, no significant difference was observed in the brightness of the T_1-weighted images of the normoxic and hypoxic samples. Accordingly, the T_1 values of the cells in normoxic or hypoxic conditions did not show any statistical difference either. These results suggest that even the Type I targeted paramagnetic liposomes were either not hypoxia-specific at all, or had limited specificity.

To further assess the hypoxia-specificity of the liposomes, the cells were digested using concentrated nitric acid, and the samples were then diluted to 3 ml with 3% nitric acid (w/w). The Gd content in the dilutions was then measured using ICP-MS.

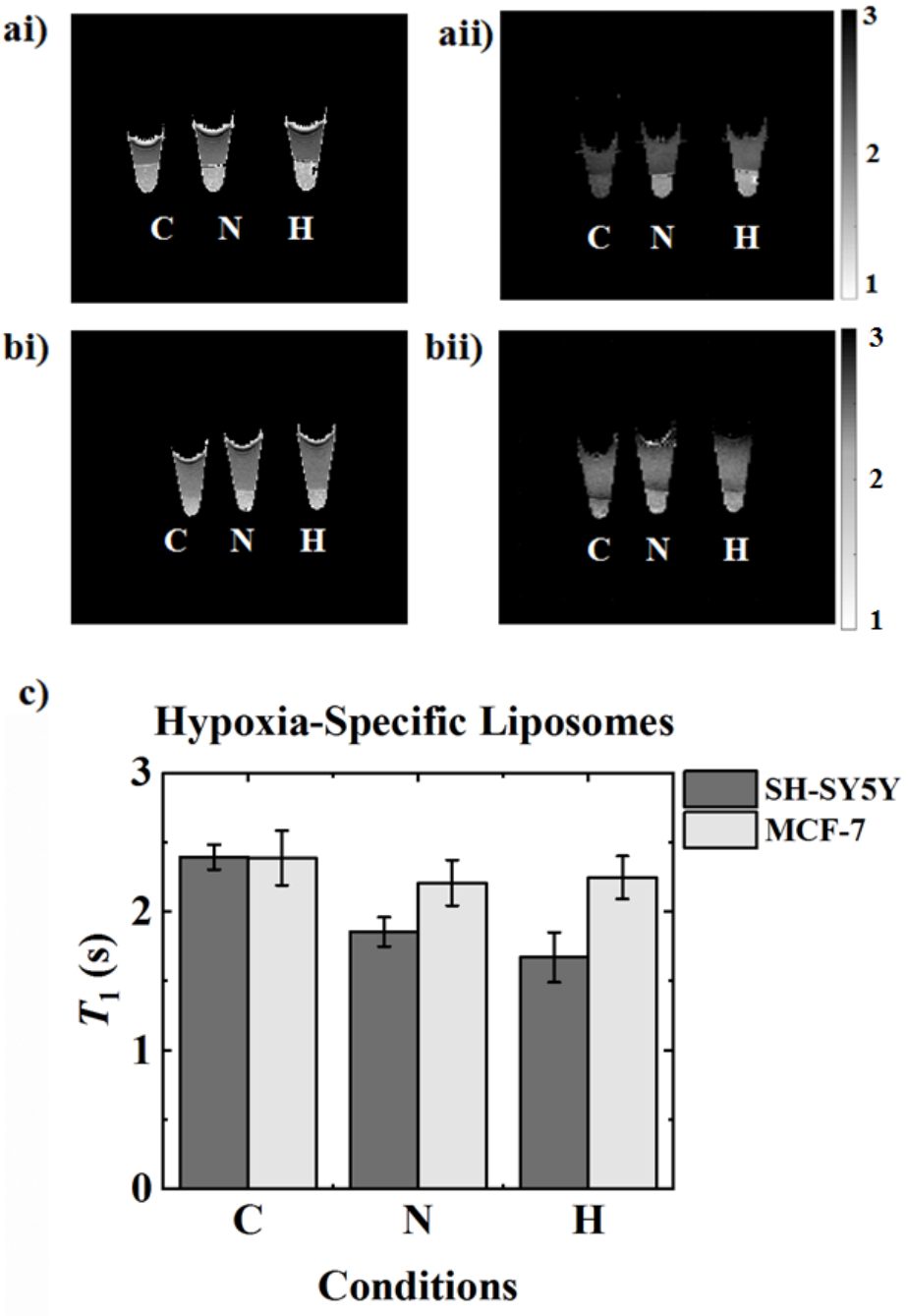

Figure 53: T_1-weighted images (i) and T_1 maps (ii) of *in vitro* MR imaging of SH-SY5Y (a) and MCF-7 (b) cells containing hypoxia-specific liposomes (i.e., containing 2-nitroimidazole) in negative control (C), normoxic (N) and hypoxic (H) conditions. The T_1-weighted images were acquired with the repetition time (T_R)/echo time (T_E) = 900/5 ms for the SH-SY5Y cells, and T_R/T_E = 1000/4 ms for the MCF-7 cells. T_1 maps were obtained using RAREVTR pulse sequence with T_E = 7.95 ms and T_R ranging from 70 – 7500 ms over 10 points. c) Plots of the average T_1 values of the cell pellets of the samples shown in (a) and (b).

8.3.3 Gadolinium Determination by ICP-MS

Gd concentrations determined by ICP-MS for the normoxic and hypoxic samples are summarised in Table 6 and plotted in Figure 54, for both cell lines. Contrary to the MRI results, ICP-MS revealed approximately three times higher Gd concentration in the hypoxic SH-SY5Y cells compared to the normoxic counterparts for the Type I paramagnetic liposomes with 2-nitroimidazole amphiphiles. Type II paramagnetic liposomes, on the other hand, displayed no preference towards hypoxic cells, as similar Gd concentrations were measured in both hypoxic and normoxic cells. Similar trends were observed for MCF-7 cell lines and Set B liposomes, with about five times higher Gd in the hypoxic cells than normoxic for Type I liposomes. Type II liposomes again showed no preference towards hypoxic cells.

The above results confirm the hypoxia-specificity of the targeted Type I paramagnetic liposomes in both SH-SY5Y and MCF-7 cell lines. As expected due to the enhanced permeation and retention effect [203], paramagnetic liposomes (with or without 2-nitroimidazole lipids) entered and were retained in both normoxic and hypoxic cells. However, the Type I liposomes with 2-nitroimidazole lipids showed a distinct preference towards hypoxic than normoxic cells, which was not observed for the Type II liposomes without 2-nitroimidazole lipids. In addition, the Set B liposomes without PEGylated lipids showed higher hypoxia-specificity than Set A liposomes with PEGylated lipids, albeit in a different cell line (MCF-7 instead of SH-SY5Y). This, once again, confirms that the hypoxia-specificity of the Type I paramagnetic liposomes is because of the 2-nitroimidazole amphiphiles, as the specificity increased when 2-nitroimidazole headgroups embedded within the bilayer membrane were made more accessible in the absence of the sterically hindering PEG spacers.

The differences in the Gd concentrations of the normoxic cells of both cell lines (e.g., 162.3 ppb for Set A, Type I in SH-SY5Y, and 45.5 ppb for Set B, Type I in MCF-7 cell lines) can most likely be attributed to the cellular properties of different cell lines and cell passages resulting in changes to passive diffusion characteristics for different liposomal formulations. Note that the cellular uptake experiments were performed on different cell passages for different paramagnetic liposome formulations. Therefore, only relative results (i.e., the

negative control, normoxic control, and hypoxic samples) for a paramagnetic liposomal formulation should be compared.

Table 6: Gd concentrations (ppb) detected by ICP-MS after the digestions and dilution of SH-SY5Y and MCF-7 cell samples incubated with different paramagnetic liposomes.

	SH-SY5Y		MCF-7	
Conditions	Type I	Type II	Type I	Type II
Normoxic	162.3 ± 2.6	27.7 ± 0.9	45.5 ± 1.4	159.8 ± 5.8
Hypoxic	455.0 ± 2.9	26.4 ± 0.5	229.0 ± 20.5	121.6 ± 5.4

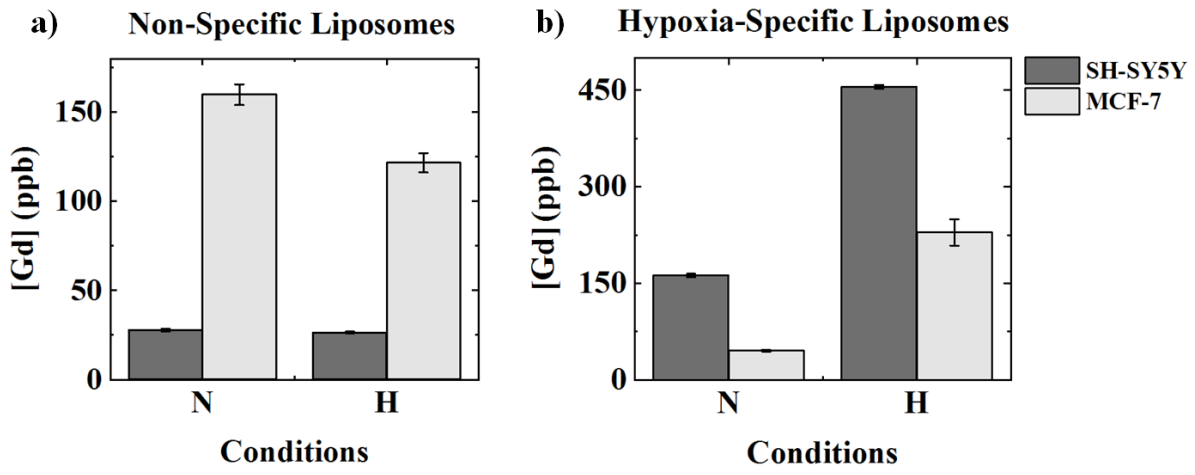

Figure 54: Gd concentrations detected by ICP-MS in the normoxic (N) and hypoxic (H) cell samples for a) non-specific (Type II) and b) hypoxia-specific (Type I) liposomes.

The uptake of type I liposomes into the SH-SY5Y cells was calculated to be approximately 24% and 9% under hypoxic and normoxic conditions, respectively, and similarly, 20% and 4% for the MCF-7 cells. It is worthwhile noting that while the absence of PEG appears to improve the targeting ability of the liposomes, it also appears to reduce the total uptake into the cells. However in this current study, this can only be speculated as this may also be the result of different cellular properties of the different cell lines.

In summary, the ICP-MS results conclusively confirm the hypoxia-specificity of the Type I paramagnetic liposomes for both the cell lines. However, this was not reflected in the MRI studies of the cell lines. To further explore this, the contrast enhancement efficiencies

(or relaxivities) of the paramagnetic liposomes determined in the previous chapter are referred to. At 1 T, the *in vitro* longitudinal relaxivities of Sets A and B of the paramagnetic liposomes were measured to be approximately 7 and 10 $mM^{-1}s^{-1}$, respectively, which is higher than the relaxivities of commercial Gd-based MRI contrast agents (typically between 3 and 5 $mM^{-1}s^{-1}$ at $\leq$ 1 T) [65], and in agreement with the values previously reported for similar paramagnetic liposomes [204]. The relaxivities were, however, found to be much lower (~ 2 $mM^{-1}s^{-1}$ for both sets of liposomes) at high magnetic field strength. Compared to a previous study on the 2-nitroimidazole conjugated Gd complex, which observed a 2-fold reduction in the T_1 values of the hypoxic cells than normoxic cells [63], cells in this study were incubated with a lower total Gd concentration (1.7 mM instead of 5 mM), and MRI studies were performed at a much higher magnetic field strength (14.1 T instead of 4.7 T). Both of these factors, suggest that even with the hypoxia-specificity of the paramagnetic liposomes, as confirmed by ICP-MS, the difference between the T_1 values of the hypoxic and normoxic cells would likely be lower than the precision of the T_1 values measured by MRI.

8.4 Conclusion

The hypoxia-targeting ability of the liposomes was assessed by comparing the cellular uptake of targeted and non-targeted paramagnetic liposomes in two cell lines: SH-SY5Y human neuroblastoma and MCF-7 human breast adenocarcinoma, in normoxic and hypoxic conditions. ICP-MS studies revealed a three and five-fold increase in the Gd concentration of the hypoxic cells relative to the normoxic cells in the SH-SY5Y and MCF-7 cell lines, respectively, confirming the hypoxia-targeting ability of these liposomal formulations. Indistinct contrast difference was observed, on the other hand, between the MR images of the normoxic and hypoxic cells in either cell-line, thus suggesting the need to design liposomal formulations with either higher Gd content, or better contrast enhancement efficiency, or both.

Chapter 9. General Conclusions and Future Work

9.1 General Conclusions

In this thesis, the primary aims of investigating the binding properties of different hypoxia-targeting vectors, and then synthesising a hypoxia-specific paramagnetic agent using one of the studied vectors were accomplished. In doing so, the following objectives were achieved:

(i) understand and derive the two-site binding Kärger model

The biological activity of drugs at the molecular level corresponds to the binding of small molecules to macromolecular receptors. NMR diffusion measurements allow bound molecules to be easily differentiated from unbound molecules. The mathematical framework for analysing such data is provided by the Kärger equations. To understand the limitations of these equations and the conditions under which they are valid, a detailed derivation of these equations for the case of two freely diffusing exchanging species was presented in this thesis along with the simplifications that result in the slow and fast exchange limits. The derivation concluded at the population weighted diffusion equation under fast exchange, which is then used to quantitatively analyse the binding interactions of the hypoxia-targeting vectors in Chapter 6 of this thesis.

(ii) quantitatively characterise the binding of different hypoxia-targeting vectors using the Kärger model

With the numerous hypoxia-targeting vectors available as discussed in this thesis, it became paramount to determine which holds the most promise to be used as a hypoxia-targeting vector prior to developing any pO_2 detection methods involving these vectors. A suitable model for such determination involves characterising the vectors with plasma proteins. Hence, the binding of three hypoxia-targeting vectors (2-nitroimidazole, 4-nitroimidazole and 6-nitroquinoline) to BSA was investigated. A thorough understanding of the Kärger equations allowed the weighted diffusion equation under fast exchange to be extended to relaxation, thus allowing the binding interactions to be investigated via diffusion and relaxation measurements. Observing the binding interactions of 2-nitroimidazole and BSA revealed that simultaneously fitting the Kärger model to the NMR data (D, R_1 and R_2) yielded significantly more robust results than individually fitting each dataset. The number of binding sites and the association constant for 2-nitroimidazole were determined to be 21 ± 3 and 53 ± 4 M^{-1}, respectively, at 298 K and pH 9.4. Such analysis was not undertaken for 4-nitroimidazole and 6-nitroquinoline as the binding interactions were considered to be

significantly weak. Hence, of the three vectors studied, 2-nitroimidazole was most likely to be the strongest binding vector.

(iii) *design, synthesise and characterise hypoxia-specific paramagnetic supramolecular nanoparticles/agents, which incorporate paramagnetic MRI contrast agent and active hypoxia-targeting vectors*

For the reasons of the biocompatibility, synthesis simplicity, high relaxivity properties and targeting capabilities, supramolecular aggregates in the form of liposomes were selected as the structure of choice to be used in the development of the hypoxia-specific paramagnetic agents in this thesis. As 2-nitroimidazole presented the most favourable binding properties of the vectors studied, a 2-nitroimidazole conjugated saturated lipid chain was synthesised to be used as an active hypoxia-targeting amphiphilic vector. Liposomes were then formulated with 2-nitroimidazole lipids and paramagnetic amphiphiles incorporated within the bilayer membrane of phosphatidylcholine phospholipids. Size distribution analysis revealed the liposomes to be uniform in size (approximately 100-120 nm in diameter). Characterising the contrast enhancement efficiency of the liposomes revealed the relaxivities for all liposomal formulations in this study to be higher than that reported for the commercially available contrast agent, Magnevist at low magnetic fields.

(iv) *investigate the hypoxia-targeting ability of the synthesised structures/agents in vitro by assessing the retention of paramagnetic metal ions in cells under hypoxic and normoxic conditions*

The hypoxia-targeting ability of the liposomes was assessed in two cell lines: SH-SY5Y human neuroblastoma and MCF-7 human breast adenocarcinoma, in normoxic and hypoxic conditions. Indistinct contrast difference was observed between the MR images of the normoxic and hypoxic cells in either cell-line. However, ICP-MS revealed a three and five-fold increase in the Gd concentration of the hypoxic cells relative to the normoxic cells in the SH-SY5Y and MCF-7 cell lines, respectively, confirming the hypoxia-targeting ability of these liposomal formulations.

9.2 Directions for Future Research

In this thesis, 2-nitroimidazole amphiphiles and commercially available paramagnetic amphiphiles were incorporated into the bilayer membrane of phosphatidylcholine phospholipids to create hypoxia-specific paramagnetic liposomes. By extending this principle to also incorporate hypoxia-activated prodrugs, such as AQ4N (1,4-bis([2-(dimethylamino)ethyl]amino)-5,8-hydroxy-anthracene-9,10-dione bis-N-oxide), into the liposomes (either in the bilayer membrane or in the central region of the liposome), it may be possible to develop hypoxia-specific theranostic liposomes in the future [229, 230], which would see the combination of diagnostic and therapeutic capabilities in a single agent.

A limitation of the hypoxia-specific paramagnetic agents that were developed in this thesis was the inability to observe a contrast difference between the hypoxic and normoxic samples using MRI. To ameliorate the MRI applications of such hypoxia-specific paramagnetic agents at high magnetic field strengths, it is imperative that a higher proportion of Gd amphiphilic chelates be incorporated within the liposomal bilayer membranes so that cellular uptake experiments can be performed with a higher Gd concentration. However, incorporating >33 mol% of the commercially available Gd-DTPA-BSA amphiphile within phospholipids is known to reduce the relaxivity of the liposomes [231]. Also, with a neutral head group in the Gd-DTPA-BSA amphiphile, higher concentrations can potentially make the liposomes unstable. Therefore, it might be better to impart hypoxia specificity to liposomes composed solely of paramagnetic amphiphiles with charged (usually anionic) head groups (i.e., without any phospholipids or cholesterol), as reported before [128, 232, 233]. However, considering the well-documented safety concerns on linear Gd chelates [122, 234], amphiphiles of the more stable macrocyclic paramagnetic chelates should replace the linear paramagnetic chelates.

To further increase the potential of MRI applications, the relaxivity of the hypoxia-specific paramagnetic liposomes will also need to be improved, especially at high magnetic field strengths. Note the relaxivity of all contrast agents diminish at high fields [235, 236]. However, by designing compounds with fast water exchange (i.e., exchange between the water molecule coordinated to the Gd ion with the bulk water) and optimum reorientational correlation time (which is dependent on the size of the molecules), it is possible to obtain liposomes with better relaxivities than the ones formulated in this present study. For example, compared to the saturated lipids used in the present study, unsaturated (e.g. oleyl/linoleyl) or

branched (e.g. phytanyl) lipid chains are known to increase the permeability of the bilayer membrane, leading to faster water exchange rate (through the bilayer membrane) and higher relaxivities [128, 237]. As a preliminary investigation to observe the change in relaxivity, another set of liposomes was developed replacing the saturated lipid, DPPC with the unsaturated lipid, 1,2-dioleoyl-sn-hlycero-3-phosphocholine (DOPC). The relaxivity (i.e., r_1) at high field increased from 2.25 $mM^{-1}s^{-1}$ (using DPPC) to 3.31 $mM^{-1}s^{-1}$ (using DOPC). Note, however, that increased leakage due to high permeability of the bilayer membrane can also impede the drug-delivery properties of the liposomes. Therefore, a balance will need to be investigated between the diagnostic and therapeutic abilities in pursuit of the development of the next generation hypoxia-specific theranostic liposomes.

References

[1] A. Sudhakar, History of cancer, ancient and modern treatment methods, *J. Cancer Sci. Ther.*, 1 (2009) 1-4.

[2] J.S. Shampton, L. Delaney, M.E. Murphy, K. Smith, M.A. Spahn, Introduction to cancer, *J. Contin. Educ.*, 9 (2007) 74.

[3] F. Bray, J. Ferlay, I. Soerjomataram, R.L. Siegel, L.A. Torre, A. Jemal, Global cancer statistics 2018: GLOBOCAN estimates of incidence and mortality worldwide for 36 cancers in 185 countries, *CA-Cancer J. Clin.*, 68 (2018) 394-424.

[4] Australian Institute of Health and Welfare, Cancer in Australia 2017, in: Cancer Series No. 101, Canberra: AIHW, (2017).

[5] C. Porth, Essentials of pathophysiology: concepts of altered health states, *Lippincott Williams & Wilkins*, Philadelphia, (2011).

[6] D. Wyatt, N. Hulbert-Williams, Cancer and cancer care, *Sage*, London, (2015).

[7] C.L. Walker, E.A. Stewart, Uterine fibroids: the elephant in the room, *Science*, 308 (2005) 1589-1592.

[8] J.L. Hess, Chromosomal translocations in benign tumors: the HMGI proteins, *American Journal of Clinical Pathology*, 109 (1998) 251-261.

[9] J.A. Gabriel, The biology of cancer, *Wiley*, Chichester, (2007).

[10] D. Glover, V. Harmer, Radiotherapy-induced skin reactions: assessment and management, *Br. J. Nurs.*, 23 (2014) S28-S35.

[11] V.T. Devita, T.S. Lawrence, S.A. Rosenberg, DeVita, Hellman, and Rosenberg's cancer: principles & practice of oncology, *Lippincott Williams & Wilkins*, Philadelphia, (2011).

[12] P.J. Keall, M. Barton, S. Crozier, The Australian magnetic resonance imaging-linac program, *Semin. Radiat. Oncol.*, 24 (2014) 203-206.

[13] X. Sui, R. Chen, Z. Wang, Z. Huang, N. Kong, M. Zhang, W. Han, F. Lou, J. Yang, Q. Zhang, X. Wang, C. He, H. Pan, Autophagy and chemotherapy resistance: a promising therapeutic target for cancer treatment, *Cell Death Dis.*, 4 (2013) e838.

[14] J.M. Brown, The hypoxic cell, *Cancer Res.*, 59 (1999) 5863-5870.

[15] A. Padhani, K. Krohn, J. Lewis, M. Alber, Imaging oxygenation of human tumours, *Eur. Radiol.*, 17 (2007) 861-872.

[16] P. Vaupel, L. Harrison, Tumor hypoxia: causative factors, compensatory mechanisms, and cellular response, *Oncologist*, 9 (2004) 4-9.

[17] P. Vaupel, F. Kallinowski, P. Okunieff, Blood Flow, Oxygen and Nutrient Supply, and Metabolic Microenvironment of Human Tumors: A Review, *Cancer Res.*, 49 (1989) 6449-6465.

[18] P. Kolstad, Intercapillary distance, oxygen tension and local recurrence in cervix cancer, *Scand. J. Clin. Lab. Invest.*, 21 (1968) 145-157.

[19] P. Bergsjö, J. Evans, Oxygen Tension of Cervical Carcinoma during the Early Phase of External Irradiation II. Measurements with Bare Platinum Micro Electrodes, *Scand. J. Clin. Lab. Invest.*, 27 (1971) 71-82.

[20] G. Powis, L. Kirkpatrick, Hypoxia inducible factor-1α as a cancer drug target, *Mol. Cancer Ther.*, 3 (2004) 647-654.

[21] E.B. Rankin, A.J. Giaccia, Hypoxic control of metastasis, *Science*, 352 (2016) 175-180.

[22] J.D. Chapman, Measurement of tumor hypoxia by invasive and non-invasive procedures: a review of recent clinical studies, *Radiother. Oncol.*, 20 (1991) 13-19.

[23] J. Liu, W. Bu, J. Shi, Chemical design and synthesis of functionalized probes for imaging and treating tumor hypoxia, *Chem. Rev.*, 117 (2017) 6160-6224.

[24] P. Vaupel, K. Schlenger, C. Knoop, M. Höckel, Oxygenation of human tumors: evaluation of tissue oxygen distribution in breast cancers by computerized O_2 tension measurements, *Cancer Res.*, 51 (1991) 3316-3322.

[25] M.-C. Kavanagh, A. Sun, Q. Hu, R.P. Hill, Comparing techniques of measuring tumor hypoxia in different murine tumors: eppendorf pO_2 histograph, [^{3}H]misonidazole binding and paired survival assay, *Radiat. Res.*, 145 (1996) 491-500.

[26] J.G. Kim, Y. Song, D. Zhao, A. Constantinescu, R.P. Mason, H. Liu, Interplay of tumor vascular oxygenation and pO2 in tumors using NIRS and needle electrode, in: Optical Tomography and Spectroscopy of Tissue IV, *Proc. SPIE 4250*, (2001), pp. 429-436.

[27] R. Mason, S. Hunjan, A. Constantinescu, Y. Song, D. Zhao, E. Hahn, P. Antich, P. Peschke, Tumor oximetry: comparison of ^{19}F MR EPI and electrodes, in: J. Dunn, H. Swartz (Eds.) Oxygen transport to tissue XXIV, *Springer*, New York, (2003), pp. 19-27.

[28] B. Wen, M. Urano, J.L. Humm, V.E. Seshan, G.C. Li, C.C. Ling, Comparison of Helzel and OxyLite Systems in the Measurements of Tumor Partial Oxygen Pressure (pO_2), *Radiat. Res.*, 169 (2008) 67-75.

[29] Y. Gu, V.A. Bourke, J.G. Kim, A. Constantinescu, R.P. Mason, H. Liu, Dynamic response of breast tumor oxygenation to hyperoxic respiratory challenge monitored with three oxygen-sensitive parameters, *Appl. Opt.*, 42 (2003) 2960-2967.

[30] D. Zhao, A. Constantinescu, E.W. Hahn, R.P. Mason, Tumor Oxygen Dynamics with Respect to Growth and Respiratory Challenge: Investigation of the Dunning Prostate R3327-HI Tumor, *Radiat. Res.*, 156 (2001) 510-520.

[31] P. Zanzonico, J. O'Donoghue, J. Chapman, R. Schneider, S. Cai, S. Larson, B. Wen, Y. Chen, R. Finn, S. Ruan, L. Gerweck, J. Humm, C. Ling, Iodine-124-labeled iodo-azomycin-galactoside imaging of tumor hypoxia in mice with serial microPET scanning, *Eur. J. Nucl. Med. Mol. Imaging*, 31 (2004) 117-128.

[32] J.A. O'Donoghue, P. Zanzonico, A. Pugachev, B. Wen, P. Smith-Jones, S. Cai, E. Burnazi, R.D. Finn, P. Burgman, S. Ruan, J.S. Lewis, M.J. Welch, C.C. Ling, J.L. Humm, Assessment of regional tumor hypoxia using ^{18}F-fluoromisonidazole and ^{64}Cu(II)-diacetyl-bis(N^4-methylthiosemicarbazone) positron emission tomography: Comparative study featuring microPET imaging, pO_2 probe measurement, autoradiography, and fluorescent microscopy in the R3327-AT and FaDu rat tumor models, *Int. J. Radiat. Oncol. Biol. Phys.*, 61 (2005) 1493-1502.

[33] J.T. Fennell, N. Wiedenmann, O. Oehlke, J.S. Kraft, A.-L. Grosu, Hypoxia and positron emission tomography in patients with gliomas, *Clin. Transl. Imaging.*, 5 (2017) 447-453.

[34] S. Chopra, W.D. Foltz, M.F. Milosevic, A. Toi, R.G. Bristow, C. Ménard, M. A. Haider, Comparing oxygen-sensitive MRI (BOLD R_2*) with oxygen electrode measurements: a pilot study in men with prostate cancer, *Int. J. Radiat. Biol.*, 85 (2009) 805-813.

[35] D. Chang, Y.-C. Wang, T.-T. Xu, X.-G. Peng, Y. Cai, L. Wang, Y.-Y. Bai, S. Ju, Noninvasive identification of renal hypoxia in experimental myocardial infarctions of different sizes by using BOLD MR imaging in a mouse model, *Radiology*, 286 (2018) 129-139.

[36] G. Mees, R. Dierckx, C. Vangestel, C. Van de Wiele, Molecular imaging of hypoxia with radiolabelled agents, *Eur. J. Nucl. Med. Mol. Imaging*, 36 (2009) 1674-1686.

[37] D. Zhao, L. Jiang, R. P. Mason, Measuring Changes in Tumor Oxygenation, in: P.M. Conn (Ed.) Methods Enzymol., *Academic Press*, (2004), pp. 378-418.

[38] H.A. Al-Hallaq, J.N. River, M. Zamora, H. Oikawa, G.S. Karczmar, Correlation of magnetic resonance and oxygen microelectrode measurements of carbogen-induced changes in tumor oxygenation, *Int. J. Radiat. Oncol. Biol. Phys.*, 41 (1998) 151-159.

[39] S.P. Robinson, F.A. Howe, L.M. Rodrigues, M. Stubbs, J.R. Griffiths, Magnetic resonance imaging techniques for monitoring changes in tumor oxygenation and blood flow, *Semin. Radiat. Oncol.*, 8 (1998) 197-207.

[40] R. Mazurchuk, R. Zhou, R.M. Straubinger, R.I. Chau, Z. Grossman, Functional magnetic resonance (fMR) imaging of a rat brain tumor model: implications for evaluation of tumor microvasculature and therapeutic response, *Magn. Reson. Imaging*, 17 (1999) 537-548.

[41] C. Baudelet, B. Gallez, How does blood oxygen level-dependent (BOLD) contrast correlate with oxygen partial pressure (pO2) inside tumors?, *Magn. Reson. Med.*, 48 (2002) 980-986.

[42] K.A. Kennedy, A.C. Sartorelli, S. Rockwell, Preferential activation of mitomycin c to cytotoxic metabolites by hypoxic tumor cells, *Cancer Res.*, 40 (1980) 2356-2360.

[43] F.W. Hunter, R.J. Young, Z. Shalev, R.N. Vellanki, J. Wang, Y. Gu, N. Joshi, S. Sreebhavan, I. Weinreb, D.P. Goldstein, J. Moffat, T. Ketela, K.R. Brown, M. Koritzinsky, B. Solomon, D. Rischin, W.R. Wilson, B.G. Wouters, Identification of P450 oxidoreductase as a major determinant of sensitivity to hypoxia-activated prodrugs, *Cancer Res.*, 75 (2015) 4211-4223.

[44] J.S. Daniels, K.S. Gates, C. Tronche, M.M. Greenberg, Direct evidence for bimodal DNA damage induced by tirapazamine, *Chem. Res. Toxicol.*, 11 (1998) 1254-1257.

[45] J.M. Brown, SR 4233 (Tirapazamine): a new anticancer drug exploiting hypoxia in solid tumours, *Br. J. Cancer*, 67 (1993) 1163.

[46] E.M. Zeman, J.M. Brown, M.J. Lemmon, V.K. Hirst, W.W. Lee, SR-4233: a new bioreductive agent with high selective toxicity for hypoxic mammalian cells, *Int. J. Radiat. Oncol. Biol. Phys.*, 12 (1986) 1239-1242.

[47] D.C. Ware, B.D. Palmer, W.R. Wilson, W.A. Denny, Hypoxia-selective antitumor agents. 7. Metal complexes of aliphatic mustards as a new class of hypoxia-selective cytotoxins. Synthesis and evaluation of cobalt(III) complexes of bidentate mustards, *J. Med. Chem.*, 36 (1993) 1839-1846.

[48] J.C. Asquith, M.E. Watts, K. Patel, C.E. Smithen, G.E. Adams, Electron Affinic Sensitization: V. Radiosensitization of Hypoxic Bacteria and Mammalian Cells in Vitro by Some Nitroimidazoles and Nitropyrazoles, *Radiat. Res.*, 60 (1974) 108-118.

[49] A. Nunn, K. Linder, H.W. Strauss, Nitroimidazoles and imaging hypoxia, *Eur. J. Nucl. Med.*, 22 (1995) 265-280.

[50] D.I. Edwards, Nitroimidazole drugs-action and resistance mechanisms I. Mechanism of action, *J. Antimicrob. Chemother.*, 31 (1993) 9-20.

[51] G.L. Kedderis, G.T. Miwa, The metabolic activation of nitroheterocyclic therapeutic agents, *Drug. Metab. Rev.*, 19 (1988) 33-62.

[52] J.A. Raleigh, C.J. Koch, Importance of thiols in the reductive binding of 2-nitroimidazoles to macromolecules, *Biochem. Pharmacol.*, 40 (1990) 2457-2464.
[53] D.R. McCalla, A. Reuvers, C. Kaiser, Mode of action of nitrofurazone, *J. Bacteriol.*, 104 (1970) 1126-1134.
[54] C.Y. Wang, B.C. Behrens, M. Ichikawa, G.T. Bryan, Nitroreduction of 5-nitrofuran derivatives by rat liver xanthine oxidase and reduced nicotinamide adenine dinucleotide phosphate-cytochrome C reductase, *Biochem. Pharmacol.*, 23 (1974) 3395-3404.
[55] J.W. Tracy, B.A. Catto, L.T. Webster, Reductive metabolism of niridazole by adult schistosoma mansoni. Correlation with covalent drug binding to parasite macromolecules, *Mol. Pharmacol.*, 24 (1983) 291-299.
[56] L.A. Poirier, J.H. Weisburger, Enzymic reduction of carcinogenic aromatic nitro compounds by rat and mouse liver fractions, *Biochem. Pharmacol.*, 23 (1974) 661-669.
[57] J.M. Brown, The mechanisms of cytotoxicity and chemosensitization by misonidazole and other nitroimidazoles, *Int. J. Radiat. Oncol. Biol. Phys.*, 8 (1982) 675-682.
[58] P. Joseph, A.K. Jaiswal, C.C. Stobbe, J.D. Chapman, The Role of Specific Reductases in the Intracellular Activation and Binding of 2-Nitroimidazoles, *Int. J. Radiat. Oncol. Biol. Phys.*, 29 (1994) 351-355.
[59] J.H. Weisburger, E.K. Weisburger, Biochemical Formation and Pharmacological, Toxicological, and Pathological Properties of Hydroxylamines and Hydroxamic Acids, *Pharmacol. Rev.*, 25 (1973) 1-66.
[60] A.J. Varghese, G.F. Whitmore, Binding to cellular macromolecules as a possible mechanism for the cytotoxicity of misonidazole, *Cancer Res.*, 40 (1980) 2165-2169.
[61] J.R. Grierson, J.M. Link, C.A. Mathis, J.S. Rasey, K.A. Krohn, A radiosynthesis of fluorine-18 fluoromisonidazole, *J. Nucl. Med.*, 30 (1989) 343.
[62] J.R. Ballinger, J.W.M. Kee, A.M. Rauth, In vitro and in vivo evaluation of a technetium-99m-labeled 2-nitroimidazole (BMS181321) as a marker of tumor hypoxia, *J. Nucl. Med.*, 37 (1996) 1023-1030.
[63] F.A. Rojas-Quijano, G. Tircsó, E. Tircsóné Benyó, Z. Baranyai, H. Tran Hoang, F.K. Kálmán, P.K. Gulaka, V.D. Kodibagkar, S. Aime, Z. Kovács, A.D. Sherry, Synthesis and characterization of a hypoxia-sensitive MRI probe, *Chem. Eur. J.*, 18 (2012) 9669-9676.
[64] P. Gulaka, F. Rojas-Quijano, Z. Kovacs, R. Mason, A.D. Sherry, V. Kodibagkar, GdDO3NI, a nitroimidazole-based T_1 MRI contrast agent for imaging tumor hypoxia in vivo, *J. Biol. Inorg. Chem.*, 19 (2014) 271-279.

[65] P. Caravan, J.J. Ellison, T.J. McMurry, R.B. Lauffer, Gadolinium(III) chelates as MRI contrast agents: structure, dynamics, and applications, *Chem. Rev.*, 99 (1999) 2293-2352.
[66] É. Tóth, L. Helm, A.E. Merbach, Relaxivity of MRI contrast agents, in: W. Krause (Ed.) Contrast Agents I: Magnetic Resonance Imaging, *Springer*, Berlin, (2002), pp. 61-101.
[67] M. Balci, Basic ^{1}H-and ^{13}C-NMR spectroscopy, *Elsevier*, Boston, (2005).
[68] R.R. Ernst, W.A. Anderson, Application of Fourier transform spectroscopy to magnetic resonance, *Rev. Sci. Instrum.*, 37 (1966) 93-102.
[69] J.C. Hoch, A.S. Stern, NMR data processing, *Wiley*, New York, (1996).
[70] M.H. Levitt, Spin dynamics: basics of nuclear magnetic resonance, *Wiley*, New York, (2008).
[71] J.H. Nelson, Nuclear magnetic resonance spectroscopy, *Prentice Hall*, New Jersey, (2003).
[72] R.L. Vold, J.S. Waugh, M.P. Klein, D.E. Phelps, Measurement of spin relaxation in complex systems, *J. Chem. Phys.*, 48 (1968) 3831-3832.
[73] E.L. Hahn, Spin Echoes, *Phys. Rev.*, 80 (1950) 580-594.
[74] H.Y. Carr, E.M. Purcell, Effects of diffusion on free precession in nuclear magnetic resonance experiments, *Phys. Rev.*, 94 (1954) 630-638.
[75] S. Meiboom, D. Gill, Modified spin-echo method for measuring nuclear relaxation times, *Rev. Sci. Instrum.*, 29 (1958) 688-691.
[76] W.S. Price, NMR studies of translational motion: principles and applications, *Cambridge University Press*, New York, (2009).
[77] G. Vogl, Diffusion and Brownian motion analogies in the migration of atoms, animals, men and ideas, *Diffusion Fundamentals*, 1 (2005) 18.
[78] S.S. Suthersan, J. Horst, M. Schnobrich, N. Welty, J. McDonough, Remediation engineering: design concepts, *CRC Press*, Boca Raton, (2016).
[79] W. Sutherland, LXXV. A dynamical theory of diffusion for non-electrolytes and the molecular mass of albumin, *Philos. Mag.*, 9 (1905) 781-785.
[80] A. Einstein, Investigations on the theory of brownian movement, *Dover*, New York, (1956).
[81] G. Truskey, F. Yuan, D. Katz, Transport phenomena in biological systems, *Prentice Hall*, New York, (2003).
[82] N. Trappeniers, C. Gerritsma, P.H. Oosting, The self-diffusion coefficient of water, at 25 C, by means of spin-echo technique, *Phys. Lett.*, 18 (1965) 256-257.

[83] W.S. Price, Recent advances in NMR diffusion techniques for studying drug binding, *Aust. J. Chem.*, 56 (2003) 855-860.

[84] D. Wijesekera, S.A. Willis, A. Gupta, A.M. Torres, G. Zheng, W.S. Price, NMR diffusion and relaxation studies of 2-nitroimidazole and albumin interactions, *Spectrochim. Acta. Mol. Biomol. Spectrosc.*, 193 (2018) 318-323.

[85] J.W. Delleur, The handbook of groundwater engineering, *CRC press*, Boca Raton, (2010).

[86] O.G. Berg, P.H.v. Hippel, Diffusion-controlled macromolecular interactions, *Annu. Rev. Biophys. Biophys. Chem.*, 14 (1985) 131-158.

[87] R.A. Alberty, G.G. Hammes, Application of the theory of diffusion-controlled reactions to enzyme kinetics, *J Phys. Chem.*, 62 (1958) 154-159.

[88] J. Keeler, Understanding NMR spectroscopy, *Wiley*, Chichester, (2011).

[89] W.S. Price, Pulsed-field gradient nuclear magnetic resonance as a tool for studying translational diffusion: Part II. Experimental aspects, *Concepts Magn. Reson.*, 10 (1998) 197-237.

[90] E.O. Stejskal, J.E. Tanner, Spin diffusion measurements: spin echoes in the presence of a time-dependent field gradient, *J. Chem. Phys.*, 42 (1965) 288-292.

[91] P.C. Lauterbur, Image formation by induced local interactions: examples employing nuclear magnetic resonance, *Nature*, 242 (1973) 190-191.

[92] S.L. Talagala, I.J. Lowe, Introduction to magnetic resonance imaging, *Concepts Magn. Reson.*, 3 (1991) 145-159.

[93] P.T. Callaghan, Principles of nuclear magnetic resonance microscopy, *Oxford University Press*, Oxford, (1991).

[94] W.E. Brant, E.E. de Lange, Essentials of body MRI, *Oxford University Press*, Oxford, (2012).

[95] A. Gupta, T.J. Stait-Gardner, B. Ghadirian, W.S. Price, Fundamental concept for the theory, dynamics and applications of MRI, in: Theory, dynamics and applications of magnetic resonance imaging-I, *Science Publishing Group*, New York, (2014), pp. 1-38.

[96] H. Jürgen, Echoes—how to generate, recognize, use or avoid them in MR-imaging sequences. Part I: Fundamental and not so fundamental properties of spin echoes, *Concepts Magn. Reson.*, 3 (1991) 125-143.

[97] H. Jürgen, Echoes—how to generate, recognize, use or avoid them in MR-imaging sequences. Part II: Echoes in imaging sequences, *Concepts Magn. Reson.*, 3 (1991) 179-192.

[98] J.P. Ridgway, Cardiovascular magnetic resonance physics for clinicians: part I, *J. Cardiovasc. Magn. Reson.*, 12 (2010) 1.

[99] R. Mezrich, A perspective on K-space, *Radiology*, 195 (1995) 297-315.

[100] R.E. Hendrick, M.E. Haacke, Basic physics of MR contrast agents and maximization of image contrast, *J. Magn. Reson. Imaging*, 3 (1993) 137-148.

[101] L. Brateman, Chemical shift imaging: a review, *Am. J. Roentgenol.*, 146 (1986) 971-980.

[102] P.E. Sijens, M.J. Van Den Bent, P.J.C.M. Nowak, P. van Dijk, M. Oudkerk, ^{1}H chemical shift imaging reveals loss of brain tumor choline signal after administration of Gd-contrast, *Magn. Reson. Med.*, 37 (1997) 222-225.

[103] S. Ogawa, T.M. Lee, A.R. Kay, D.W. Tank, Brain magnetic resonance imaging with contrast dependent on blood oxygenation, *Proc. Nat. Acad. Sci.*, 87 (1990) 9868-9872.

[104] E.-j. Vonken, M. van Osch, C. Bakker, M. Viergever, Simultaneous quantitative cerebral perfusion and Gd-DTPA extravasation measurement with dual-echo dynamic susceptibility contrast MRI, *Magn. Reson. Med.*, 43 (2000) 820-827.

[105] P.J. Basser, J. Mattiello, D. LeBihan, MR diffusion tensor spectroscopy and imaging, *Biophys. J.*, 66 (1994) 259-267.

[106] M.L. Lipton, Totally accessible MRI: a user's guide to principles, technology, and applications, *Springer*, New York, (2008).

[107] M.R. Goldman, T.J. Brady, I.L. Pykett, C.T. Burt, F.S. Buonanno, J.P. Kistler, J.H. Newhouse, W.S. Hinshaw, G.M. Pohost, Quantification of experimental myocardial infarction using nuclear magnetic resonance imaging and paramagnetic ion contrast enhancement in excised canine hearts, *Circulation*, 66 (1982) 1012-1016.

[108] P. Caravan, Strategies for increasing the sensitivity of gadolinium based MRI contrast agents, *Chem. Soc. Rev.*, 35 (2006) 512-523.

[109] E.J. Werner, A. Datta, C.J. Jocher, K.N. Raymond, High-relaxivity MRI contrast agents: where coordination chemistry meets medical imaging, *Angew. Chem. Int. Ed.*, 47 (2008) 8568-8580.

[110] E. Brücher, Kinetic stabilities of gadolinium(III) chelates used as MRI contrast agents, in: W. Krause (Ed.) Contrast Agents I: Magnetic Resonance Imaging, *Springer*, Berlin, (2002), pp. 103-122.

[111] H. Gries, Extracellular MRI contrast agents based on gadolinium, in: W. Krause (Ed.) Contrast Agents I: Magnetic Resonance Imaging, *Springer*, Berlin, (2002), pp. 1-24.

[112] H.J. Weinmann, R.C. Brasch, W.R. Press, G.E. Wesbey, Characteristics of gadolinium-DTPA complex: a potential NMR contrast agent, *Am. J. Roentgenol.*, 142 (1984) 619-624.
[113] M. Magerstädt, O.A. Gansow, M.W. Brechbiel, D. Colcher, L. Baltzer, R.H. Knop, M.E. Girton, M. Naegele, Gd(DOTA): An alternative to Gd(DTPA) as a $T_{1,2}$ relaxation agent for NMR imaging or spectroscopy, *Magn. Reson. Med.*, 3 (1986) 808-812.
[114] W.P. Cacheris, S.C. Quay, S.M. Rocklage, The relationship between thermodynamics and the toxicity of gadolinium complexes, *Magn. Reson. Imaging*, 8 (1990) 467-481.
[115] I.A. Dekkers, R. Roos, A.J. van der Molen, Gadolinium retention after administration of contrast agents based on linear chelators and the recommendations of the European Medicines Agency, *Eur. Radiol.*, 28 (2018) 1579-1584.
[116] J.W.M. Bulte, D.L. Kraitchman, Iron oxide MR contrast agents for molecular and cellular imaging, *NMR Biomed.*, 17 (2004) 484-499.
[117] Y.-X.J. Wang, S.M. Hussain, G.P. Krestin, Superparamagnetic iron oxide contrast agents: physicochemical characteristics and applications in MR imaging, *Eur. Radiol.*, 11 (2001) 2319-2331.
[118] Y.-X.J. Wang, Superparamagnetic iron oxide based MRI contrast agents: current status of clinical application, *Quant. Imaging Med. Surg.*, 1 (2011) 35-40.
[119] R.B. Lauffer, Paramagnetic metal complexes as water proton relaxation agents for NMR imaging: theory and design, *Chem. Rev.*, 87 (1987) 901-927.
[120] A. Accardo, D. Tesauro, L. Aloj, C. Pedone, G. Morelli, Supramolecular aggregates containing lipophilic Gd(III) complexes as contrast agents in MRI, *Coord. Chem. Rev.*, 253 (2009) 2193-2213.
[121] C. Nguyen-minh, V.M. Haughton, H.S. An, J.W. You, S. Wook, K.C. Ho, Contrast media of high and low molecular weights in the detection of recurrent herniated disks, *Am. J. Neuroradiol.*, 19 (1998) 889-893.
[122] T. Grobner, Gadolinium – a specific trigger for the development of nephrogenic fibrosing dermopathy and nephrogenic systemic fibrosis?, *Nephrol. Dial. Transplant.*, 21 (2006) 1104-1108.
[123] A. Khurana, V.M. Runge, M. Narayanan, J.F.J. Greene, A.E. Nickel, Nephrogenic systemic fibrosis: a review of 6 cases temporally related to gadodiamide injection (Omniscan), *Invest. Radiol.*, 42 (2007) 139-145.
[124] E. Toth, L. Helm, A. Merbach, Relaxivity of gadolinium (III) complexes: theory and mechanism, *Wiley*, New York, (2013).

[125] J. Tang, Y. Sheng, H. Hu, Y. Shen, Macromolecular MRI contrast agents: structures, properties and applications, *Prog. Polym. Sci.*, 38 (2013) 462-502.

[126] V. Degiorgio, M. Corti, Physics of amphiphiles: micelles, vesicles, and microemulsions, *North Holland*, Amsterdam, (1985).

[127] J.N. Israelachvili, D.J. Mitchell, B.W. Ninham, Theory of self-assembly of hydrocarbon amphiphiles into micelles and bilayers, *J. Chem. Soc. Faraday Trans. 2*, 72 (1976) 1525-1568.

[128] A. Gupta, S.A. Willis, L.J. Waddington, T. Stait-Gardner, L. de Campo, D.W. Hwang, N. Kirby, W.S. Price, M.J. Moghaddam, Gd-DTPA-dopamine-bisphytanyl amphiphile: synthesis, characterisation and relaxation parameters of the nanoassemblies and their potential as MRI contrast agents, *Chem. Eur. J.*, 21 (2015) 13950-13960.

[129] J.N. Israelachvili, Intermolecular and surface forces, *Academic press*, Boston, (2011).

[130] M.-C. Jones, J.-C. Leroux, Polymeric micelles – a new generation of colloidal drug carriers, *Eur. J. Pharm. Biopharm.*, 48 (1999) 101-111.

[131] P. Sharma, D. Tyrrell, B. Ryman, Some properties of liposomes of different sizes, *Biochem. Soc. Trans.*, 5 (1977) 1146.

[132] D.C. Drummond, O. Meyer, K. Hong, D.B. Kirpotin, D. Papahadjopoulos, Optimizing liposomes for delivery of chemotherapeutic agents to solid tumors, *Pharmacol. Rev.*, 51 (1999) 691-744.

[133] D.D. Lasic, Mixed micelles in drug delivery, *Nature*, 355 (1992) 279-280.

[134] A. Martínez-Coscollá, E. Miralles-Loyola, T.M. Garrigues, M.D. Sirvent, E. Salinas, V.G. Casabó, Studies on the reliability of a novel absorption-lipophilicity approach to interpret the effects of the synthetic surfactants on drug and xenobiotic absorption, *Arzneim.-Forsch.*, 43 (1993) 699-705.

[135] G.S. Kwon, K. Kataoka, Block copolymer micelles as long-circulating drug vehicles, *Adv. Drug Delivery Rev.*, 16 (1995) 295-309.

[136] C. Tilcock, E. Unger, P. Cullis, P. MacDougall, Liposomal Gd-DTPA: preparation and characterization of relaxivity, *Radiology*, 171 (1989) 77-80.

[137] G. Kabalka, E. Buonocore, K. Hubner, T. Moss, N. Norley, L. Huang, Gadolinium-labeled liposomes: targeted MR contrast agents for the liver and spleen, *Radiology*, 163 (1987) 255-258.

[138] C.W.M. Grant, S. Karlik, E. Florio, A liposomal MRI contrast agent: phosphatid ylethanolamine-DTPA, *Magn. Reson. Med.*, 11 (1989) 236-243.

[139] T. Fritz, G. Wu, D. Shen, B. Kulik, T. New, M. Crowell, N. Wilke, E. Unger, Liposomal MR contrast agents, *J. Liposome Res.*, 4 (1994) 811-834.

[140] E. Unger, D.K. Shen, G. Wu, T. Fritz, Liposomes as MR contrast agents: pros and cons, *Magn. Reson. Med.*, 22 (1991) 304-308.

[141] S.H. Koenig, Q.F. Ahkong, R.D. Brown, M. Lafleur, M. Spiller, E. Unger, C. Tilcock, Permeability of liposomal membranes to water: results from the magnetic field dependence of T_1 of solvent protons in suspensions of vesicles with entrapped paramagnetic ions, *Magn. Reson. Med.*, 23 (1992) 275-286.

[142] S.K. Kim, G.M. Pohost, G.A. Elgavish, Fatty-acyl iminopolycarboxylates: lipophilic bifunctional contrast agents for NMR imaging, *Magn. Reson. Med.*, 22 (1991) 57-67.

[143] T.M. Allen, P.R. Cullis, Liposomal drug delivery systems: From concept to clinical applications, *Adv. Drug Delivery Rev.*, 65 (2013) 36-48.

[144] Y. Barenholz, Doxil® — The first FDA-approved nano-drug: lessons learned, *J. Controlled Release*, 160 (2012) 117-134.

[145] L. Fielding, NMR methods for the determination of protein–ligand dissociation constants, *Prog. Nucl. Magn. Reson. Spectrosc.*, 51 (2007) 219-242.

[146] J. Kaplan, G. Fraenkel, NMR of chemically exchanging systems, *Academic Press*, New York, (1980).

[147] J. Sandström, Dynamic NMR spectroscopy, *Academic Press*, London, (1982).

[148] A.R. Waldeck, P.W. Kuchel, A.J. Lennon, B.E. Chapman, NMR diffusion measurements to characterise membrane transport and solute binding, *Prog. Nucl. Magn. Reson. Spectrosc.*, 30 (1997) 39-68.

[149] B. Meyer, T. Peters, NMR spectroscopy techniques for screening and identifying ligand binding to protein receptors, *Angew. Chem. Int. Ed.*, 42 (2003) 864-890.

[150] L.H. Lucas, C.K. Larive, Measuring ligand-protein binding using NMR diffusion experiments, *Concepts Magn. Res. A.*, 20A (2004) 24-41.

[151] J. Kärger, Zur Bestimmung der Diffusion in einem Zweibereichsystem mit Hilfe von gepulsten Feldgradienten, *Ann. Phys.*, 479 (1969) 1-4.

[152] J. Kärger, NMR self-diffusion studies in heterogeneous systems, *Adv. Colloid Interface Sci.*, 23 (1985) 129-148.

[153] J. Kärger, H. Pfeiffer, W. Heink, Principles and applications of self-diffusion measurements by NMR, *Adv. Magn. Reson.*, 12 (1988) 1-89.

[154] W.S. Price, A.V. Barzykin, K. Hayamizu, M. Tachiya, A model for diffusive transport through a spherical interface probed by pulsed-field gradient NMR, *Biophys. J.*, 74 (1998) 2259-2271.
[155] N. Moutal, M. Nilsson, D. Topgaard, D. Grebenkov, The Kärger vs bi-exponential model: Theoretical insights and experimental validations, *J. Magn. Reson.*, 296 (2018) 72-78.
[156] S. Hwang, J. Kärger, NMR diffusometry with guest molecules in nanoporous materials, *Magn. Reson. Imaging*, (2018).
[157] F. Bloch, Nuclear induction, *Phys. Rev.*, 70 (1946) 460-474.
[158] J.D. Roberts, The Bloch equations. How to have fun calculating what happens in NMR experiments with a personal computer, *Concepts Magn. Reson.*, 3 (1991) 27-45.
[159] H. Carslaw, J. Jaeger, Conduction of heat in solids, *Oxford University Press*, Oxford, (1959).
[160] J. Crank, The mathematics of diffusion, *Oxford University Press*, Oxford, (1975).
[161] D. Duffy, Advanced engineering mathematics with MATLAB, *CRC Press*, Boca Raton, (2010).
[162] H.C. Torrey, Bloch equations with diffusion terms, *Phys. Rev.*, 104 (1956) 563-565.
[163] W.S. Price, T. Stait-Gardner, A.M. Torres, G. Zheng, Developments in NMR diffusion measurements and q-space imaging, *Chinese J. Magn. Reson.*, 27 (2010) 267-288.
[164] W.S. Price, Pulsed-field gradient nuclear magnetic resonance as a tool for studying translational diffusion: Part 1. Basic theory, *Concepts Magn. Reson.*, 9 (1997) 299-336.
[165] W.S. Price, O. Söderman, Some "reflections" on the effects of finite gradient pulse lengths in PGSE NMR experiments in restricted systems, *Isr. J. Chem.*, 43 (2003) 25-32.
[166] H. Haddar, J.R. Li, S. Schiavi, Adapting the Kärger model to account for finite diffusion-encoding pulses in diffusion MRI, *IMA J. Appl. Math.*, 81 (2016) 779-794.
[167] W.S. Price, F. Elwinger, C. Vigouroux, P. Stilbs, PGSE-WATERGATE, a new tool for NMR diffusion-based studies of ligand–macromolecule binding, *Magn. Reson. Chem.*, 40 (2002) 391-395.
[168] A. Lauerer, R. Kurzhals, H. Toufar, D. Freude, J. Kärger, Tracing compartment exchange by NMR diffusometry: Water in lithium-exchanged low-silica X zeolites, *J. Magn. Reson.*, 289 (2018) 1-11.
[169] R.-S. Luo, M.-L. Liu, X.-A. Mao, NMR diffusion and relaxation study on ibuprofen—HSA interaction, *Appl. Spectrosc.*, 53 (1999) 776-779.
[170] T. Peters, Serum albumin, *Adv. Protein Chem.*, 37 (1985) 161-245.

[171] X.M. He, D.C. Carter, Atomic structure and chemistry of human serum albumin, *Nature*, 358 (1992) 209-215.

[172] M.H. Rahman, K. Yamasaki, Y.-H. Shin, C.C. Lin, M. Otagiri, Characterization of high affinity binding sites of non-steroidal anti-inflammatory drugs with respect to site-specific probes on human serum albumin, *Biol. Pharm. Bull.*, 16 (1993) 1169-1174.

[173] V. Andrisano, T. Booth, V. Cavrini, I. Wainer, Enantioselective separation of chiral arylcarboxylic acids on an immobilized human serum albumin chiral stationary phase, *Chirality*, 9 (1997) 178-183.

[174] V.K. Cheruvallath, C.M. Riley, S.R. Narayanan, S. Lindenbaum, J.H. Perrin, The effect of octanoic acid on the binding of the enantiomers of ibuprofen and naproxen to human serum albumin: a chromatographic implication, *Pharm. Res.*, 13 (1996) 173-178.

[175] M.T. Larsen, M. Kuhlmann, M.L. Hvam, K.A. Howard, Albumin-based drug delivery: harnessing nature to cure disease, *Mol. Cell. Ther.*, 4 (2016) 3.

[176] S. Ashoka, J. Seetharamappa, P.B. Kandagal, S.M.T. Shaikh, Investigation of the interaction between trazodone hydrochloride and bovine serum albumin, *J. Lumin.*, 121 (2006) 179-186.

[177] D. Ran, X. Wu, J. Zheng, J. Yang, H. Zhou, M. Zhang, Y. Tang, Study on the interaction between florasulam and bovine serum albumin, *J. Fluoresc.*, 17 (2007) 721-726.

[178] S. Hashimoto, T. Yabusaki, H. Takeuchi, I. Harada, Structure and ligand-binding modes of human serum albumin studied by UV resonance raman spectroscopy, *Biospectros.*, 1 (1995) 375-385.

[179] T. Itoh, Y. Saura, Y. Tsuda, H. Yamada, Stereoselectivity and enantiomer-enantiomer interactions in the binding of ibuprofen to human serum albumin, *Chirality*, 9 (1997) 643-649.

[180] V.K. Cheruvallath, C.M. Riley, S.R. Narayanan, S. Lindenbaum, J.H. Perrin, A quantitative circular dichroic investigation of the binding of the enantiomers of ibuprofen and naproxen to human serum albumin, *J. Pharm. Biomed. Anal.*, 15 (1997) 1719-1724.

[181] R.-S. Luo, M.-L. Liu, X.-A. Mao, NMR diffusion and relaxation study of drug–protein interaction, *Spectrochim. Acta. Mol. Biomol. Spectrosc.*, 55 (1999) 1897-1901.

[182] D.S. Hage, T.A.G. Noctor, I.W. Wainer, Characterization of the protein binding of chiral drugs by high-performance affinity chromatography interactions of R- and S-ibuprofen with human serum albumin, *J. Chromatogr. A*, 693 (1995) 23-32.

[183] A.S. Altieri, D.P. Hinton, R.A. Byrd, Association of biomolecular systems via pulsed field gradient NMR self-diffusion measurements, *J. Am. Chem. Soc.*, 117 (1995) 7566-7567.

[184] J. Oravcová, B. Böhs, W. Lindner, Drug-protein binding studies new trends in analytical and experimental methodology, *J. Chromatogr. B.*, 677 (1996) 1-28.

[185] M. Pellecchia, I. Bertini, D. Cowburn, C. Dalvit, E. Giralt, W. Jahnke, T.L. James, S.W. Homans, H. Kessler, C. Luchinat, B. Meyer, H. Oschkinat, J. Peng, H. Schwalbe, G. Siegal, Perspectives on NMR in drug discovery: a technique comes of age, *Nat. Rev. Drug Discov.*, 7 (2008) 738-745.

[186] K. Vuignier, J. Schappler, J.-L. Veuthey, P.-A. Carrupt, S. Martel, Drug–protein binding: a critical review of analytical tools, *Anal. Bioanal. Chem.*, 398 (2010) 53-66.

[187] C. Henoumont, L. Vander Elst, S. Laurent, R.N. Muller, Study of non-covalent interactions between MRI contrast agents and human serum albumin by NMR diffusometry, *J. Biol. Inorg. Chem.*, 14 (2009) 683-691.

[188] P. Stilbs, Fourier transform pulsed-gradient spin-echo studies of molecular diffusion, *Prog. Nucl. Magn. Reson. Spectrosc.*, 19 (1987) 1-45.

[189] A. Sulkowska, B. Lubas, T. Wilczok, The mechanism of binding of the radiosensitizers metronidazole and misonidazole (RO-07-0582) to bovine and human serum albumin: a proton NMR study, *Radiat. Res.*, 85 (1981) 1-12.

[190] D.R. Sanvordeker, Y.W. Chien, T.K. Lin, H.J. Lambert, Binding of metronidazole and its derivatives to plasma proteins: an assessment of drug binding phenomenon, *J. Pharm. Sci.*, 64 (1975) 1797-1803.

[191] L. Fielding, S. Rutherford, D. Fletcher, Determination of protein–ligand binding affinity by NMR: observations from serum albumin model systems, *Magn. Reson. Chem.*, 43 (2005) 463-470.

[192] J.E. Tanner, Use of the stimulated echo in NMR diffusion studies, *J. Chem. Phys.*, 52 (1970) 2523-2526.

[193] S.A. Willis, G.R. Dennis, G. Zheng, W.S. Price, Preparation and physical properties of a macroscopically aligned lyotropic hexagonal phase templated hydrogel, *React. Funct. Polym.*, 73 (2013) 911-922.

[194] S.A. Willis, G.R. Dennis, T. Stait-Gardner, G. Zheng, W.S. Price, Determining a ‘diffusion-averaged’ characteristic ratio for aligned lyotropic hexagonal phases using PGSE NMR self-diffusion measurements, random walk simulations and obstruction models, *J. Mol. Liq.*, 236 (2017) 107-116.

[195] J.-P. Melchior, G. Majer, K.-D. Kreuer, Why do proton conducting polybenzimidazole phosphoric acid membranes perform well in high-temperature PEM fuel cells?, *Phys. Chem. Chem. Phys.*, 19 (2017) 601-612.

[196] W.S. Price, F. Hallberg, P. Stilbs, A PGSE diffusion and electrophoretic NMR study of Cs^+ and Na^+ dynamics in aqueous crown ether systems, *Magn. Reson. Chem.*, 45 (2007) 152-156.

[197] A.J. Lennon, N.R. Scott, B.E. Chapman, P.W. Kuchel, Hemoglobin affinity for 2,3-bisphosphoglycerate in solutions and intact erythrocytes: studies using pulsed-field gradient nuclear magnetic resonance and Monte Carlo simulations, *Biophys. J.*, 67 (1994) 2096-2109.

[198] M. Liu, J. K. Nicholson, J. C. Lindon, Analysis of drug-protein binding using nuclear magnetic resonance based molecular diffusion measurements, *Anal. Commun.*, 34 (1997) 225-228.

[199] D. Leckband, J. Israelachvili, Intermolecular forces in biology, *Q. Rev. Biophys.*, 34 (2001) 105-267.

[200] J. Chen, X.Y. Jiang, X.Q. Chen, Y. Chen, Effect of temperature on the metronidazole–BSA interaction: Multi-spectroscopic method, *J. Mol. Struct.*, 876 (2008) 121-126.

[201] J. Wilting, W.F. van der Giesen, L.H. Janssen, M.M. Weideman, M. Otagiri, J.H. Perrin, The effect of albumin conformation on the binding of warfarin to human serum albumin., *J. Biol. Chem.*, 255 (1980) 3032-3037.

[202] G.R. Fulmer, A.J.M. Miller, N.H. Sherden, H.E. Gottlieb, A. Nudelman, B.M. Stoltz, J.E. Bercaw, K.I. Goldberg, NMR chemical shifts of trace impurities: common laboratory solvents, organics, and gases in deuterated solvents relevant to the organometallic chemist, *Organometallics*, 29 (2010) 2176-2179.

[203] K. Greish, Enhanced permeability and retention (EPR) effect for anticancer nanomedicine drug targeting, *Humana Press*, New Jersey, (2010).

[204] T.N. Parac-Vogt, K. Kimpe, S. Laurent, C. Piérart, L.V. Elst, R.N. Muller, K. Binnemans, Paramagnetic liposomes containing amphiphilic bisamide derivatives of Gd-DTPA with aromatic side chain groups as possible contrast agents for magnetic resonance imaging, *Eur. Biophys. J.*, 35 (2006) 136-144.

[205] M.P. Hay, W.R. Wilson, J.W. Moselen, B.D. Palmer, W.A. Denny, Hypoxia-selective antitumor agents. 8. Bis(nitroimidazolyl)alkanecarboxamides: a new class of hypoxia-selective cytotoxins and hypoxic cell radiosensitizers, *J. Med. Chem.*, 37 (1994) 381-391.

[206] J. Dua, A. Rana, A. Bhandari, Liposome: methods of preparation and applications, *Int. J. Pharm. Stud. Res.*, 3 (2012) 14-20.

[207] A. Gupta, S.A. Willis, T. Stait-Gardner, M.J. Moghaddam, W.S. Price, Fast determination of the ^{1}H relaxivities of MRI contrast agents, *Magn. Reson. Chem.*, 54 (2016) 58-61.

[208] G.J. Strijkers, W.J.M. Mulder, R.B. van Heeswijk, P.M. Frederik, P. Bomans, P.C.M.M. Magusin, K. Nicolay, Relaxivity of liposomal paramagnetic MRI contrast agents, *Magn. Reson. Mater. Phy.*, 18 (2005) 186-192.

[209] A. Mori, A.L. Klibanov, V.P. Torchilin, L. Huang, Influence of the steric barrier activity of amphipathic poly(ethyleneglycol) and ganglioside GM_1 on the circulation time of liposomes and on the target binding of immunoliposomes in vivo, *FEBS Lett.*, 284 (1991) 263-266.

[210] A.L. Klibanov, K. Maruyama, A.M. Beckerleg, V.P. Torchilin, L. Huang, Activity of amphipathic poly(ethylene glycol) 5000 to prolong the circulation time of liposomes depends on the liposome size and is unfavorable for immunoliposome binding to target, *Biochim. Biophys. Acta, Rev. Biomembr.*, 1062 (1991) 142-148.

[211] V.P. Torchilin, A.L. Klibanov, L. Huang, S. O'Donnell, N.D. Nossiff, B.A. Khaw, Targeted accumulation of polyethylene glycol-coated immunoliposomes in infarcted rabbit myocardium, *FASEB. J.*, 6 (1992) 2716-2719.

[212] V.P. Torchilin, Immunoliposomes and PEGylated immunoliposomes: possible use for targeted delivery of imaging agents, *ImmunoMethods*, 4 (1994) 244-258.

[213] C. Kirby, J. Clarke, G. Gregoriadis, Effect of the cholesterol content of small unilamellar liposomes on their stability in vivo and in vitro, *Biochem. J.*, 186 (1980) 591-598.

[214] G.T. Noble, J.F. Stefanick, J.D. Ashley, T. Kiziltepe, B. Bilgicer, Ligand-targeted liposome design: challenges and fundamental considerations, *Trends Biotechnol.*, 32 (2014) 32-45.

[215] S.C. de Araújo Lopes, C. dos Santos Giuberti, T.G.R. Rocha, D. dos Santos Ferreira, E.A. Leite, M.C. Oliveira, Liposomes as carriers of anticancer drugs, in: Cancer Treatment-Conventional and Innovative Approaches, *InTech*, (2013).

[216] A.K. Gupta, M. Gupta, Synthesis and surface engineering of iron oxide nanoparticles for biomedical applications, *Biomaterials*, 26 (2005) 3995-4021.

[217] M. Mikawa, H. Kato, M. Okumura, M. Narazaki, Y. Kanazawa, N. Miwa, H. Shinohara, Paramagnetic water-soluble metallofullerenes having the highest relaxivity for MRI contrast agents, *Bioconjugate Chem.*, 12 (2001) 510-514.

[218] M. Dekker, Phospholipids Handbook, *Marcel Dekker Inc.*, New York, (1993).

[219] T. Bui, J. Stevenson, J. Hoekman, S. Zhang, K. Maravilla, R.J.Y. Ho, Novel Gd nanoparticles enhance vascular contrast for high-resolution magnetic resonance imaging, *PLoS One*, 5 (2010) e13082.

[220] C. Gløgård, G. Stensrud, R. Hovland, S.L. Fossheim, J. Klaveness, Liposomes as carriers of amphiphilic gadolinium chelates: the effect of membrane composition on incorporation efficacy and in vitro relaxivity, *Int. J. Pharm.*, 233 (2002) 131-140.

[221] B. Issa, S. Qadri, I.M. Obaidat, R.W. Bowtell, Y. Haik, PEG coating reduces NMR relaxivity of $Mn_{0.5}Zn_{0.5}Gd_{0.02}Fe_{1.98}O_4$ hyperthermia nanoparticles, *J. Magn. Reson. Imaging*, 34 (2011) 1192-1198.

[222] A. Gupta, L. de Campo, B. Rehmanjan, S.A. Willis, L.J. Waddington, T. Stait-Gardner, N. Kirby, W.S. Price, M.J. Moghaddam, Evaluation of Gd-DTPA-monophytanyl and phytantriol nanoassemblies as potential MRI contrast agents, *Langmuir*, 31 (2015) 1556-1563.

[223] J.D. Chapman, A.J. Franko, J. Sharplin, A marker for hypoxic cells in tumours with potential clinical applicability, *Br. J. Cancer*, 43 (1981) 546-550.

[224] R.J. Maxwell, P. Workman, J.R. Griffiths, Demonstration of tumor-selective retention of fluorinated nitroimidazole probes by ^{19}F magnetic resonance spectroscopy in vivo, *Int. J. Radiat. Oncol. Biol. Phys.*, 16 (1989) 925-929.

[225] E.O. Aboagye, A.D. Lewis, A. Johnson, P. Workman, M. Tracy, I.M. Huxham, The novel fluorinated 2-nitroimidazole hypoxia probe SR-4554: reductive metabolism and semiquantitative localisation in human ovarian cancer multicellular spheroids as measured by electron energy loss spectroscopic analysis, *Br. J. Cancer*, 72 (1995) 312.

[226] B.M. Seddon, G.S. Payne, L. Simmons, R. Ruddle, R. Grimshaw, S. Tan, A. Turner, F. Raynaud, G. Halbert, M.O. Leach, I. Judson, P. Workman, A phase I study of SR-4554 via intravenous administration for noninvasive investigation of tumor hypoxia by magnetic resonance spectroscopy in patients with malignancy, *Clin. Cancer Res.*, 9 (2003) 5101-5112.

[227] S.T. Lee, A.M. Scott, Hypoxia positron emission tomography imaging with ^{18}F-fluoromisonidazole, *Semin. Nucl. Med.*, 37 (2007) 451-461.

[228] W.J. Koh, J.S. Rasey, M.L. Evans, J.R. Grierson, T.K. Lewellen, M.M. Graham, K.A. Krohn, T.W. Griffin, Imaging of hypoxia in human tumors with [F-18]fluoromisonidazole, *Int. J. Radiat. Oncol. Biol. Phys.*, 22 (1991) 199-212.

[229] L.H. Patterson, Rationale for the use of aliphatic N-oxides of cytotoxic anthraquinones as prodrug DNA binding agents: a new class of bioreductive agent, *Cancer Metast. Rev.*, 12 (1993) 119-134.

[230] L. Feng, L. Cheng, Z. Dong, D. Tao, T.E. Barnhart, W. Cai, M. Chen, Z. Liu, Theranostic liposomes with hypoxia-activated prodrug to effectively destruct hypoxic tumors post-photodynamic therapy, *ACS Nano*, 11 (2017) 927-937.

[231] G.W. Kabalka, E. Buonocore, K. Hubner, M. Davis, L. Huang, Gadolinium-labeled liposomes containing paramagnetic amphipathic agents: Targeted MRI contrast agents for the liver, *Magn. Reson. Med.*, 8 (1988) 89-95.
[232] A. Gupta, L. de Campo, L.J. Waddington, R.B. Knott, D. Hwang, N. Kirby, W.S. Price, M.J. Moghaddam, Towards advanced paramagnetic nanoassemblies of highly ordered interior nanostructures as potential MRI contrast agents, *New J. Chem.*, 41 (2017) 2735-2744.
[233] M.J. Moghaddam, L.d. Campo, N. Kirby, C.J. Drummond, Chelating DTPA amphiphiles: ion-tunable self-assembly structures and gadolinium complexes, *Phys. Chem. Chem. Phys.*, 14 (2012) 12854-12862.
[234] Y. Errante, V. Cirimele, C.A. Mallio, V. Di Lazzaro, B.B. Zobel, C.C. Quattrocchi, Progressive increase of T_1 signal intensity of the dentate nucleus on unenhanced magnetic resonance images is associated with cumulative doses of intravenously administered gadodiamide in patients with normal renal function, suggesting dechelation, *Invest. Radiol.*, 49 (2014) 685-690.
[235] P. Caravan, C.T. Farrar, L. Frullano, R. Uppal, Influence of molecular parameters and increasing magnetic field strength on relaxivity of gadolinium- and manganese-based T_1 contrast agents, *Contrast Media Mol. Imaging*, 4 (2009) 89-100.
[236] A. Gupta, T. Stait-Gardner, M.J. Moghaddam, W.S. Price, Dipolar relaxation revisited: a complete derivation for the two spin case, *Concepts Magn. Res. A.*, 44 (2015) 74-113.
[237] S. Laurent, L. Vander Elst, C. Thirifays, R.N. Muller, Relaxivities of paramagnetic liposomes: on the importance of the chain type and the length of the amphiphilic complex, *Eur. Biophys. J.*, 37 (2008) 1007-1014.